Faculty of Electrical Engineering,
Mathematics & Computer Science
Department of Microelectronics and
Computer Engineering,
High-Frequency Technology and Components

Faculty of Applied Sciences,
Kavli Institute of NanoScience,
Physics of NanoElectronics

Modeling and optimization of Nb tuning circuits for Nb/AlOx/Nb SIS mixers in the 600-720 GHz range

Master Thesis by: **Omid Noroozian**

Student Number: ET1245821
Research Group: Physics of Nano Electronics
Group Leader: Prof. dr. ir. T.M. Klapwijk
Supervisors: Prof. dr. ir. T.M. Klapwijk and Dr. B. Rejaei Salmassi
Period: August 2005 -August 2006

Modeling and optimization of Nb tuning circuits for Nb/AlOx/Nb SIS mixers in the 600-720 GHz range

Omid Noroozian

August 1, 2006

Abstract

This thesis describes the development, modeling, and optimization of Nb superconducting microstrip tuning circuits for Superconductor-Insulator-Superconductor mixers. The ultimate goal is to extend the quantum limited noise performance of Nb/AlOx/Nb SIS mixers to above the Nb gap frequency (680 GHz). The mixers are intended to be used in the Atacama Large Millimeter Array (ALMA) band 9 frequency range (600-720 GHz). The behavior of Nb microstrip tuning circuits especially above the gap frequency is modeled using the complex conductivity given by the Mattis-Bardeen theory of the anomalous skin effect [72]. A computer code utilizing two-port network theory is utilized to predict and optimize the RF coupling efficiency and bandwidth of the tuning circuits and embedding impedances. The effect of material and geometrical variations on the coupling has been evaluated. The installment of the devices in the waveguide has been found to be a crucial factor explaining the observed scattering in measurement results for nominally identical devices. Despite parameter variations, modeling of the RF coupling efficiency proved to be successful within the limitations set by scattering of the measured results. Using this model, the tuning circuit geometry has been optimized for bandwidth and maximum coupling efficiency. During the work several SIS devices whave been fabricated and Fourier transform spectroscopy measurements have been made for RF coupling evaluation. Finally, using simulations, it has been found that application of Nb/AlN/Nb junctions would increase the bandwidth to an extent which should dramatically decrease the sensitivity to parameter variations.

Contents

Chapter 1
Introduction

Superconductor–Insulator–Superconductor (SIS) receivers are the most sensitive receivers for millimeter and submillimeter astronomy. In this chapter, submillimeter astronomy is briefly described to justify the need for sensitive heterodyne receivers. The developed receivers in this work will be used in the Atacama Large Millimeter Array (ALMA) telescope which will be introduced. The principle of heterodyne detection is then presented along with some important properties of receivers. This is followed by a short overview of the current state of the terahertz technology.

1.1 Motivation

The submillimeter electromagnetic band can be defined loosely as wavelengths from 1 mm (300 GHz) to 100 μm (3 THz), and is one of the most important regions of the electromagnetic spectrum for astronomy. Results from the NASA Cosmic Background Explorer (COBE) indicate that 98% of the photons emitted since the Big Bang fall into the submillimeter and far-IR range [4]. This means that a huge wealth of scientific information is contained in this region. Yet, it is one of the least explored fields in astronomy.

The challenge in fully exploring the submillimeter band is of a technical nature. Due to the relatively weak sources in the submillimeter band, large telescopes with high surface accuracy must be constructed in order to have high sensitivity and good angular resolution. Moreover, the atmosphere is not at all or little transparent in most of the submillimeter band. This means in particular that the interstellar medium, the material between the stars from which stars form, is difficult to observe from the ground. Figure.1.1 (upper) shows the transparency of atmosphere for good weather conditions at an altitude of 4200m on Mauna Kea, Hawaii for the submillimeter band. There are three useful regions: the radio/millimeter region from 0 to 300 GHz, which is almost completely transparent, and the two wide submillimeter windows at $\sim$ 650 GHz (450 μm) and 850 GHz (350μm). The rest of the spectrum is blacked out by absorbtion mainly by water. The atmosphere is completely opaque at shorter wavelengths until the mid-infrared windows at - 30μm (10 THz) are reached. At airborne altitudes, say 12000 m, the transmission is much

better, but also not perfect as can be seen in Fig. 1.1 (lower). The spectrum between 600 GHz and 3 THz has many strong water absorbtion lines, which could possibly interfere with specific spectral line studies and would contaminate continuum or wideband spectroscopy data [1].

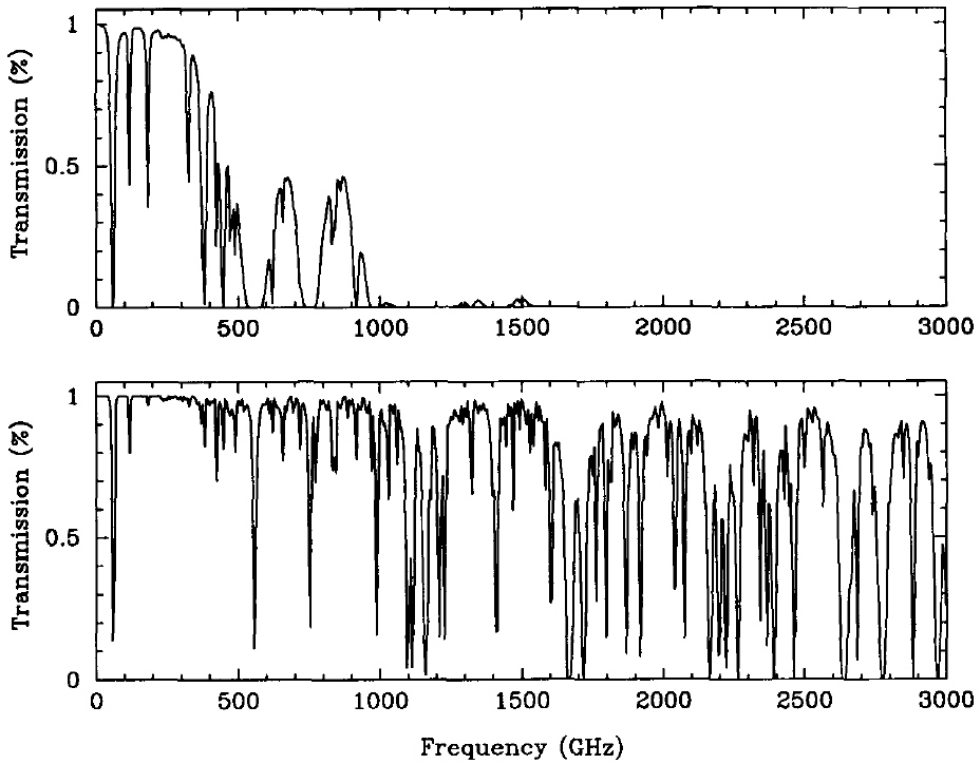

Figure 1.1: (Upper) Atmospheric transmission at Mauna Kea at an altitude of 4200 m, with 1 mm of precipitable water. (Lower) Atmospheric transmission from the Kuiper Airborne Observatory at an altitude of 12000 m. 3000 GHz corresponds to a wavelength of 100 μm. [5, 6].

1.1.1 Submillimeter Wave Astronomy

The submillimeter band is a critical and rich band for astronomy. It contains spectral and spacial information on the cosmic background, on very distant newly formed galaxies, and on the early stages of star formation within gas clouds in our own galaxy. Stars are known to be formed within the dense molecular and dust regions of the galaxy and later release much of their outer heavily processed envelopes, back to the interstellar medium. Therefore the atomic and isotope abundances of the interstellar medium provide information on the nature of the star-formation process and the degree of the star-formation activity which a given region has gone through. In addition, a critical factor in the star-formation process itself, is the gas cooling mechanism, since a cloud cannot collapse all the way to form a star unless it can rid itself of the heat of its compression under gravity. Such cooling is provided by a variety of molecular transitions in the

submillimeter band [1]. Measuring lines of different excitation states for a given molecule in the cloud and comparing their intensities allows in fact a determination of the interstellar gas temperature, while a lines intensity is a measure of the concentration of molecules along the line of sight [2].

We can immediately see the importance of the submillimeter band to star-formation studies by noting that the temperatures of the dense interstellar gas range from about 10 K to 200 K. Corresponding frequencies ($h\nu \sim kT$) range from about 200 GHz to 4 THz. This same range also corresponds to many interesting molecular rotation and atomic fine-structure transitions.

An overall view of the spectrum of a dense interstellar cloud in our own galaxy provides a sense of the spectroscopic requirements for astronomers. Figure 1.2 shows a schematic representation of the likely emission from a typical star forming cloud in the galaxy. The cloud dust

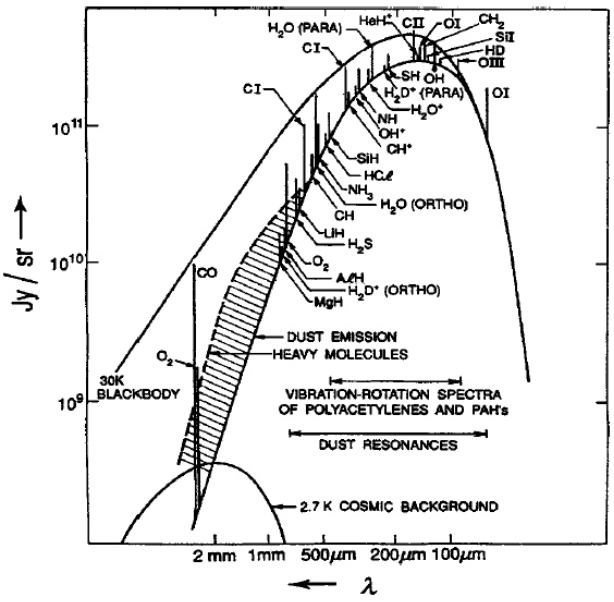

Figure 1.2: A schematic presentation of some of the spectral content in the submillimeter band for an interstellar cloud (Radiated energy versus wavelength). The spectrum includes dust continuum, molecular rotation line and atomic fine-structure line emissions [1, 3].

and gas temperatures are assumed to be 30 K. A black body curve bounds the emission strength. Besides the continuum emissions, interstellar dust clouds likely emit some 40000 individual spectral lines, only a few thousand of which have been resolved and many of these have not been identified [3]. Moreover, red-shifted spectral lines from the early universe appear strongly in the submillimeter region where they are less obscured by intervening dust that often hides our view of galactic centers.

[1]This is mostly due to the CO and H_2O molecules. It also may be provided by atomic species such as neutral and ionized carbon and oxygen [1].

A second challenge for submillimeter astronomy is to develop sensitive detectors. Since the submillimeter band lies between the microwave and infrared, technologies used in those two fields can be borrowed and adapted.

Detection of dust emission and cosmic background radiation which are continuum type of emissions, can be done by bolometers, which are borrowed from infrared astronomy. They have high sensitivity, but low frequency resolution, which is suitable for that purpose. They employ the fact that incoming radiation causes a small change in their 'temperature' which changes their electrical resistance. However, for spectroscopic investigation of atomic and molecular lines, very high resolution ($\Delta f/f \sim 10^{-6}$) is required. Therefore the heterodyne detection techniques used in microwave technology should be pushed up into the submillimeter band. Heterodyne receivers down convert the radiation to lower frequencies, which are technically easier to manage. In this process the phases of the waves are preserved, which allows narrow spectral lines to be resolved.
Two actual examples of such spectroscopical observations are shown in Fig. 1.3.

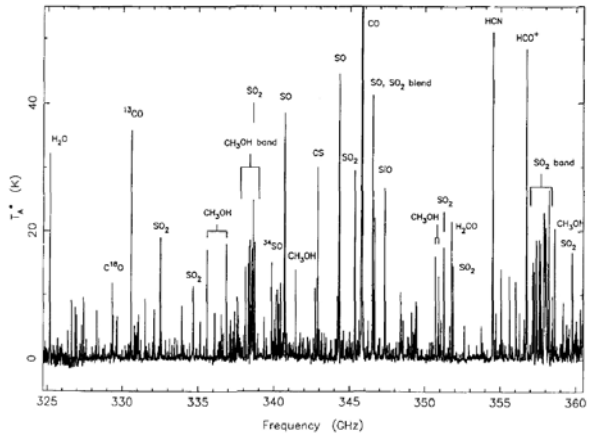

(a) A sample survey of the Orion Molecular Cloud emission in the frequency range 325 to 360 GHz, using an SIS receiver and the Caltech Submillimeter Observatory which resulted in detection of 900 lines [7].

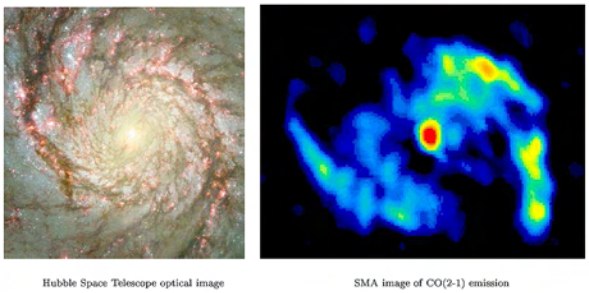

(b) Galaxy M51 as observed (left) at optical wavelengths by The Hubble Space Telescope, and (right) at 230 GHz (wavelength 1 mm) by the SubMillimeter Array. The observed emission in (right) is entirely due to the 2-1 spectral line of the carbon monoxide (CO) present in M51. The colors represent the intensity of emission, and hence the density of the CO gas. Comparison shows that the CO is densest along the dark spiral arms seen in the left picture [9].

Figure 1.3: Molecular emission spectrum examples.

Up to the year 2001, more than 120 different chemical compounds were identified in interstellar clouds, circumstellar matter, and comets, each one telling its own story about the chemistry and physics where it was found. The complete list of all interstellar molecules identified to 2006 can be found at [8].

Submillimeter Telescopes

Submillimeter telescopes need to be built at high altitudes where the atmosphere is more transparent. Telescopes like the James Clerk Maxwell Telescope (JCMT) at 15 m diameter and the

Caltech Submillimeter Observatory (CSO) at 10.4 m diameter are operating at an altitude of 4200 m on Mauna Kea, Hawaii. Since the atmosphere is more transparent at higher altitudes, airborne observatories like the NASA Kuiper Airborne Observatory (KAO) or the Stratospheric Observatory for Infrared Astronomy (SOFIA) on board of an airplane have been designed. However, the ideal observatories are space-borne. Several space-borne missions are now under construction or in planning. Herschel originally named 'FIRST' for 'Far Infrared and Submillimeter Telescope' is a 3.5 m ESA space telescope scheduled to be launched in 2007.
The Atacama Large Millimeter Array (ALMA) is the world's largest interferometric telescope currently under construction, which has been the science drive behind this thesis work. In the next section, ALMA will be reviewed briefly.

1.1.2 Atacama Large Millimeter Array (ALMA)

The purpose of this thesis work, is to aid in the design, modeling, and fabrication of a specific type of receiver (SIS) for the Atacama Larga Millimeter Array (ALMA) interferometer, currently under construction in the Atacama desert in Chili, located at an altitude of 5000 meter, which is probably the world's driest place. ALMA consists of 64 telescopes, each having a 12 meter wide dish. The ALMA antennas will be movable. At its largest, the array will measure 14 km, and at its smallest, only 150 m. Each telescope has 10 different detectors, each of which is designed to cover a portion of the electromagnetic frequency range between 30 - 950 GHz. This thesis work is for the so called 'Band 9' of ALMA, which is the frequency range between 602 - 720 GHz, and is the highest band in the ALMA baseline project. The ALMA Band 9 receiver is a compact unit containing the core of a heterodyne receiver front-end that can be easily inserted into and removed from the ALMA cryostat. In particular, its core technologies include low-noise, broadband SIS mixers; an electronically tunable solid-state local oscillator; and low-noise cryogenic IF amplifiers. The 10 frequency bands in the atmospheric windows and an artists view of ALMA are shown in figure 1.4.

Three scientific requirements stand out in all the scientific planning for ALMA. These three 'primary' science requirements are:

1. The ability to detect spectral line emission from CO or C II in a normal galaxy like the Milky Way at a redshift of z=3, in less than 24 hours of observation.

2. The ability to image the gas kinematics in protostars and protoplanetary disks around young Sun-like stars at a distance of 150 pc. [2]

3. The ability to provide precise images at an angular resolution of 0.1" [10].

These requirements have driven ALMA to its current technical specifications, which are given in Table 1.1.

[2]One Parsec (pc) is approximately 3.26156378 light years.

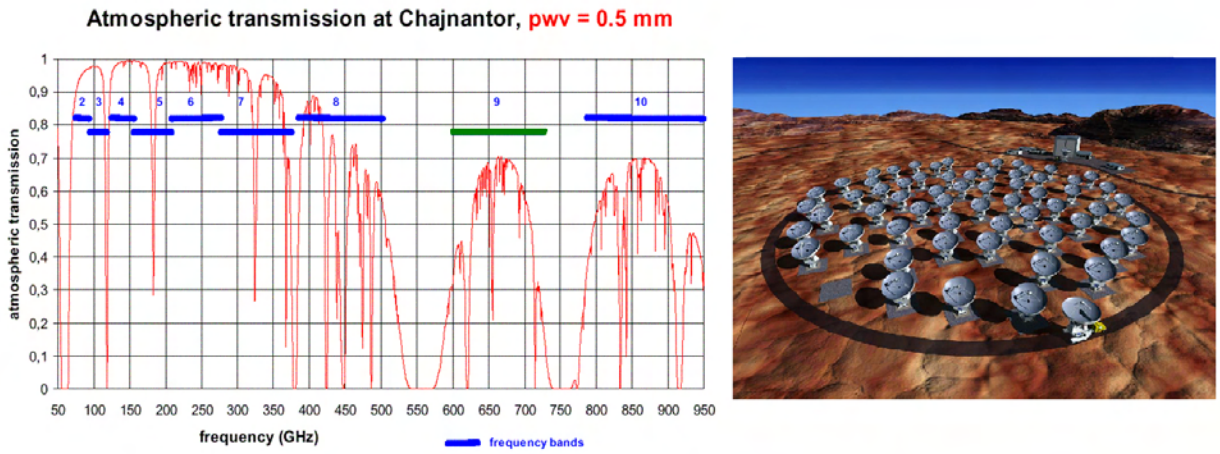

Figure 1.4: (Left) ALMA's 10 frequency bands which correspond to the atmosphere's transparency in each band. The precipitable water vapor column density is 0.5 mm. Band 9 (602-720 GHz) is marked in green. (Right) An artists impression of ALMA in the Atacama desert in Chili at an altitude of 5000m.

Table 1.1: ALMA Specifications [10]

Summary of Important ALMA Technical Specifications	
Frequency	30 to 950 GHz
Bandwidth	8 GHz, fully tunable
Spectral resolution	31.5 kHz at 100 GHz
Spatial resolution	<0.01"
Sensitivity	The ALMA receivers shall be close to quantum limited, with SSB receiver temperatures of: $\alpha h\nu/k + 4K$ with $\alpha = 10$ over the central 80% and $\alpha = 15$ for the outer 20% of the band for bands 9.
Site	Atacama desert to take advantage of the extremely dry conditions, which derive from the transparent and stable atmosphere over the site
Antenna	50 antennas of 12m diameter

1.2 Heterodyne Detectors

At millimeter and submillimeter wavelengths it is very difficult to build amplifiers. Instead mixers are used to convert the high frequency signal (RF) to a lower frequency, known as the intermediate frequency (IF), which can be amplified. Once the signal has been amplified, it can be processed further without adding any noise. The combination of the mixer, IF-amplifiers and subsequent signal processing equipment is called a heterodyne receiver. Incoherent detectors can also be used at millimeter and submillimeter wavelengths. They measure the signal over a large bandwidth. Spectral information about the signal can be obtained by filtering the radiation

prior to detection, but since filters at such high frequencies are not sharp enough, the result does not have high resolution. In contrast, heterodyne systems have typically very high frequency resolution. For astronomers this means that narrow molecular emission lines can be resolved.

1.2.1 Heterodyne Principle

In order to downconvert a high frequency signal to an IF signal, the signal, together with a coherent local oscillator (LO), is applied to a nonlinear 'diode' like device. If the local oscillator power is large compared to the signal power f_s, there will be an output at all frequencies $f = nf_{LO} \pm f_s$ where n is an integer. The LO is typically a frequency very close to the signal frequency of interest. The mixer is usually designed so that all of these frequencies are terminated reactively, except the signal, LO, and intermediate frequencies, where the IF is $f_{IF} =\mid f_s - f_{LO} \mid$. These signals are shown schematically in figure 1.5. Mixers can respond to radiation that is at a frequency

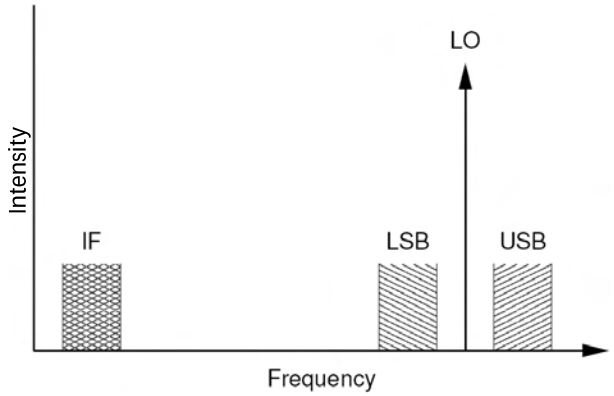

Figure 1.5: A schematic view of heterodyne mixing. The receiver is driven by a strong local oscillator signal. Any signals in the upper or lower sidebands (USB and LSB) are downconverted into the intermediate frequency band.

$f_s = f_{LO} + f_{IF}$;this is called the upper sideband (USB). Similarly, mixers can also respond to lower sideband (LSB) which is $f_s = f_{LO} - f_{IF}$. All receivers down-convert both the upper and lower sidebands (also called the signal and image sidebands) to the IF. If the response to both sidebands is equal, the receiver is called a double sideband receiver (DSB). If the response to one is suppressed significantly relative to the other, the receiver is called a single sideband (SSB) receiver.

A complete heterodyne receiver system contains five key components (figure 1.6):

- An antenna to couple to incoming signal to the detector circuit
- A local oscillator source to provide the reference signal
- A component to combine the LO and in coming signal
- The non-linear mixing element

- A system for amplifying and reading out the down-converted signal

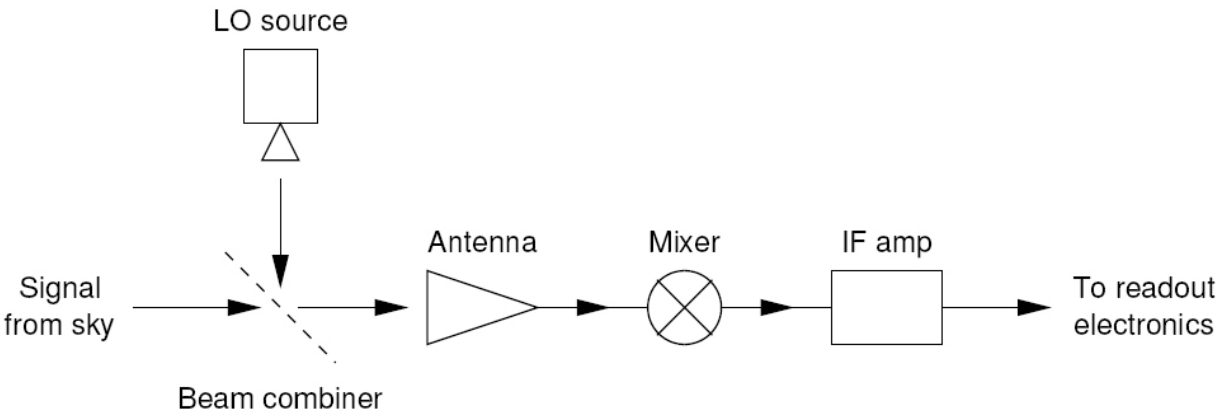

Figure 1.6: A schematic diagram of a heterodyne receiver system.

1.2.2 Mixer Figures of Merit

In order to compare receivers, their response and sensitivity must be quantified. For this, we will look into several key figures of merit for mixers:

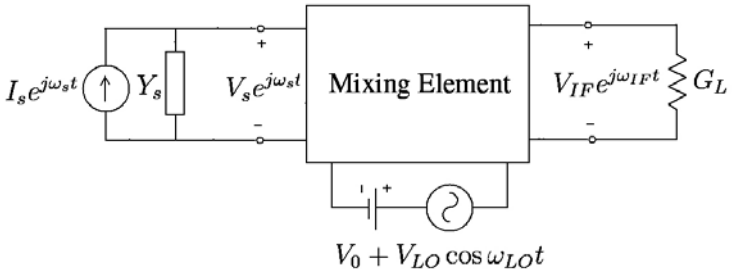

Figure 1.7: Schematic diagram of a mixer. The different ports are distinguished in frequency; in their physical realization they might all be carried out on the same pair of wires.

1. ***Mixer Gain:*** Figure 1.7 shows a schematic diagram of a basic mixer circuit. A mixer has as its input a signal at some high frequency, f_s. That signal is represented by an ideal sinusoidal current source with complex amplitude I_s, shunted by the signal source admittance $Y_s = G_s + jB_s$. The signal power available to the mixer [3] from this source is:

$$P_{avs} = I_s I_s^* / 8G_s \tag{1.1}$$

[3]This is the maximum power that the source can deliver to the mixer. This happens when the source and mixer input impedances are matched.

The source causes a signal voltage V_s to be developed across the mixing element.
A local oscillator (LO) induces a voltage V_{LO} across the mixing element at the LO frequency, f_{LO}. For linear mixing, it is assumed that $|V_{LO}| \gg |V_s|$. In mixing, V_{LO} is held constant so that variations in the amplitude and phase of V_s, can be detected. The LO provides the natural phase reference for the mixer, so it makes sense to define V_{LO} to be a pure real phasor. There is also a dc bias voltage, V_0, applied to the mixing element.
A linear mixer produces an IF signal voltage $V_{IF} = \Gamma V_s$ where Γ is the voltage gain of the mixer. The mixer output V_{IF} contains both the amplitude and phase of the input signal V_s. The IF signal power is the signal power delivered to a load admittance G_L attached across the IF port of the mixer: $P_{IF} = 0.5 G_L V_{IF} V_{IF}^*$. In a real mixer, G_L is the input admittance of a following IF amplifier.
Although defined above in terms of a voltage gain Γ, mixers are usually described in terms of their power gain,

$$G = P_{IF}/P_s, \tag{1.2}$$

also called the conversion efficiency. In most mixers, G is less than 1. Because of this, the mixers conversion efficiency has traditionally been referred to as its conversion loss, which is just G^{-1}.

2. ***Mixer Noise:*** Real mixers are not perfect; they add white noise to the signal they are detecting. Including a noise source in the mixer, its output voltage is $\Gamma V_S + V_N$. Being noise, V_N , has a fluctuating phase and amplitude, and is best characterized by its root mean square value $\overline{V_N^2}$. The noise voltage induces an extra power in $G_L : P_N = \overline{V_N^2} G_L$. Since it is white noise, P_N rises linearly as the bandwidth B of the IF is increased.
The noise described above originates in the mixer or in the mixing process, and so it can only be detected at the output of the mixer. However, it is common and useful to refer that noise to the input of the mixer so that its effect on the sensitivity of the mixer is emphasized. The mixer described above behaves identically to a noiseless mixer which has $V_S + V_N \Gamma^{-1}$ at its input. This fictitious noise source at the input has an available noise power

$$P_M = P_N/G. \tag{1.3}$$

P_M is called the minimum detectable power of the mixer [26]. However, the usual parameter to describe the noise in a mixer is

$$T_M = P_M/k_B B, \tag{1.4}$$

where k_B is Boltzmanns constant. T_M is called the mixer noise temperature referred to the input or just the mixer temperature [4].

[4]There exists an important point of concern that usually causes confusion. Here I would like to make that clear: Mixer noise temperatures are sometimes referred to as SSB or DSB mixer noise. Mixers can generally detect both the upper and the lower side-band signals. If the conversion gain for both bands is equal, the mixer is called a DSB mixer. In this case, we can define a double side band gain $G_{DSB} = 2G_{SSB}$. Since the noise at the output of the mixer , P_N, is not changed by how the signal is defined, the DSB mixer has a lower noise referred to it's input: $T_{M,DSB} = T_{M,SSB}/2$. Both these figures can be used to describe the DSB mixer. But for a SSB mixer, a DSB

3. ***Receiver Noise:*** A complete SIS heterodyne receiver consists of an SIS mixer followed by a high-gain, low-noise IF amplifier. Like the mixer itself, the IF amplifier has a characteristic gain G_{IF} and noise temperature referred to its input T_{IF}. The total receiver has a gain $G_{REC} = G \times G_{IF}$. The total receiver has a noise temperature referred to its input

$$T_{REC} = T_M + T_{IF}/G. \tag{1.5}$$

In practice, the antenna, the local oscillator, the atmosphere, and the cosmic background radiation also add noise which should be added to the receiver noise. Receivers are usually used to detect signal powers which are much less than $P_{REC} = k_B T_{REC} B$. This is done by integrating the output power of the receiver for a time τ. If the signal has an equivalent temperature of T_{in}, the signal to noise ratio of the receiver is given by Dicke's radiometer equation [27]

$$\frac{S}{N} = \frac{T_{in}}{T_{REC}}\sqrt{\tau B} \tag{1.6}$$

where B is the instantaneous receiver bandwidth (IF bandwidth). Therefore, the receiver is capable of detecting

$$\delta T_{REC} = T_{REC}/\sqrt{\tau B} \tag{1.7}$$

with a signal to noise ratio of unity. This is called the radiometric or spectral resolution of the receiver. Note that τ can not be increased infinitely, because it is limited by the stability of the integrators and other elements. It is very important to notice that by halving the receiver noise temperature, a particular measurement can be made with the same accuracy in either a quarter of the time, or with four times the spectral resolution [5].

1.3 Terahertz Sensor Technology

Terahertz sensor technology has evolved much faster than any other submillimeter technology. The critical difference between detection at at THz frequencies and shorter wavelengths lies in the low photon energies (1-10 meV). This means that the ambient background thermal noise almost always dominates the naturally emitted narrow-band signals, requiring either cryogenic cooling of the detector elements or long-integration times in order to gather enough coherent information from the source. On one hand diffraction effects in THz frequencies are too high to be able to use optical technology for terahertz sensors, and on the other hand the traditional microwave technology and components is not available for this frequency range. Therefore, terahertz sensors suffer from a lack of available electronic components like lumped resistors, capacitors, and inductors, as well as amplifiers and low-loss transmission media [6]. Currently there are two main types of terahertz heterodyne sensors which will be described briefly below:

noise temperature can not be defined and is meaningless. When nothing is said about the type of mixer, generally it is a DSB mixer

[5]For example the JCMT telescope was capable of taking a map around the Orion nebula with it's new camera in just 40 minutes, while with the older recievers installed this would have taken nearly a month [47].

[6]For example, low noise amplifiers currently are not available for frequencies higher than 150 GHz. For this purpose cryogenic InP High-Electron-Mobility-Transistor amplifiers are used [15].

1.3.1 Semiconductor Heterodyne Sensors

For some applications like earth and planetary sciences, the sensitivity offered by semiconductor sensors is generally adequate for reasonable that purpose. For passive systems, heterodyning is used to increase signal-to-noise ratio by reducing bandwidth. Mixing is done with a semiconductor non-linear element (crystal rectification) and then post IF amplification.
For applications where the sensitivity of room-temperature detectors is adequate, the basic single Schottky diode mixer is the preferred downconverter in the terahertz frequency range. But Schottky mixers have several disadvantages. They require high local oscillator powers ($\sim$0.5 mW of RF power at THz), which is basically a lack of powerful terahertz sources, and is currently a hot research topic [45, 46]. Moreover, their inherent noise is fairly large, and their conversion gain is small. Both of these will degrade the SNR of the IF signal. [7]

1.3.2 Superconductor Heterodyne Sensors

High-sensitivity detectors must rely on cryogenic cooling for operation in the terahertz range. Several superconducting heterodyne detectors have been developed including those based on the Josephson effect [21], superconductor-semiconductor barriers (super-Schottky [22]), and bolometric devices [23]. However the superconducting equivalent of the Schottky diode downconverter is the superconductor - insulator - superconductor (SIS) tunnel junction mixer which is the detector type used in this thesis. The current flow mechanism is based on the photon-assisted tunneling process discovered by Dayem and Martin [24] in the early 1960s and analyzed by Tucker [26] in the late 1970s (A detailed analysis will come in the next section). SIS mixers are widely used at frequencies from 100 to 1200 GHz [30] at observatories around the world. Like the Schottky diode downconverter, the SIS mixer relies on an extremely nonlinear I-V characteristic created by the sharp onset of tunneling between the single-electron quasi-particles on either side of a thin superconducting gap. The tunneling process is nonclassical and the sensitivity limit (equivalent mixer noise temperature) is governed by the Heisenberg uncertainty principle [26]. Sensitivities for the SIS mixers fall close to the quantum limit ($T_{M,quantum-limit} = h\nu/2K_B \approx$ 0.05K/GHz) for frequencies up to several hundred gigahertz and are within a factor of ten of this limit up to 1 THz. A selection of noise temperature results for SIS receivers achieved between 200GHz and 1.3 THz for on various recently or nearly completed telescopes is shown in figure 1.8.

An additional advantage of the SIS mixers is the very modest LO power requirement compared to Schottky diodes. They require on the order of microwatts, rather than milliwatts, for a single device.
SIS devices reach a natural frequency limit f_{cutoff} at twice the superconducting energy gap (4Δ)

[7] Receivers based on room-temperature Schottky diode mixers typically have radiometric resolution (δT) near 0.05 K at 500 GHz and 0.5 K at 2500 GHz for a 1-second integration time and a 1-GHz predetection bandwidth, and input referred noise powers as low as 5000 K at 2500 GHz [16]. This is sufficient for detecting many naturally occurring thermal emission lines. For detailed design and performance reviews of schottky mixers, refer to [17, 18, 19, 20].

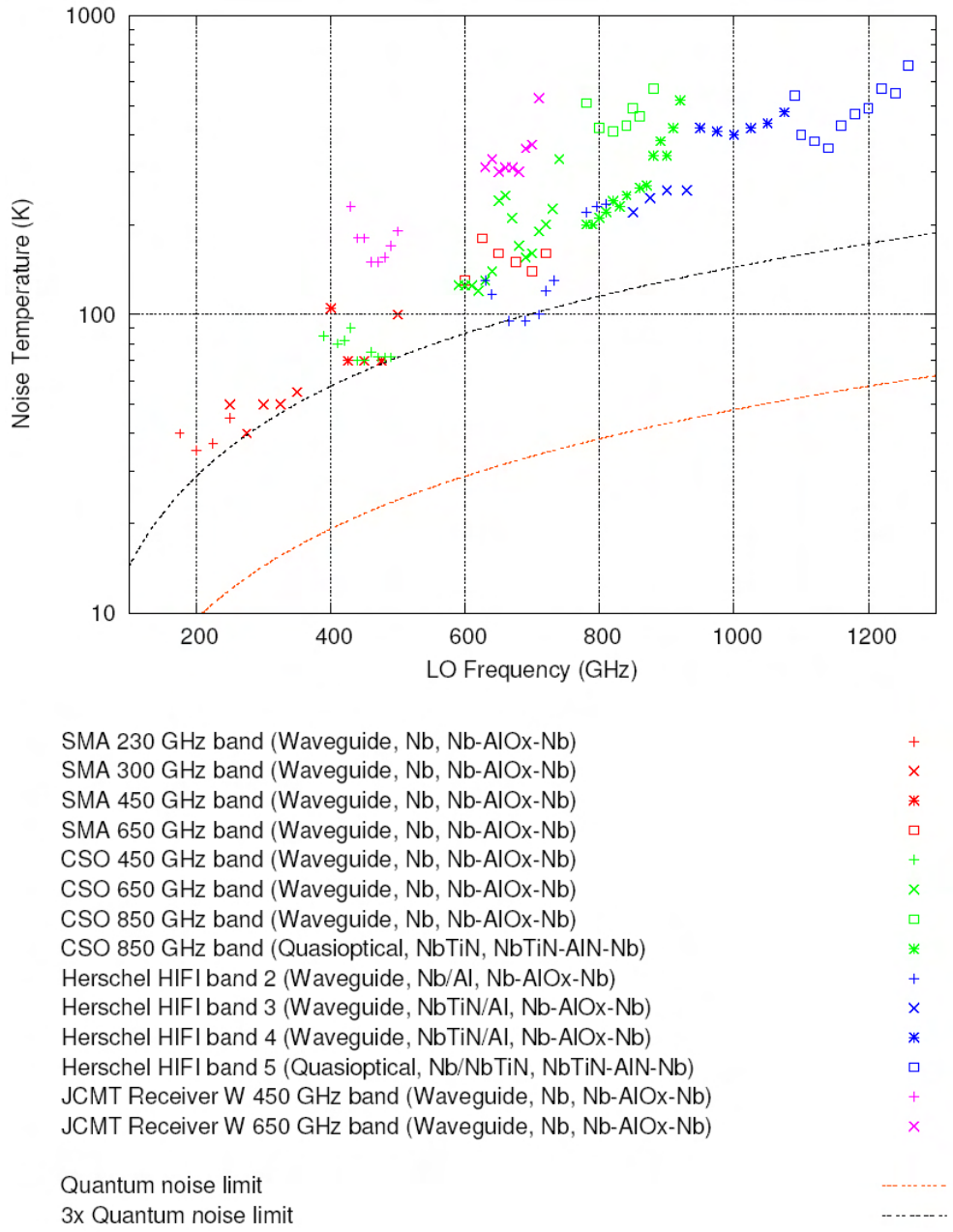

Figure 1.8: Noise temperatures reported for a selection of SIS receivers for use on various telescopes worldwide. The included telescopes are: the Submillimeter Array (SMA, Mauna Kea, Hawaii), the Caltech Submillimeter Observatory (CSO, Mauna Kea, Hawaii), ESA's Herschel Space Telescope (HIFI instrument), and the James Clerk Maxwell Telescope (JCMT, Mauna Kea, Hawaii). The mixer type and the materials used for the device wiring and junction are shown in parantheses. (reprinted from [48]).

for temperatures well below the critical temperature [26]. This upper operating frequency is dependent upon the tunnel junction material composition which determines T_c [8].

The most common material for SIS tunnel junctions is a trilayer of niobium-aluminum oxide-niobium (Nb/AlOx/Nb)with $T_c = 9.3K$. The material technology for creating this trilayer, has been well developed during the years partly because of the interest of several different communities. Material choices for SIS mixers will be discussed in section 2.4. Nb/AlOx/Nb and Nb/AlN/Nb devices are the choice in this thesis work.

[8]The superconducting energy gap, 2Δ, is approximately equal to $3.52k_BT_c$ for many superconductors.

Chapter 2
SIS Mixers

An SIS tunnel junction consists of two superconducting electrodes separated by a very thin insulating layer typically 1 nm thick. Electrons in one electrode can tunnel through the insulator into the other electrode. SIS mixers require very low LO power and are the lowest noise mixers up to 1.2 THz.
This section discusses the basic physics behind SIS tunnel junction mixers. We will begin with an introduction to superconductivity. The unusual density of states for the superconductors, causes SIS tunnel junction to have extremely non-linear current–voltage (I-V) characteristics. This extreme non-linearity leads to several phenomena, which can only be described by using a quantum mechanical theory. This theory and these phenomena are described in detail.

2.1 Physics of SIS Tunnel Junctions

We will first give a short simple summary of the physics of superconductivity and its origin. Superconductivity is caused by a small attractive force between conduction electrons in a metal. In a conventional superconductor, this attractive force is controlled by the electron–phonon interaction. Below the superconducting transition temperature (T_c), the electrons near the fermi energy form bound pairs, called Cooper pairs because of this interaction [31]. The distance over which these pairs are correlated in is called ξ and is know as the coherence length. Because ξ is much larger than the average distance between electrons in a solid, one Cooper pair overlaps many others. This overlap causes a correlated state over the whole solid. Moreover, the Cooper pairs have a net spin of zero, so they act like bosons and not like fermions. Therefore, all the pairs will condensate into one single ground state. These pairs can carry current without any dissipation of energy. A microscopic theory to explain this phenomena was given by Bardeen, Cooper, and Schriffer in 1957 [32]. To create an excitation from the ground state, a Cooper pair is broken into electrons. The lowest energy state for the excited electrons is an energy Δ above the Fermi energy; therefore the lowest excitation energy for the system is 2Δ, because there are two electrons in a Cooper pair. This excitation energy is called the superconducting energy gap. The density of the excited states as function of energy is shown in figure 2.1. There is an infinite density of states at the edges of the energy gap. The density of states shown in this figure is fre-

quently called the semiconductor picture of a superconductor. The Cooper pairs are not shown in this diagram; they are all at the Fermi energy. In the ground state of the superconductor, all the electronic states below the energy gap are filled and all the electronic states above the energy gap are empty. The semiconductor picture of a superconductor is a very simple way of describing superconductivity and is only useful for this purpose. In a superconductor, the excitations are called quasi-particles. Quasi-particles act in most ways like electrons, but they have a finite lifetime and they will decay back into the pair states. An introduction to superconductivity is given by Tinkham [33].

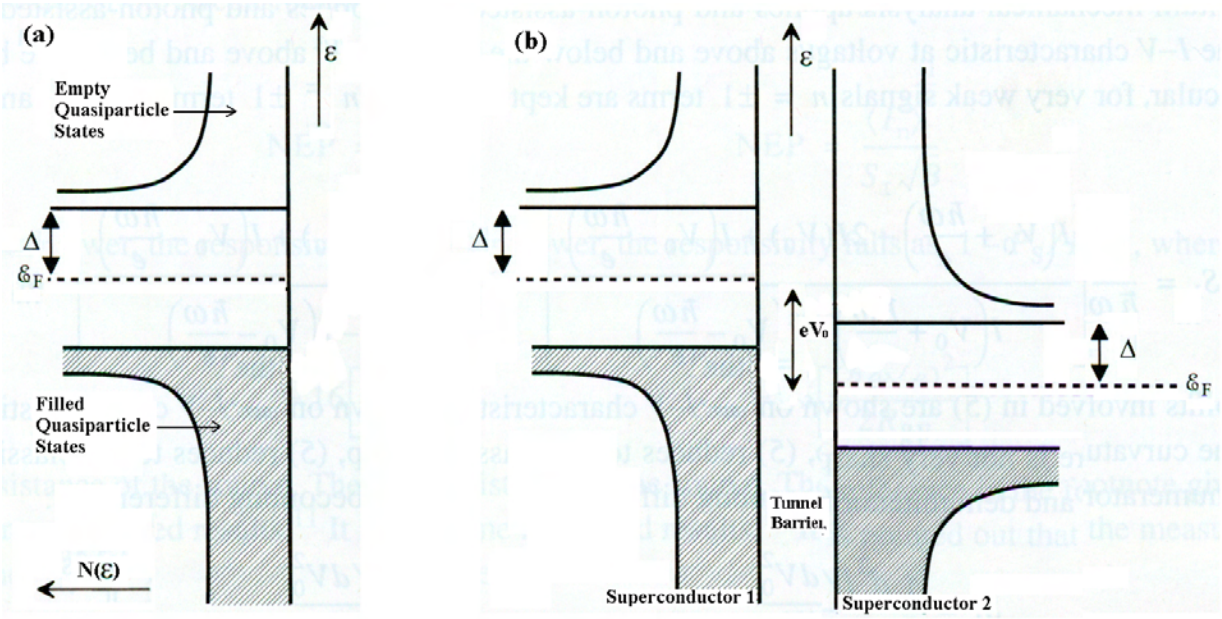

Figure 2.1: SIS Tunneling. Figure (a) shows the semiconductor picture of the BCS density of states at 0 Kelvin which has a square-root singularity at the gap edges. Figure (b) shows the semiconductor picture of an SIS junction biased below the gap voltage.

The Semiconductor picture can be used to understand SIS tunnel junctions. Figure 2.1 shows the semiconductor picture of an SIS tunnel junction biased at a voltage V_0. At this voltage, there are no empty states for the quasi-particles in superconductor 1 to tunnel into. When the bias voltage is raised to the gap voltage ($V_0 = (2\Delta/e)$, the filled states at the gap edge in superconductor 1 can tunnel into empty states at the gap edge in superconductor 2. The onset of tunneling current at this volatge is abrupt, because there are singularities in the density of states at both gap edges. At voltages above the gap voltage, the current rises approximately with a characteristic resistance R_n, referred to as the normal-state resistance of the device. Using the BCS expression for the density of states and the tunneling probabilities, the I-V characteristics for a SIS tunnel junction can be calculated [33]. The tunneling probability (T) is equal to an overlap integral for the states on both sides of the barrier. All possible tunneling channels are summed over to obtain the total tunneling current for a given bias voltage. The I-V characteristics of a junction at 0

Kelvin is shown in figure 2.2.

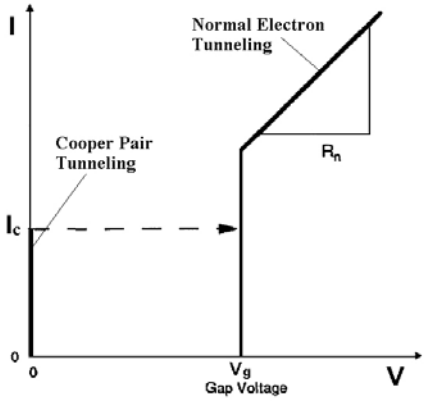

Figure 2.2: Ideal SIS junction I-V characteristics at 0 K.

SIS tunnel junctions have nearly perfect I-V characteristics for heterodyne mixing. The optimal I-V characteristic for a classical mixer is a switch, which conducts no current below a certain bias voltage, and above this bias voltage the current turns on abruptly. This happens in an ideal SIS I-V characteristic at the gap voltage. In real SIS junctions, the turn on of the current is not perfectly sharp, but typically occurs over a fraction of a millivolt. The nonlinearity in SIS tunnel junctions is much sharper than the non-linearity in semiconductor diodes, which makes them the perfect candidate for heterodyne mixing.

2.2 Photon Assisted Tunneling

When a tunnel diode has an extremely nonlinear I-V characteristic, classical mixer theory breaks down, and a quantum mechanical treatment is necessary. The frequency where classical theory fails depends on the voltage range over which the current is a non-linear function. In SIS junctions, quantum mechanical effects have been experimentally observed at frequencies as low as 30 GHz ([34]). To explain these effects, a quantum mechanical theory for mixers was developed by Tucker [26]. Before considering the complete quantum mixer theory, we will first have to explain the principle of the photon-assisted tunneling effect. This effect was discovered experimentally by Dayem and Martin [24] and explained by Tien and Gordon [25].

Suppose that one side of the junction is grounded, and consider the Schrödinger wave function representing a single-electron quasi-particle eigenstate on the opposite side of the tunnel barrier. When a a high frequency ac signal is applied to the SIS junction which is biased at a voltage V_0 (Fig. 2.3), the time dependent voltage across the junction will be:

$$V(t) = V_0 + V_\omega \cos \omega t \tag{2.1}$$

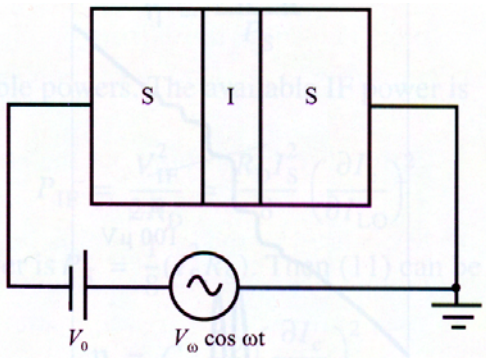

Figure 2.3: SIS tunnel junction with time-varying voltage biasing.

This applied voltage will modulate the potential energy of each quasi-particle level. The time dependence of the wave function for every one-electron state will therefore be modified according to:

$$\begin{aligned} \psi_i(x,t) &= \psi_i(x) \exp\Big\{ -\frac{i}{\hbar} \int^t dt' [E_i + eV(t')] \Big\} \\ &= \psi_i(x) e^{\frac{-i}{\hbar}(E_i + eV_0)t} \times \sum_{n=-\infty}^{\infty} J_n\Big(\frac{eV_\omega}{\hbar\omega}\Big) e^{-in\omega t} \end{aligned} \tag{2.2}$$

where E_i is the unperturbed energy of the Bloch state, and J_n is the Bessel function of the first kind. The modulation of the Fermi sea on this side of the junction can thus be viewed in terms of a probability amplitude $J_n(eV_\omega/\hbar\omega)$ for each quasi-particle level to be displaced in energy by $n\hbar\omega$. The interpretation of Eq. (2.2) is illustrated schematically in Fig. 2.4.

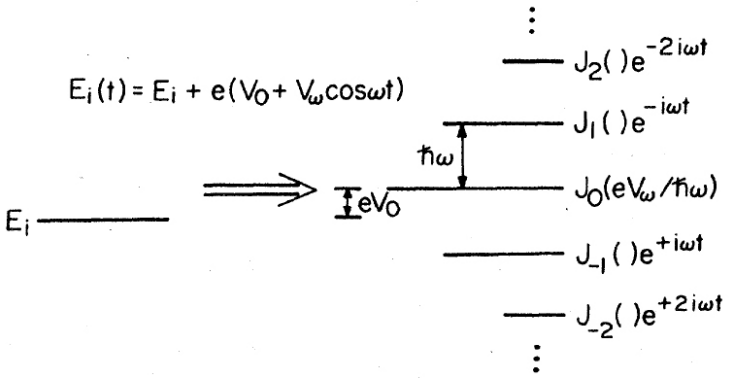

Figure 2.4: Virtual energy levels generated according to Eq. (2.2) by modulation of the energy $E_i(t)$ for each electron state within the ungrounded electrode of a SIS junction in the presence of a microwave field.

We see that each energy level becomes many levels $E_i + eV_0 + n\hbar\omega$ with probability amplitude $J_n(eV_\omega/\hbar\omega)$. A quasi-particle on the left side which, without the RF excitation, would be at too low an energy to tunnel ($V_0 < 2\Delta/e$) has its energy raised and can contribute to junction current.

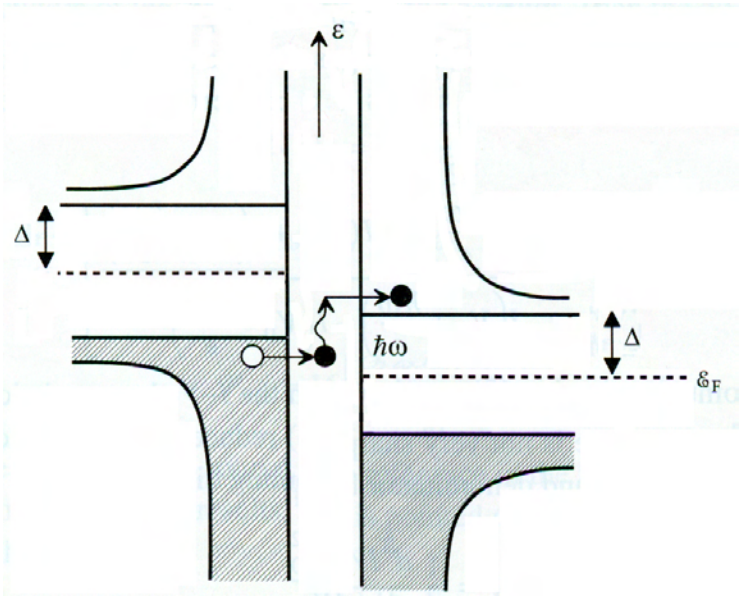

Figure 2.5: Semiconductor picture of photon-assisted tunneling at $T = 0K$.

This is suggested in the tunneling diagram in Fig. 2.5. Since all electron states are modulated together, these displacements in energy are equivalent to dc voltages $(V_0 + n\hbar\omega/e)$ applied across the junction with a probability $J_n^2(eV_\omega/\hbar\omega)$ that depends upon the ac signal amplitude. The resulting dc (total) I-V characteristic is produced by adding a set of unperturbed I-V characteristics, but shifted in voltage by $n\hbar\omega$ and magnitude set by the corresponding Bessel function. Thus the sharp step at the gap voltage V_g in the unperturbed I-V is imaged with different amplitudes. The total tunneling current will, therefore, be given by:

$$I_0(V_0, V_\omega) = \sum_{n=-\infty}^{\infty} J_n^2(\frac{eV_\omega}{\hbar\omega}) I_{dc}(V_0 + n\hbar\omega/e) \tag{2.3}$$

where $I_{dc}(V_0)$ represents the unmodulated dc I-V characteristic.
This result can be interpreted as such: the effect of the applied microwave field is to superimpose contributions from the unmodulated I-V characteristic, displaced in voltage by integral multiples of the quantum energy $\hbar\omega/e$. The resulting I-V curve, is called a pumped I-V curve and is shown in Fig. 2.6.

A more intuitive picture can be given for this process as follows: For a particular bias voltage V_0, a photon energy of at least $\hbar\omega = 2\Delta - eV_0$ is required to give a quasi-particle just below the gap enough energy to tunnel across the barrier. Therefore if the bias voltage is varied with the junction illuminated by a signal at a particular frequency ω, then a photon assisted tunnel current will be observed for voltages less than $\hbar\omega/e$ below the gap voltage. At bias voltages less than $\hbar\omega/e$ above the gap voltage, a decrement in tunneling current is seen, due to photon-assisted tunneling in the reverse direction. If the signal is sufficiently powerful, then two photons can be absorbed by a single quasi-particle, and tunneling currents can be seen at bias voltages less than

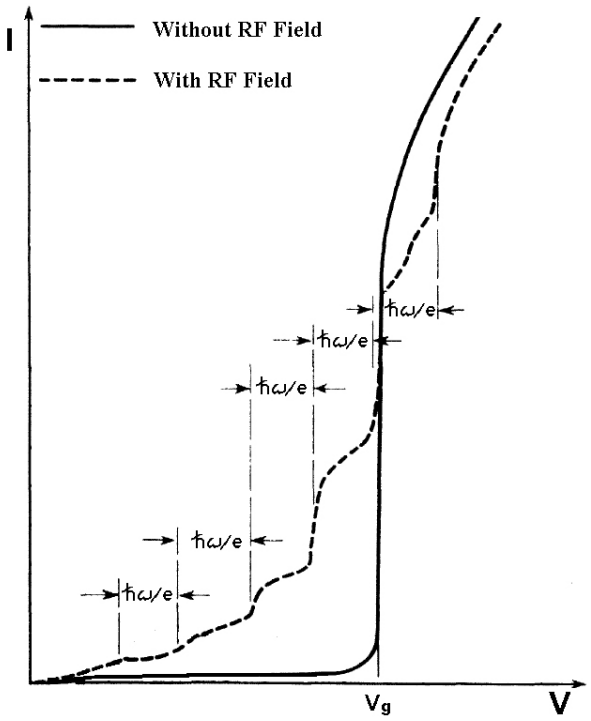

Figure 2.6: Step structure induced by photon assisted tunneling in the I-V characteristic of an SIS junction by an applied RF voltage. Rises of the steps are spaced by $\hbar\omega/e$, centered about V_g.

$2\Delta - 2\hbar\omega/e$. But since the probability of two photon absorption processes is less, the current due to it will be smaller. This argument can be extended to processes involving increasing number of photons at decreasing levels of probability.

2.2.1 Direct Detection

We will first apply Tucker's theory to the simple problem of direct detection of a coherent signal before considering the complete mixer theory.
The figure of merit for a direct detector is the current responsivity (R_i), which is defined as the change of dc current divided by the RF power absorbed (P_{RF}):

$$R_i = \frac{\Delta I_{dc}}{P_{RF}} \tag{2.4}$$

In detection, the signals are very weak and one would not see the step structure in the I-V characteristic. Still the quantum mechanical analysis applies and photon-assisted tunneling will take place. The value of the I-V at voltages above and below the bias point by $n\hbar\omega/e$ are important. In particular for very weak signals $n = \pm 1$ terms are kept and by expanding the Bessel functions in Eq. (2.3) we get:

$$\Delta I_{dc}(V_0) = \frac{1}{4} V_\omega^2 \left[\frac{I_{dc}(V_0 + \hbar\omega/e) - 2I_{dc}(V_0) + I_{dc}(V_0 - \hbar\omega/e)}{(\hbar\omega/e)^2} \right] \tag{2.5}$$

The dissipative, in-phase component of the junction current induced at the applied AC frequency (I_ω) can be derived [1] and is given by:

$$I_\omega(V_0, V_\omega) = \sum_{n=-\infty}^{\infty} J_n(eV_\omega/\hbar\omega)\Big[J_{n+1}(eV_\omega/\hbar\omega) + J_{n-1}(eV_\omega/\hbar\omega)\Big] I_{dc}(V_0 + n\hbar\omega/e) \quad (2.6)$$

In the limit of small AC amplitude, $I_\omega(V_0, V_\omega)$ can be reduced to

$$I_\omega = V_\omega \frac{I_{dc}(V_0 + \hbar\omega/e) + I_{dc}(V_0 - \hbar\omega/e)}{2(\hbar\omega/e)} \quad (2.7)$$

The RF power absorbed by the junction is $P_{RF} = 1/2 V_\omega I_\omega$. Therefore the responsivity is given by:

$$\begin{aligned} R_i &= \frac{e}{\hbar\omega}\left[\frac{I_{dc}(V_0 + \hbar\omega/e) - 2I_{dc}(V_0) + I_{dc}(V_0 - \hbar\omega/e)}{I_{dc}(V_0 + \hbar\omega/e) - I_{dc}(V_0 - \hbar\omega/e)}\right] \\ &\rightarrow \frac{1}{2}\frac{d^2 I_{dc}/dV_0^2}{dI_{dc}/dV_0}, \text{ classical limit} \\ &\rightarrow \frac{e}{\hbar\omega}\eta_Q, \text{ quantum limit.} \end{aligned} \quad (2.8)$$

Here η_Q is the quantum efficiency of the junction in analogy to a photodiode detector [28, 29]. In the case of an ideal SIS junction, $\eta_Q = 1$, $R_i = e/\hbar\omega$.
The location of the points involved in Eq. (2.8) are shown on the I-V characteristic in Fig. 2.7. It easy to show that if the curvature is not very sharp, that is, I-V changes slowly on the scale $\hbar\omega/e$, Eq. (2.8) reduces to the classical expression. This classical result would imply that a direct detector could be made arbitrarily sensitive by increasing the curvature $d^2 I_{dc}/dV_0^2$ of the dc non-linearity. Photon-assisted tunneling theory, however, demonstrates differently: if we go towards a very sharp step in the I-V characteristic, the bracket in Eq. (2.8) reduces to unity, and the responsivity becomes the fundamental quantum limited value of one electron per photon.

To explain the quantum mechanical limit, one can go back to Fig. 2.5. No current can flow at this bias voltage; however, if photons are incident on the tunnel junction, a quasi-particle can tunnel for each photon that is absorbed. This process will occur if the junction is biased at a voltage $\hbar\omega/e$ below the gap voltage or at any higher bias voltage. If two photons are absorbed, tunneling can occur at bias voltages of $2\hbar\omega/e$ below the gap voltage. This leads to a series of steps in the I-V curve at voltages $(\Delta_1 + \Delta_2)/e - n\hbar\omega/e$, corresponding to the absorption of n photons. For bias voltages slightly less than the gap voltage, one electron can tunnel per each absorbed photon, which is the quantum regime discussed above.

The sensitivity of a non-linear tunnel junction as a direct detector is limited by noise due to the bias current. For dc voltages $eV_0 > 2K_BT$ larger than thermal energies, the mean square

[1] The derivation of this equation is out of the scope of this work and the reader can refer to the full quantum mixer theory Sec. IV.C in reference [26] for the derivation.

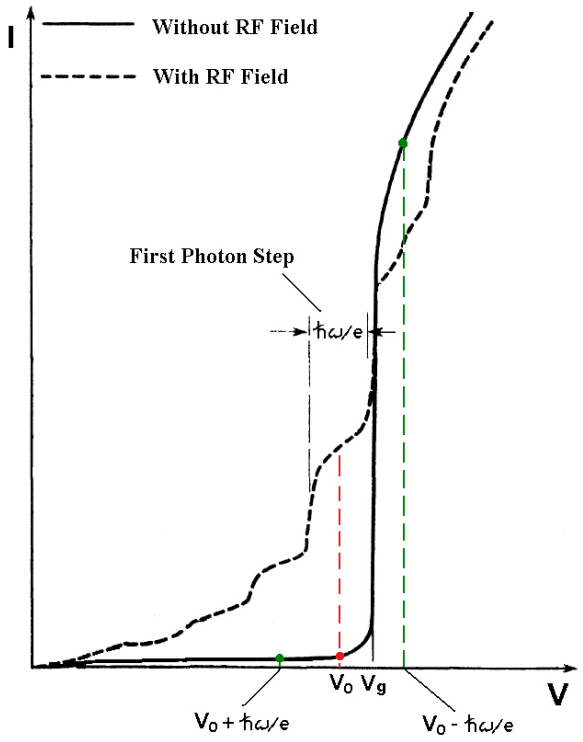

Figure 2.7: Currents and voltages in current responsivity for SIS direct detection. The bias point is located in the center of the "first photon step" of the pumped curve.

noise current is given by the usual shot-noise expression, $\langle I_n^2 \rangle = 2eI_{dc}(V_0)B$, where B represents the output bandwidth. Using Eq. (2.8), the noise equivalent power (NEP) at the input, can be estimated as:

$$\begin{aligned} NEP &= \frac{\sqrt{\langle I_n^2 \rangle}}{\eta R_i} \\ &= \frac{\sqrt{2}\hbar\omega B}{\eta}\left[\frac{I_{dc}(V_0)}{eB}\right]^{1/2}, \text{ quantum limit.} \end{aligned} \tag{2.9}$$

Here η is a factor characterizing the efficiency for impedance-matching incoming signal power into the diode. This quantum limit has a simple physical interpretation. The quantity $N = I_{dc}(V_0)/eB$ is the average number of electrons tunneling through the barrier due to the dc bias voltage during a resolution time $\sim 1/B$ determined by the output bandwidth. Since these individual events are statistically uncorrelated, the mean fluctuation in the number of electrons tunneling during this interval is $\sqrt{N}$. The quantum limited value for NEP therefore represents the absorption of $\sim \sqrt{N}$ photons per resolution time, in order to generate a signal current equal in magnitude to the average noise [2].

[2]Eq. (2.9) is in fact identical to the corresponding result for a photomultiplier, a photodiode or a photoconductor

It can be shown that in the most ideal case, the noise equivalent power in Eq. (2.9) reduces to the limit set by the Heisenberg uncertainty principle: $NEP \approx \hbar\omega B$. This is because a simultaneous measurement of amplitude and phase of an electromagnetic signal during an effective measurement time B^{-1} is limited to the detection of a single quantum within this interval with a power $\hbar\omega B$. The minimum uncertainty of a ny coherent measurement must be of this order. In fact the minimum mixer noise temperature is equal to $T_{quantum-limit} = \hbar\omega/2K_B$ [26].

2.2.2 Quantum Mixing

Tucker also extends his quantum mechanical theory to the more complicated problem of heterodyne detection. This theory is beyond the scope of this text, so I will simply give the results and provide some intuitive understanding.
The local oscillator signal causes the photon-assisted tunneling illustrated in Fig. 2.5, and has the effect on the I-V characteristics seen in Fig. 2.6.

To operate an SIS junction as a mixer, a strong LO signal is applied and the junction biased within the first photon step. A second smaller RF signal at a frequency close to that of the LO signal will beat with the LO signal, modulating the photon assisted tunneling current at a frequency equal to the difference between the two applied signals. This leads to the photon assisted tunneling current having a frequency component at this difference frequency (IF). Since the voltage across the SIS junction responds in a very non-linear way to the tunneling current, this IF frequency component can have a significant amplitude giving the mixer a the possibility of large conversion gain. We will consider two limiting situations.

If the LO and RF voltages have equivalent photon voltages $\hbar\omega/e$ smaller than the scale of the nonlinearity of the junction I-V characteristic, the mixing response is classical and can be dealt with using Taylor expansion of the nonlinearity and Fourier analysis. The maximum conversion efficiency for a classical double-sideband (DSB) mixer is 0.5 and is 1 for a single-sideband mixer [35].
However, in SIS mixers operated in the millimeter and submillimeter bands, the photon voltages may be much larger than the nonlinearity at the gap voltage, and the junction will behave differently and will respond to individual photons. That is, if the step at V_g is sharp enough to satisfy

$$\frac{e}{\hbar\omega}\left[I(V_0 + \hbar\omega/e) - I(V_0)\right] > 1/2\left[\frac{dI(V_0 + \hbar\omega/e)}{dV} + \frac{dI(V_0)}{dV}\right] \tag{2.10}$$

which involves currents and derivatives dI/dV at voltages V_0 and $V_0 + \hbar\omega_{LO}/e$ in the unmodulated I-V, then the quantum effects arise. In this case, Taylor expansion and Fourier analysis of ΔI as a function of ΔV is not possible, since variations in ΔV can only be multiples of $\hbar\omega/e$ and cannot approach zero. The result is that G, the mixer conversion gain, can be greater than unity, allowing the converted IF power to be grater than the RF signal power [3].

[3]The prohibition of conversion gains larger than unity for a classical mixer, arises solely from the assumption of instantaneous response of current to voltage. At high enough frequency, in the quantum regime, the mixing

As we saw in equation (1.5), the noise temperature of a receiver is reduced by having a larger mixer conversion efficiency G defined in Eq. (1.2). This helps in reducing the IF amplifier noise, and hence the receiver noise.

The output impedance of the mixer is the dynamic resistance R_D (inverse of the slope of the pumped I-V characteristic) at the operating voltage V_0. In figure 2.6 we see that the slope on the steps is almost zero, and the mixer acts as a nearly perfect current source. Therefore the power available to the load R_L (input impedance of the IF amplifier) is proportional to R_D, and for the matched case will be $P_{IF} = I_{IF}^2 R_D/4$. With a strong local oscillator and a nearly ideal I-V, the slopes of the tops of the steps can be nearly zero. This means very high gains are possible. But due to matching problems of R_D to the IF amplifier, gains larger than two are difficult to get [36]. Fortunately, a very large conversion gain is not required in order to approach the quantum limited sensitivity in the millimeter wave region. The "temperature" of a single energy quantum $T = \hbar\omega/k_B$ corresponds to a few degrees Kelvin at these frequencies, and a conversion gain of $G = 2 - 4$ is sufficient to reduce the contribution of a $T_{IF} \approx 10K$ amplifier below this level.

Other important factors are the required local oscillator power and the dynamic range. The typical power level for a single junction mixer is a bout 2 pW. This is very important since narrow-band local oscillator sources in the submillimeter range produce very little power. The upper end of the dynamic range of the mixer is set by the saturation level and the lower end is determined by noise. It can be shown that the noise temperature limit for quantum mixers is the quantum limit $T_{M,limit} = \hbar\omega/k_B$ set by the Heisenberg uncertainty principle [4] [26]. A collection of noise temperatures for different SIS mixers was shown in figure 1.8. It is also very interesting to note that high mixer conversion gain and low noise are not incompatible and tend to go hand-in-hand [5]. As a summary, the low inherent mixer noise and the conversion gain, lead to very low receiver noise levels for these devices, which makes them the most sensitive receivers up to 1.2 THz [30].

However, there are limitations on the performance of SIS mixers, particularly at higher frequencies. These limitations are cased by non-ideal I-V properties and by the basic physics of superconductors. The properties and limits of real SIS junctions are discussed in the next section.

2.3 Properties of Real SIS Tunnel Junctions

The previous section described the performance of mixers using ideal SIS tunnel junctions. However, real SIS junctions have properties that limit their performance. This section analyzes these limitations and their physical origins. Figure 2.8 shows a stylized version of a real SIS I-V

element's response is not perfectly instantaneous which leads to the possibility of having gains larger than unity.

[4] It can be shown that the noise added by the mixing process itself can be ultimately zero. This limits us to the noise present in the signal itself which is the zero-point fluctuations in the electromagnetic field equal to $\hbar\omega/2$.

[5] A very good intuitive reasoning of this is given on page 1076 in [26].

characteristic, as compared to the ideal I-V characteristic shown in figure 2.2.

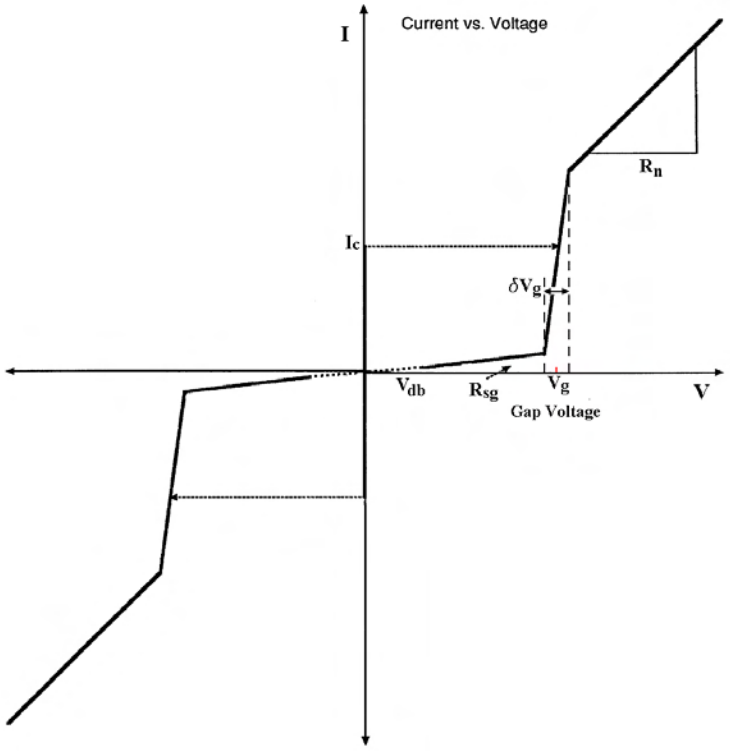

Figure 2.8: Stylized SIS I-V characteristic. This figure shows a stylized vesrion of a real I-V plot for an SIS junction. There is a finite subgap resistance (R_{sg}), a broadening of the onset of the tunneling at the gap voltage (δV_g), and the drop-back voltage (V_{db}), below which there is no stable nonzero bias voltage. Additionally, there may be an increase in the subgap leakage at half the gap voltage (which is not shown in the figure).

2.3.1 Smearing of I-V Characteristics

SIS-based mixers exhibit quantum behavior only when the I-V is extremely non-linear. Real tunnel junctions have sub-gap leakage currents and a smeared turn-on of the tunneling current at the gap voltage. Both of these non-ideal properties reduce the non-linearity in an SIS I-V characteristic. Devices that suffer from such non-idealities, show quantum mechanical behavior effects only at higher frequencies, because the photon energy has to be larger than the scale of the non-linearity in the I-V for that to happen.

The most severe problem in I-V smearing is the gap smearing (δV_g). A very simple explanation exists for this, which here I will give. Superconductivity is not a local phenomenon. In a superconductor the Cooper pairs extend over a finite region which is called the superconducting coherence length (ξ). Because of the finite size of the Cooper pair, the local energy gap of a superconductor is a weighted spatial average of the material properties in a volume ξ^3. Real

superconductors are not spatially uniform, but have imperfections such as grain boundaries, impurities, and crystal defects. If the size of these imperfections is small compared to the coherence length, the measured gap will be the spatial average of the local gap values. In this case, the gap voltage in the I-V will be reduced, but the onset of tunneling at the gap voltage will be sharp. If the scale of the imperfections is large compared to the coherence length, the measured gap will be reduced and will vary spatially. This leads to a smeared onset of tunneling at the gap voltage. To reduce gap smearing in short coherence length materials [6], it is necessary to deposit superconducting materials that are near perfect crystals.

The second form of I-V characteristic smearing, is sub-gap leakage currents. The I-V characteristic in figure 2.2 shows no sub-gap leakage currents, because the physical temperature is zero. At finite temperatures, electrons can be excited thermally, leading to sub-gap leakage currents. This leakage is very low for temperatures below $T_c/2$. However, in real junctions, there are finite sub-gap leakage currents, even at very low temperatures. There are several possible sources of this "excess" leakage current. There can be holes in the barrier that lead to parallel bridge-type weak links. There can be normal metal regions in the superconductor that lead to parallel, superconductor–insulator–normal metal (SIN) tunneling.

If there are pinholes in the barrier, there will be conduction through constricted superconductor-bridges. For a pinhole that is smaller than the coherence length, a bridge-type weak link is formed in parallel with the junction. The weak link can be modeled by the so called 'Resistively Shunted Junction' (R.S.J.) Model. Typical I-V characteristics for weak links are non-hysteretic and have only one value for the voltage for currents above the critical current [7] [38]. Now the I-V characteristic of this pin-hole will be in parallel to the SIS junction and will cause a non-hysteretic part to be added to the critical current, and will also increase the sub-gap leakage.

Sometimes leaky junctions have an increase in the sub-gap conduction at half the gap voltage. One mechanism which can lead to an increase of conduction at half the gap voltage is the existence of normal metal regions in one of the tunnel junction electrodes. This will cause superconductor–insulator–metal (SIN) conduction to happen [33]. SIN I-V characteristics, have a conductance maximum at half the gap voltage, and can explain the increase in sub-gap current at half the gap voltage.

[6] The intrinsic coherence length for Nb which is the material being used in this work, is $\xi_0 = 40nm$ at 0 Kelvin. However, the presence of impurities reduces the coherence length because of scattering. A suggested empirical relation for the reduced coherence length is

$$\frac{1}{\xi_p} \approx \frac{1}{\xi_0} + \frac{1}{\ell_e} \tag{2.11}$$

where ℓ_e is the electron mean free path, and ξ_p is the Pippard coherence length [37]. ℓ_e for Nb deposited in this work is around $\sim 5nm$.

[7] For a sample weak-link I-V curve refer to page 122 in [38].

2.3.2 High Frequency Limits on SIS Mixers

The high frequency roll-off of the detection efficiency for an SIS tunnel junction is limited by two of its properties. The junction capacitance acts as a short circuit at high frequencies, and the superconducting energy gap limits the performance through two mechanisms at high frequencies. Both of these effects will be discussed here.

The two electrodes and the barrier of a tunnel junction form a parallel plate capacitor, which forms a low-pass filter with the junction resistance. The capacitance causes the signal current to be shunted away from the non-linear tunneling element [8]. When calculating the "RC" time constant of an SIS junction, the correct resistance to use is the resistance seen at the radiation frequency, which depends of course on the bias conditions. It can be shown that the junction RF resistance is of the same order as the normal-state-tunneling resistance of the junction or R_n [26]. In this thesis, R_n is used everywhere to model the junction at RF frequencies.

The junction capacitance can be calculated trough the normal parallel plate capacitor formula, and fringing field effects can be safely neglected, since the barrier thickness ($1nm$) is much less than the plate areas ($1\mu m^2$ for AlOx barriers and $0.25\mu m^2$ for AlN barriers). Therefore,

$$C = \epsilon_0 \epsilon_r A/t = C_s A \tag{2.12}$$

where $\epsilon_0 = 8.8542 \times 10^{-12} F/m$ and ϵ_r is the relative dielectric constant of AlOx or AlN, t is the barrier thickness, and C_s is the specific capacitance. Unfortunately, the barrier thickness and the dielectric constant are not very well known. In practice, these are only estimated and the capacitance used in modeling is obtained experimentally. For AlOx barriers used in this thesis, it is taken from experimental measurements that $C_s = 80 fF/\mu m^2$ [9].

The SIS junction normal-state resistance can be easily measured. For a $A = 1\mu m^2$ and $t = 1nm$ AlOx junction, R_n values are around 25Ω [10]. If we assume the barrier to be a simple square shaped barrier, the junction normal-state resistance would be

$$R_n = \frac{h^2 t}{e^2 A\sqrt{2m\phi}} e^{(4\pi t\sqrt{2m\phi}/h)} \tag{2.13}$$

where ϕ is the barrier height, m is the mass of the electron, h is Planck's constant , and e is the charge of an electron. Now several things can be concluded from the $R_n C$ product: It does not depend on the junction area, and the RC time constant varies with the barrier thickness as $exp(t/t_0)$, because the linear thickness terms cancel out. Therefore, high speed (wide-band)

[8] It should be noted that the existence of this capacitor is useful for shunting out most of the ac Josephson current and high order harmonics that are harmful for quasi-particle mixing.

[9] Measurements of the capacitance of SIS junctions is not an easy task. One technique that can do this, is called the 'Fiske Steps' technique where the resonant modes appearing in the I-V characteristic are manipulated by a magnetic field. These resonant voltages can be related to C_s [41].

[10] However, R_n is critically dependant on the exact thickness of the barrier, and therefore can easily increase up to 40Ω.

junctions should have thin barriers and small R_nA products. Since the impedance of the embedding circuitry which surrounds the SIS junction is designed to be around 50Ω, the resistance of the junction should be of the same order, so that matching exists at RF frequencies. In this thesis work, the AlOx junctions are designed and fabricated to have R_nA products of about $25\Omega\mu m^2$, so that for an area of $1\mu m^2$ their R_n would be 25Ω. In the case of AlN junctions, they are fabricated to have an R_nA product of about $6.25\Omega\mu m^2$, so that for an area of $0.25\mu m^2$ their R_n would be again 25Ω. We see that for having resistances of the order of 50Ω, the needed areas are very small. This means that during fabrication, photolithography will be not very accurate. Therefore, in our work, electron-beam lithography has been used which is much more accurate.

The second limitation on high-frequency performance is the energy gap of the superconductors. For $\hbar\omega \geq 2\Delta$, photon energies are large enough to break Cooper pairs and create excited quasi-particles. Above this gap frequency, the resistivity of the superconductor is roughly equal to it's normal state resistivity. This implies that antenna and transmission line circuits will become lossy and will not act in an ideal manner. This will become more clear in the modeling chapter when we model the superconducting transmission lines.

At twice the gap frequency ($\hbar\omega > 4\Delta$), the junction is no longer an efficient mixer. Consider a junction illuminated by an LO signal with a photon voltage larger than the gap voltage. Then the first photon step will extend to negative bias voltages. However since the I-V characteristic is antisymmetric about the zero bias point, there will be another photon step extending from the negative side gap voltage. This negative photon step will cause tunneling in the opposite direction to the positive side photon step, and so the currents cancel (as in the low bias region of figure 2.9). This leaves a region on the photon step that is still suitable for mixing. However, if the photon frequency is increased to twice the gap voltage, then the photon steps will cancel, and no suitable bias point for mixing can be found. The junction will no longer act as a rectifier and therefore not an efficient mixer. As a result, SIS mixers are limited up to twice the gap frequency.

2.3.3 Josephson Tunneling in SIS Junctions

Both quasi-particles and Cooper pairs can tunnel in an SIS junction. All the effects described before, were quasi-particle tunneling. This is the effect that is typically used in mixers. Cooper pairs can tunnel coherently across the barrier, producing a dissipationless current at zero voltage, as is seen in figure 2.2. Pair tunneling is called the Josephson effect. A full review on Josephson tunneling and it's applications is given in [38].

For the small area junctions used in SIS mixers, two simple equations describe the Josephson effect:

$$J = J_c sin(\phi) \tag{2.14}$$

$$V = \frac{\hbar}{2e}\frac{d\phi}{dt} \tag{2.15}$$

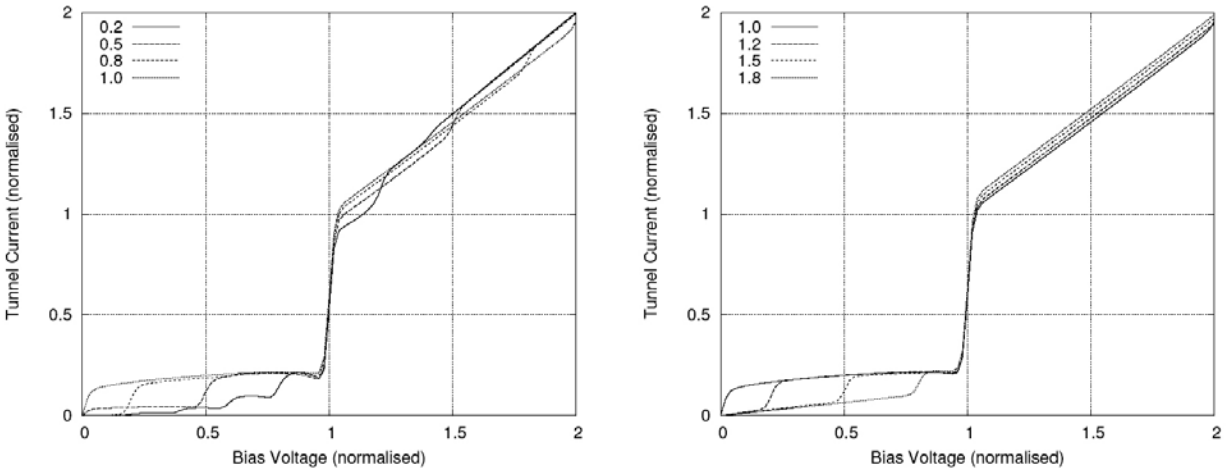

Figure 2.9: Photon assisted tunneling in an SIS junction. (Left) Photon steps at a variety of photon energies below the gap energy. (Right) Photon steps at a variety of photon energies above the gap energy (reprinted from [48]).

where ϕ is the difference in the macroscopic phase of the superconductor wave function across the barrier, and J_c is a constant determined by the area of the junction, and the barrier and superconducting electrodes material properties, and temperature as:

$$J_c(T) = \frac{\pi\Delta(T)}{2eR_nA}\tanh\frac{\Delta}{2k_BT} \tag{2.16}$$

For our Nb/AlOx/Nb SIS junctions, at $T = 0$K, $J_c^{AlOx} \approx 9.4kA/cm^2$ and for our Nb/AlN/Nb junctions $J_c^{AlN} \approx 37.7kA/cm^2$. The most obvious effect of Josephson tunneling is the finite current at zero voltage. At zero voltage, ϕ can take on any constant value, and the current density can vary between $+J_c$ and $-J_c$. The Josephson supercurrent is a dissipationless tunneling of pairs across the barrier. A second effect is that if the junction is biased at a dc voltage (V_0), $\phi = \phi_0 + 2eV_0t/\hbar$, and the current will oscillate at a frequency $f = 2eV_0/\hbar$.

The Josephson effect causes two problems in SIS quasi-particle mixers. Below a certain voltage V_{db} (called the drop-back voltage), there are no stable dc bias points, and the junction switches to the zero voltage state. The other thing is that the Josephson oscillations can be used for heterodyne mixing. This Josephson mixing can interfere with quasi-particle mixing and cause increased mixer noise. These two phenomena are described below.

The drop-back voltage is caused by Josephson oscillations. At a certain bias voltage, the voltage amplitude of the Josephson oscillations becomes equal to the bias voltage. At this point, the junction will switch to the zero voltage state, since it is a lower energy state than the finite voltage state. At higher voltages, the oscillation frequency is high, and the supercurrent is shunted out by the capacitance. If the local oscillator causes the bias to enter this unstable drop-back region, the mixer will be very noisy. This has been studied in [39].

The Josephson effect can also be used to detect radiation. When an RF signal is applied to a Josephson junction, steps appear in the I-V characteristic, at voltages $n\hbar\omega/2e$ [40].The heights of the steps are a function of the RF power. This can be used for direct detection and mixing, the same way as the quasi-particle tunneling. At high frequencies these steps can interfere with quasi-particle mixing. This will increase the noise level of the quasi-particle mixer.

To reduce the problems associated with the drop-back voltage and Josephson mixing, a magnetic field can be applied to suppress the Josephson tunneling so that quasi-particle tunneling dominates. To describe the effect of magnetic fields on Josephson tunneling, we first need to introduce two things: The Josephson penetraion depth, and the effect of magnetic fields on the macroscopic phase ϕ.

The Josephson penetration depth gives a measure of the length within which dc Josephson currents are confined near the edges of the junction and is defined as:

$$\lambda_J = \left(\frac{\hbar}{2\mu_0 e J_c d}\right)^{1/2} \tag{2.17}$$

where $d = t + \lambda_1 + \lambda_2$, and λ_1 and λ_2 are the penetration depths for the two superconducting electrodes [11],and J_c is the junction critical current density defined in equation (2.16). It can be observed that changes in the barrier thickness t strongly affect λ_J since J_c depends on t exponentially ($R_n A$ depends on t exponentially). For our SIS junctions which have an area of $A = 1\mu m^2$ and thickness of $t = 1nm$, for Nb/AlOx/Nb junctions $\lambda_J^{AlOx} \approx 7.5\mu m$ and for Nb/AlN/Nb junctions $\lambda_J^{AlN} \approx 3.7\mu m$. It turns out that they are 'small' in terms of the Josephson penetration depth λ_J. The conclusion is that if the junction dimensions are smaller than λ_J, current is uniformly distributed inside the junction and life becomes easier.

We need one more equation to be able to describe the effect of magnetic fields on Josephson junctions. Applying a magnetic field causes a modulation of the macroscopic phase ϕ described by:

$$\nabla_{x,y}\phi = \frac{2ed}{\hbar}\mathbf{B} \times \hat{\mathbf{z}} \tag{2.18}$$

Now we can look at the effect of a magnetic field on the Josephson current. The junctions are square shaped. We will consider two orientations of the magnetic field. In the first case the magnetic filed is perpendicular to one of the sides of the junction and parallel to the barrier. This we will call the ***square shaped*** junction orientation. In the other case, the field is 45 degrees rotated and is perpendicular to the diagonal of the junction and parallel to the barrier. This we will call the ***diamond shaped*** junction orientation. The effect of the shape of the junctions and orientation of magnetic field, has been studied in [49, 50]. A relationship between the maximum dc Josephson current ($I_{c,max}$) and the applied field can be calculated for each case. This will be done below.

[11] For 'clean' Nb at zero Kelvin, $\lambda_0 = 38nm$ [37].

In each case we solve for equation (2.18) for $\phi(x,y)$ as a function of applied field. Then we substitute $\phi(x,y)$ in equation (2.14) to get the current density distribution as a function of applied field. Then by integrating over the junction area, and taking the maximum, we can calculate the maximum total dc supercurrent current as a function of applied field:

$$I_c = \int\int dxdyJ_c sin[\phi(x,y)] \tag{2.19}$$

The result for the 'square shaped' and 'diamond shaped' junction is:

$$\frac{I_{c,max}}{I_{c,max}(\phi=0)} = \begin{cases} \left|\dfrac{sin\pi(\phi/\Phi_0)}{\pi(\phi/\Phi_0)}\right| & \text{SquareShaped} \\ 2\left|\dfrac{1-cos(\pi(\phi/\Phi_0))}{(\pi(\phi/\Phi_0))^2}\right| & \text{DiamondShaped} \end{cases} \tag{2.20}$$

where $\Phi_0 = h/2e = 2.07 \times 10^{-15}$ weber is the flux quantum , $\phi = BLd$ is the magnetic flux through the junction, L is the junction side length, and B is the applied magnetic field. In figure 2.10(a) we can see the calculated normalized maximum dc Josephson current as a function of normalized flux for different angles of the applied magnetic field [12]. The two extreme cases are indicated.

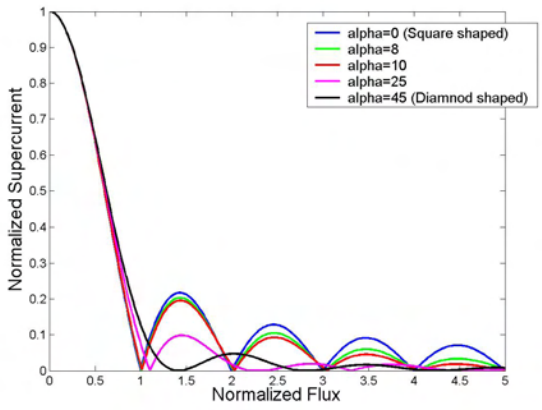

(a) Calculated normalized Josephson Supercurrent $I_{c,max}$ (normalized to $I_c(0)$) as a function of normalized flux ϕ (normalized to $\Phi_0 = h/2e$) in an SIS junction for different orientations of the applied magnetic field. For an angle of alpha=45 degrees, the sensitivity of the current to the field is minimum.

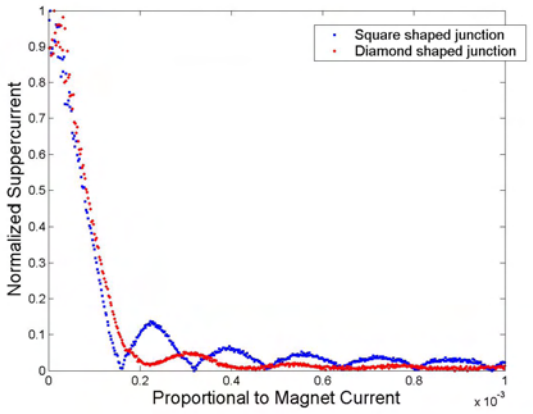

(b) Measurement results for an $8\mu m^2$ AlOx SIS junction. The vertical axis is the dc Josephson supercurrent normalized to it's maximum value. The horizontal axis is proportional to the current passed through the magnet coil. The figure shows the results for the two square and diamond shaped junctions.

Figure 2.10: Fraunhoffer patterns (calculated and measured) in the dc Josephson current.

Two things can be understood from this picture. We see that by applying a magnetic field, the Josephson supercurrent is suppressed. Usually the first or second minimum is chosen for

[12]These patterns are also called 'Fraunhoffer' patterns, due to their mathematical similarity to optical diffraction patterns

this purpose, since the required current in the coil magnets generating the magnetic field will be small. We see that the sensitivity of the current - at the minimum points - to the field is much less when the angle approaches 45 degrees, and a broad minimum is created. This is an important improvement, since SIS junctions are not exactly similar, and therefore one specific bias current through the magnet coil, will not bring the curve to the minimum for all SIS junctions. In the ALMA project, there will be 64 telescopes operating at the same time. Some of the mixers will be made out of two SIS junctions (For example sideband separating mixers). A slight difference in I_c of the SIS junctions, produces mismatch between the properties of the junctions which causes a degradation in the efficiency of the mixer. The specific advantage for a diamond shape junction is the broad minimum in the DC Josephson current versus magnetic field, which makes the pair not sensitive to the small differences of the SIS junctions. The effect of the magnetic field orientation on the dc Josephson current has been measured for an $8\mu m^2$ AlOx junction for the two different field orientations, and is presented in figure 2.10(b). The effect is clearly visible.

Real SIS tunnel junctions have many properties that will limit mixer performance. These limitations can be put into four general categories: smearing of the I-V characteristics, high-frequency roll-off caused by the junction capacitance, the high-frequency limit imposed by the superconducting energy gap, and problems caused by the Josephson effect. All of these properties depend on the material properties of the superconductor and the barrier. This will be discussed next.

2.4 Material Choice for SIS Mixers

There is a large range of materials that can be used for SIS mixers. We will first summarize the desired properties for an SIS tunnel junction used as a submillimeter mixer.
The junction capacitance should be small; therefore barriers of low dielectric constant and low barrier height, and submicron low R_nA product junctions are needed. The energy gap of the superconductor should be large to avoid losses in the superconductor and the effects of the drop-back voltage. The transition temperature should be as large as possible to be able to cool down the junctions and surrounding circuits efficiently. The junctions should survive thermal cycling and long periods of storage. Finally, the I-V characteristics need to be sharp enough to reach quantum limited mixing, but they don't need to be as sharp as they would be at lower frequencies. Basically no single material satisfies all these needs, and trade-offs need to be made.
Materials that can be used as SIS junctions for mixers include Lead(Pb)/native-oxide or Lead-alloy/native-oxide (Pb/Oxide/Pb), Niobium/native-oxide/Lead (Nb/Oxide/Pb), NbN/MgO/NbN, Nb/Al-AlOx/Nb, NbN/AlN/NbN, and NbTiN/AlN/NbTiN. The latter has not been used to date, and still has to be developed. A fair comparison between all these materials is out of the scope of this thesis. We will only compare the two types that are used in this work.

Nb/Al-AlOx/Nb SIS junctions have generally good I-V characteristics. They were first developed in 1983 by Gurvitch *et al.* [44]. The combination of the three layers called the trilayer, is made in a single vacuum sputter deposition. The barrier is formed by depositing an Al layer

and thermally oxidizing the layer. The remaining un-oxidized Al parts, will become superconductive due to the superconducting proximity effect [13]. The resulting Al_2O_3 barrier has much better properties than native Nb oxide, because there is only one stable oxide [14], and the relative dielectric constant is lower ($\epsilon_r \approx 10$). The junction area and the surrounding circuitry are defined after the trilayer is completed. In the fabrication chapter, the fabrication process is given in detail.
Nb/Al-AlOx/Nb junctions have several advantages. The I-V characteristics are extremely sharp. The sub-gap leakage of these junctions is very low, and the gap width is small. Their thermal stability is very good and they can be stored at room temperature without degradation of the I-V characteristic. Their repeatability is also high. They are a bit difficult to create in submicron dimensions and their specific capacity is somewhat higher compared to Pb technology. The gap voltage of these junctions is only 2.8 meV, so the Nb will be lossy above 700 GHz. Yet, they are the most used technology for submillimeter astronomy SIS mixing.

Nb/Al-AlN/Nb SIS junctions have recently become very attractive. The reason is mainly their low barrier height compared to AlOx barriers, which gives them the possibility to have smaller RC time constants, and therefore wider RF bandwidths in mixers. Mixer designers prefer R_n to remain constant for matching purposes. Therefore if the barrier height (ϕ) in equation (2.13) reduces, and the thickness is kept constant, the area has to be reduced to have R_n unchanged. Nevertheless, the RC product decreases as a result of this. The thickness cannot be reduced easily, since pin-holes will appear in the barrier, and the quality will degrade. Reducing the area is also not easy, and is still a point of concern. This technology is still under development, but is very promising and already reasonably good results have been achieved [42, 43].

2.5 Coupling of Radiation to the SIS Junction

A typical SIS junction size is $\sim 1\mu m$. Because this is so much smaller than the wavelength being received, an antenna and associated coupling circuitry are needed to bring the radiation to the junction without loosing power. Additionally, since the input impedance of the SIS junction is very different than that of the free space impedance (377Ω), a large amount of the signal will be back-reflected and not absorbed by the junction. This also has to be corrected for by matching the impedances through the coupling circuit.
There are two major ways to couple the optical beam into the SIS junction: waveguide coupling and quasi-optical coupling. Moreover, extra tuning circuits are needed to compensate for the SIS junction capacitance. These will be discussed now.

[13] When a superconductor is placed in contact with a 'normal' non-superconductor, Cooper pairs can diffuse into the normal metal, extending the superconducting properties to some length scale. This is called the "Superconducting Proximity Effect" [33].

[14] There are several stable oxides of Nb. The different oxides are a low T_c superconductor, a semiconductor, and an insulator. All of these will be present during Nb oxidation, making the superconductor-barrier interface poor. Additionally, the insulating phase (Nb_2O_5) has a dielectric constant of 30, which is very high.

2.5.1 Waveguide Coupling

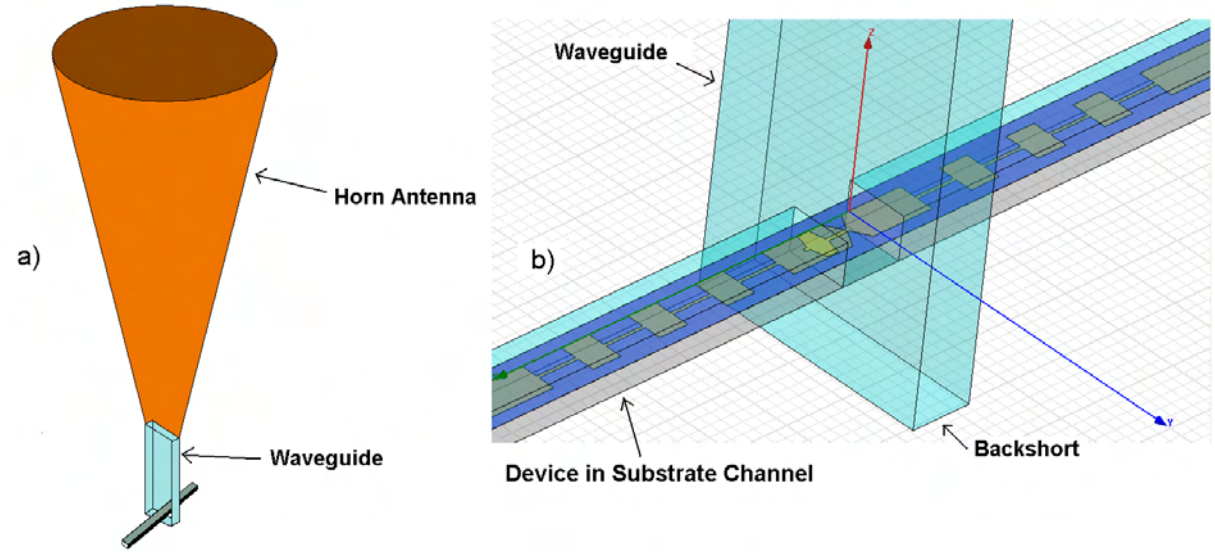

Figure 2.11: Geometry of a waveguide mixer. Radiation is coupled into the waveguide via a horn antenna. The device sits in a substrate channel that crosses the waveguide. The backshort cavity behind the device is used to tune the electromagnetic environment in the waveguide and around the device.

The coupling technique used in this work is waveguide coupling, which is the more traditional microwave engineering approach. In a typical waveguide coupled mixer, the input optical beam is collected by a horn antenna, which itself is coupled to a single-mode rectangular waveguide (figure 2.11(a)). The SIS chip is mounted in a very narrow channel (called the substrate channel) which crosses the waveguide (figure 2.11(b)). This requires very precise mechanical positioning as well as polishing the chip substrate to very thin dimensions (40μm for our case). An on-chip planar transition or 'probe' picks up the incident radiation from the waveguide, and passes it on to an on-chip thin-film transmission line which couples the radiation to the SIS junction where the signal and LO are mixed (figure 2.12(a)).
The metallization on the chip and the waveguide walls form a transmission line, which carry the generated IF signal in the junction, to the ends of the chip where contact is made with the receiver's IF system. The on-chip metallization line is patterned with a periodic series of high- and low-impedance sections, which form a low-pass filter that prevent the RF radiation to leak into the substrate channel and interfere with the generated IF signal. This is called the RF choke filter. This same IF line is used to supply the DC bias to the SIS junction (figure 2.12(a)).

The geometry of a waveguide mixer chip incorporating a microstrip transmission line is shown in figure 2.12(c). The two conductors of the RF tuning circuit (the ground plane and the wiring layer) are superconducting or metallic films, and they are seperated by a dielectric layer. All three layers are in the order of 100's of nm thick. The tuning circuit incorporated 3

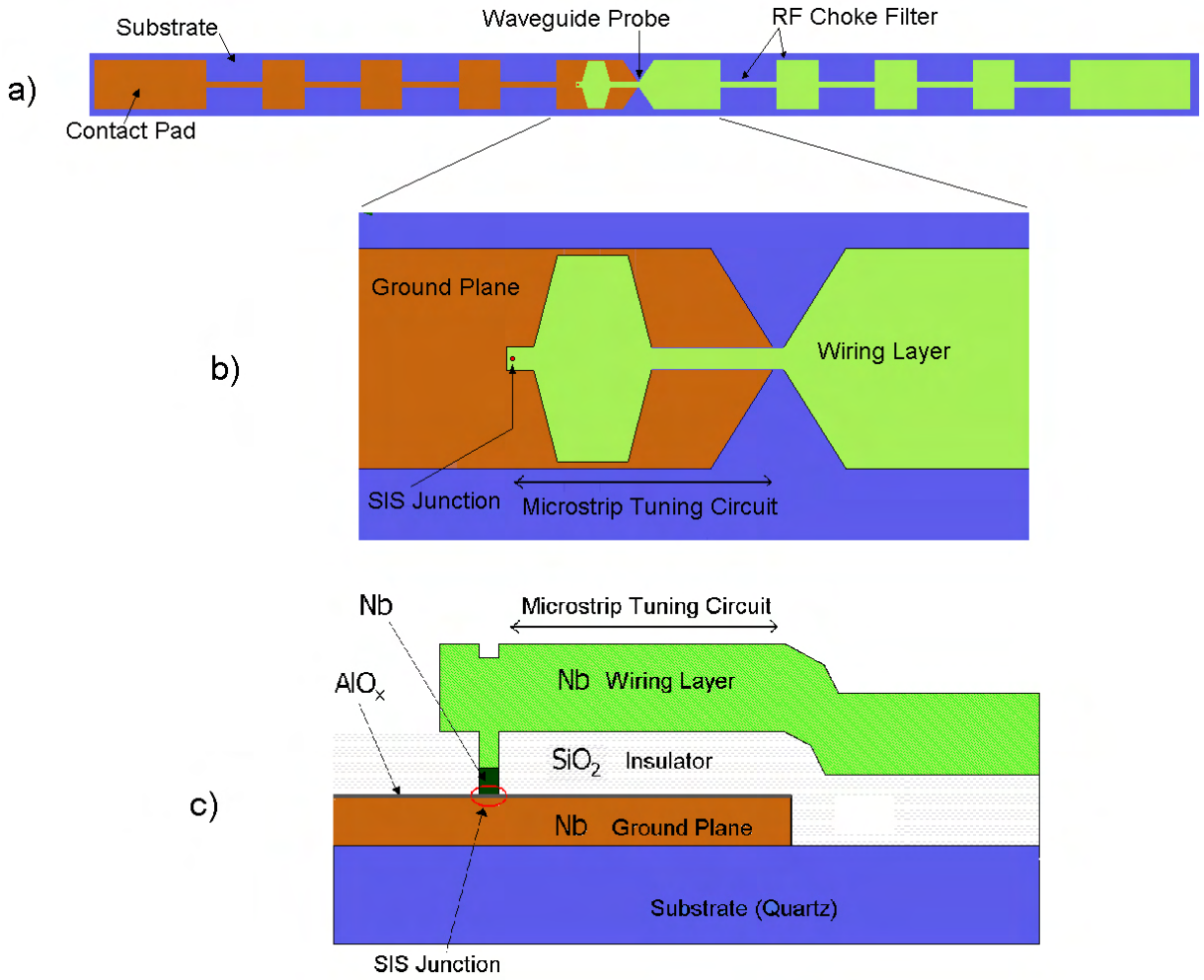

Figure 2.12: The on-chip geometry of a waveguide SIS device. (b) shows a zoom in of the central portion of the device shown in (a), showing the waveguide probe, on-chip tuning circuit, and SIS junction. (c) is a cross section of (b), showing the material used for the different layers.

sections of microstrip that are 3-40 μm long and 1-60 μm wide. The SIS junction(s) are embedded between the ground plane and the wiring layer. Ideally, the impedance seen from the probe point into the waveguide, should be matched with the impedance seen from the probe point into the thin-film transmission lines. This means that the probe and the transmission lines can be used to achieve the proper matching condition.

The design hierarchy for achieving proper matching is described now. First, the horn antenna, the waveguide dimensions, and the depth of the waveguide cavity behind the SIS chip (the backshort), are designed assuming that the impedance seen into the probe and on-chip transmission lines is approximately 50Ω. The combination of the horn, waveguide and the backshort (called the waveguide block) impose a certain bandwidth limitation to the RF signal. The backshort can

be used to adjust this bandwidth to some extent. In high reliability mechanical systems, it is preferred to have a fixed position for the backshort making it non-tunable (which is the case for this work). Now assuming that we have a 50Ω impedance looking into the waveguide, the probe can be designed. Again, for the probe design, we assume that the impedance seen looking into the on-chip transmission lines, is 50Ω. Note that the probe also imposes a bandwidth limitation. After all this, a series of on-chip transmission-line impedance transformers can be used to match the SIS junction impedance to the probe.

However, due to the parallel-plate structure in SIS junctions with the two electrodes separated by only $\sim 1nm$ of insulation, the capacitance of SIS junctions is very large. Typical values for the junction specific capacitance are in the range $60 - 100fF/\mu m^2$, depending on the materials used, current density, etc. Thus, for a typical $1\mu m^2$ junction, $1/\omega C \sim 3 - 4\Omega$ at 600 GHz - quite far from the typical 50Ω impedance levels for RF circuits. As a consequence, an inductive on-chip transmission-line should be added to compensate for the junction capacitance (and not just impedance transformers). The tuning inductor may be either a parallel [52, 53] or series [54] element, or be placed in between two SIS junctions [55]. Typically, the tuning inductance is a short section of thin-film superconducting microstrip line. For all of these cases, the RF bandwidth of the mixer is fundamentally limited by the RC product of the SIS junctions [56], to about 100 GHz for Nb/AlOx/Nb junctions and increasing to 300 GHz for devices with AlN barriers [57]. Detailed analysis of the microstripline design is given in the modeling chapter.

In conclusion, waveguide systems are widely used for detection in the submillimeter regime, because of their well proven behavior , excellent beam quality and bandwidths. However, their fabrication is very elaborate and becomes more and more difficult as their operation frequency increases, since their dimensions decrease.

2.5.2 Quasi-optical Coupling

The other major approach is quasi-optical coupling, in which case one omits the intermediate step of collecting the radiation into a waveguide, and instead uses a thin-film lithographed antenna on the SIS chip itself. An additional focusing element is needed in front of such an antenna because of the nonideal beam pattern. For this purpose, a silicon lens is used which is glued to the mixer chip. Experimental and theoretical work show that a 90% coupling efficiency may be achieved using optimized antennas and lenses [51]. Planar antenna calculations are typically carried out using method of moment techniques, and the effect of the lens is evaluated using ray-tracing and diffraction calculations, sometimes including multiple internal reflections. The same problem with tuning out the capacitance of the SIS junction exists here, and the same techniques are used for this purpose as explained in the waveguide coupling subsection. Figure 2.13 shows a sample quasi-optical mixer chip layout incorporating a twin-slot antenna and a two-junction tuning circuit.

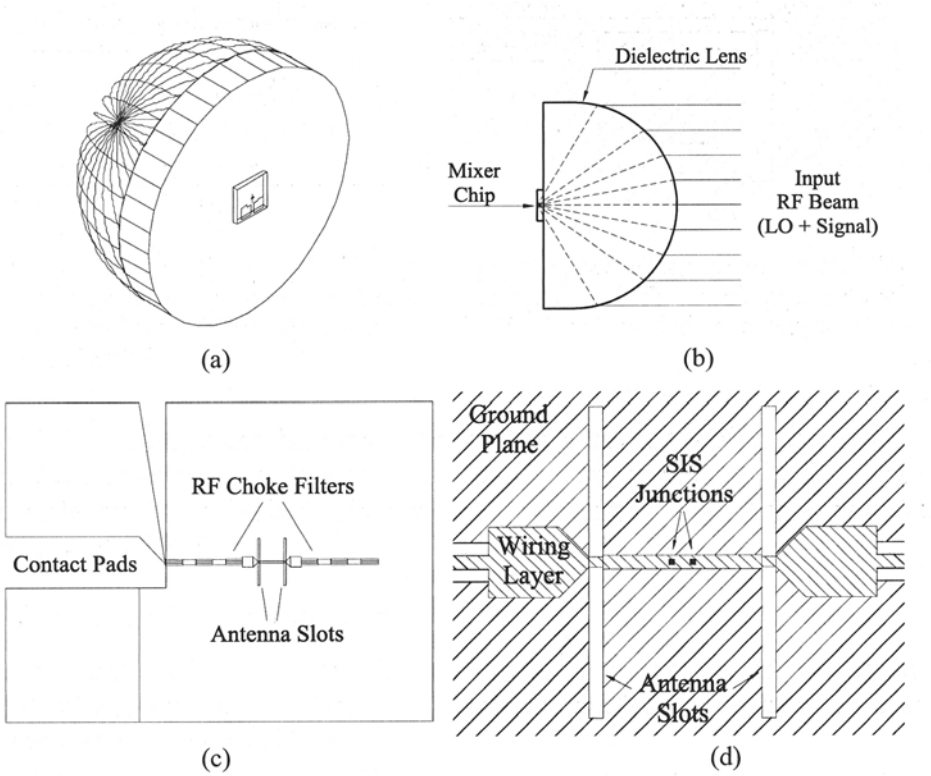

Figure 2.13: (a) and (b) Geometry of a typical quasi-optical mixer, showing the SIS device chip mounted on the back of a dielectric silicon lens. (c) and (d) Sample quasi-optical mixer chip layout incorporating a twin-slot antenna coupled to a two-junction tuning circuit [58].

Chapter 3
SIS Device Fabrication

3.1 Layer Production

For creating the different layers in an SIS mixer chip shown in figure 2.12, different processes are used. The different layers and the processes used to create them are discussed in the next sections. First an overview of the deposition of individual superconducting, metallic, and dielectric layers for fabrication of Nb/AlOx/Nb SIS junctions is given, and then the methods that are used to pattern these layers are discussed. After that, a detailed review of the fabrication process, in a flow chart manner is provided.

3.1.1 Layer Deposition

There are four main layers involved in the fabrication of Nb/AlOx/Nb or Nb/AlN/Nb SIS devices in this thesis. These are either superconducting (Nb), metallic (Al) [1], or insulating (AlOx, SiO_2). Nb and Al are made using standard DC magnetron sputtering and are based upon a long history of use in the group [59]. SiO_2 is made by RF magnetron sputtering. AlOx is made by oxidation of the Al layer.

3.1.2 SIS Trilayer Production

The trilayer is the most critical fabrication step in SIS devices that determines important mixer properties. The properties of an I-V characteristic are almost completely dependant on this multi-layer. It is a combination of 3 main layers that are created in one process step. Their fabrication of Nb/AlOx/Nb trilayer goes briefly as follows:

- Deposition of a 100nm thick Nb layer by sputter deposition. This is the bottom (base) electrode of the SIS junction.

[1] The superconducting transition temperature for Al is 1.2 K. However, at liquid helium temperature of 4.2 K, the Al layer which is in contact with the Nb layer becomes superconducting due to the proximity effect between Nb and Al [33].

- Deposition of a thin Al layer, approximately 7-10 nm thick.
- In-situ low pressure oxidation with pure oxygen at room temperature of the Al. This oxide layer is approximately 1 nm thick and determines the normal-state resistivity and specific capacitance of the SIS junction.
- Deposition of a 100nm thick Nb layer by sputter deposition. This is the top (counter) electrode in the junction.

This specific technique for creating the trilayer has resulted in the success of SIS mixers during many years because of its unique specialities. These can be summarized as follows:
The Al layer which is sputtered on Nb, has the property that it can get superconducting due to its proximity to Nb, even though its superconducting transition temperature (1.2 K) is below liquid helium temperature (4.2 K). This is called the proximity effect, and is caused by the fact that the coherence length for Cooper pairs in Nb is larger than the thickness of the Al layer, allowing Cooper pairs to pass the Al without loosing their superconducting properties. Moreover, Al has a very uniform and good quality (free of pinholes) intrinsic oxide (Al_2O_3) which results in controllability of oxidation, allowing repeatability in the R_nA product and low leakage currents that determines the behavior of I-V characteristics. Al_2O_3 layers as thin as a few angstroms (1-2 monolayers) can be created. By changing the oxidation time and pressure, R_nA can be changed to $R_nA \sim 10 - 40\Omega\mu m^2$.

3.2 Pattern Definition

For patterning the different layers, two main processes are used: Plasma etching and lift-off. These will be described in this section. In the case of lift-off, the resist layer is either patterned with optical lithography (Ground plane definition) or with electron-beam lithography (Junction definition). In the case of plasma etching, the resist layer is patterned with e-beam lithography.

3.2.1 Plasma Etching

The plasma etching process used in this work is a reactive-ion etching (RIE) process. An O_2/SF_6 plasma is generated, the fluorine-based gas (SF_6) which is the reactive agent, chemically reacts with Nb. This will produce anisotropic etching. RIE is used to pattern the critical structures in an SIS mixer (*i.e.* the junction and the wiring layer). The resulting pattern is a positive image of the original resist pattern (figure 3.1(a)).
The resist pattern needs to be as vertical as possible (no undercut) to get the best etching result. For cleaning organic residues like photo-resist remnants, an O_2 plasma is used to sputter etch the surface. An Argon plasma sputter etch is used to remove the native oxide from the Nb surface prior to deposition of a second material.

3.2.2 Lift-Off

In a lift-off process, a resist layer is first patterned. Then a layer of some material is deposited. When the resist pattern is dissolved, the parts where the material is deposited on top of the resist will also be removed, leaving behind a negative pattern of the resist by the deposited material. In this case, undercut in the resist layer is required to have smooth edges of the deposited layer after lift-off. Lift-Off is used to pattern the trilayer and the SiO2 insulating layer (using the same resist layer used for patterning the junctions - a "self-aligned" lift-off" process). A schematic diagram of a typical lift-off process is shown in figure 3.1(b).

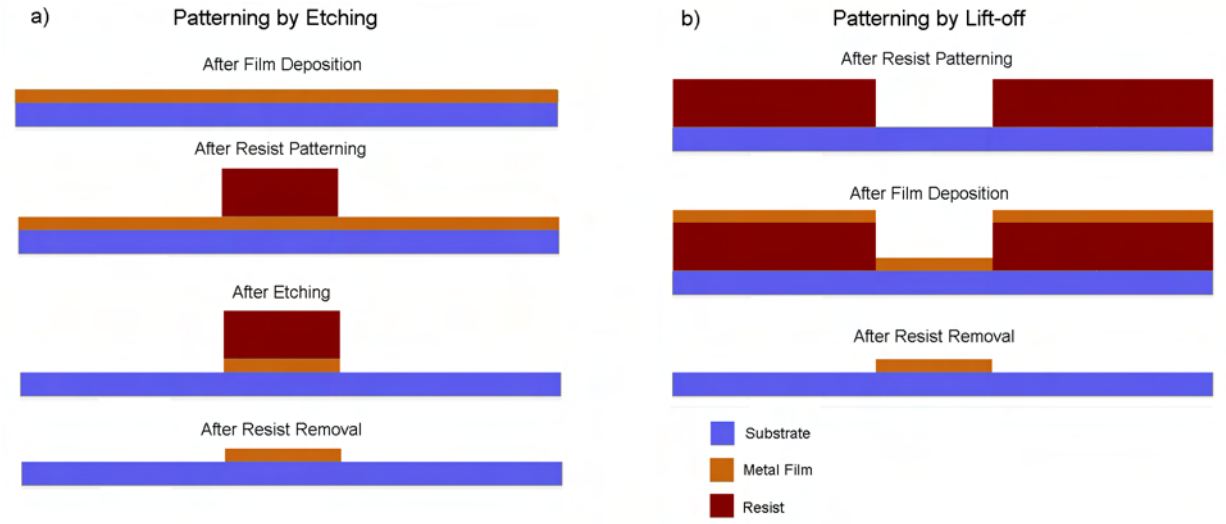

Figure 3.1: Pattern definition by etching (a) and lift-off (b). In etching the layer is deposited, a resist pattern is defined, and the pattern is transferred to the layer by etching the exposed material. In lift-off patterning, a resist pattern is defined before depositing the layer. Dissolving the resist leaves behind a pattern that is the reverse image of the resist pattern.

3.3 Fabrication Flow Chart

In this section a step by step description of important process steps for fabricating a Nb/AlOx/Nb SIS mixer device is given.
The devices are made on a thin ($200\mu m$) quartz wafer, which should be delicately handled. The wafer is first cleaned and ultra-sonicated in acetone for 10 minutes. The fabrication flow chart shown in figure 3.2 will now be explained in detail.

Nb monitor layer deposition

In this step, 100 nm of Nb is deposited on the quartz wafer by sputtering in a Nordiko-2000 sputtering system. The process time is 75 sec for 100 nm. This monitor layer will later become

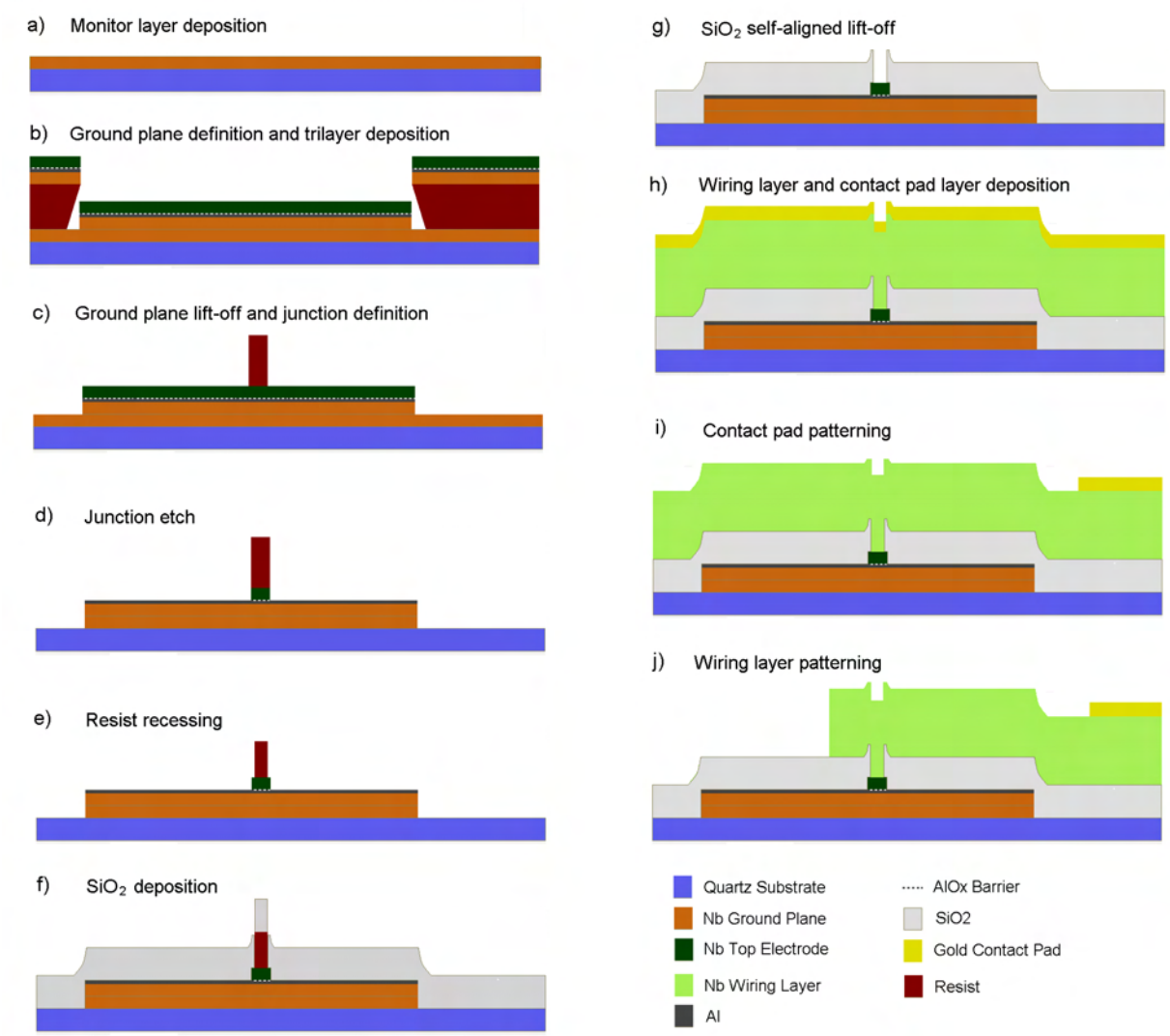

Figure 3.2: Fabrication flow chart for Nb/AlOx/Nb SIS devices.

part of the ground plane together with the trilayer's bottom electrode, and is used to monitor the top electrode etching process later during the top electrode etch.

Ground plane definition and trilayer deposition

In this step, first a pattern is created for the ground plane by using optical lithography and photoresist AZ5214E. No alignment is needed at this stage. The resist is baked after spinning and post-exposure baked after UV exposure through the ground plane mask. The resist is then developed in developer MF-321. The amount of development depends on how much undercut in the resist is required. This determines whether the later deposited trilayer will create smooth ground-plane edges or not. If insufficient undercut is created, the deposited trilayer will create

sharp ground-plane edges, which could lead to short circuits. Therefore, the developed resist should be checked under the optical microscope for sufficient undercut.

The next step is to deposit the trilyer of Nb/Al-AlOx/Nb. This trilayer is very crucial for the SIS mixer and therefore is created in one process step. The wafer is put into the Nordiko-2000 sputtering system and is RF Argon-plasma cleaned. Then a pre-sputtering of Nb is performed (with the shutter closed) to reach a steady-state deposition rate. The actual Nb deposition follows next and 100 nm of Nb is deposited. Next, in the same manner, 7-10 nm of Al is deposited. Afterwards, the wafer is exposed to low-pressure ($\sim 3 \times 10^{-3}$ Torr) room-temperature oxidation inside the load-lock chamber for ~ 16 minutes. This results in a ~ 1 nm thick Al_2O_3 barrier. A second 100 nm Nb layer is then sputtered again to complete the trilayer. The summary of this step is shown in figure 3.2(b).

Ground plane lift-off and junction definition

In this step, the pattern in the resist is transferred to the sputtered trilayer when lift-off in hot acetone and sonication is done.
Then the junction resist pattern is created by electron-beam lithography in a Leica e-beam system. This allows for a very accurate definition of the small square $1\mu m^2$ junctions, and sharp square edges. As a result, the junction area is determined accurately (compared to older optical lithography techniques), which allows for accurate junction capacitance definition [2]. The e-beam writing time, depends heavily on the writing resolution, and for this work is approximately 45 minutes. This step is shown in figure 3.2(c).

Junction etch (Nb top electrode etch)

After defining the junction pattern, the wafer is subjected to a SF_6/O_2 plasma. This RIE process, etches the 100 nm Nb top electrode. Here the monitor layer is used to monitor the etching process, since it's thickness is the same as the top electrode. A laser beam is shone on the monitor layer during the etching process, and the combination of the reflected and incident beam produces a periodic change in the intensity of the detected beam. When the monitor layer is completely etched, a sudden change occurs in the detected beam, which indicates the end of the process. Care should be taken, since the thickness of the resist reduces ~ 100nm during this etching, which should be taken into account. This step is shown in figure 3.2(d).

Resist recessing

Before continuing with the SiO_2 deposition, an intermediate step is performed. The width of the resist is reduced in order to prevent later short circuits that might occur during the SiO_2 lift-off

[2]Since small junctions have a degree of area inaccuracy ($\pm 20\%$), their capacitance changes $\pm 20\%$. To measure their capacitance, larger $25\mu m^2$ junctions are created on the wafer of which R_n is measured later during dc testing. Then the area of the small junctions is deduced by dividing the normal-state resistance - area product (R_nA) calculated from big junctions, by the measured R_n of small junctions.

process. This will be explained further in the SiO_2 lift-off step. The recessing is done in an O_2 plasma for ~ 10 minutes, after a preconditioning for 20 minutes. However, during this process, the thickness of the resist also reduces again by an amount of $\sim 500 - 600$ nm, which should be taken into account. Since this etching is quite isotropic, the reduction rate in thickness is the same amount in the width. This step is shown in figure 3.2(e).

SiO_2 deposition

This process is done in an RF SiO_2 sputtering system. 250 nm of SiO_2 is sputtered in ~ 16 minutes time. The resist layer at this stage should be thick enough ($\geq 250nm$) in order for the next lift-off process to be easier. Otherwise, the resist layer will be completely covered by SiO_2 and acetone will not be able to penetrate inside the 'junction hole' to solve the resist. This step is shown in figure 3.2(f).

SiO_2 self-aligned lift-off

The wafer is put in acetone for approximately one day, so that the acetone can penetrate in the small junction holes. The lift-off process usually needs extra treatment, since the junction holes are very small. Therefore, the wafer is first put in hot acetone and ultra-sonicated for 10 minutes. Then the surface is brushed very delicately with a soft cloth to assist the lift-off. Care should be taken not to overdo this, since there exists the risk that the SiO_2 is removed from around the junctions, and short circuits might occur during the wiring layer deposition. The recessing reduces this risk. This step is shown in figure 3.2(g).

Wiring layer and contact pad layer deposition

During this step, 500 nm of Nb and then 50 nm of Gold is deposited on the wafer with the Norkio system. Before this deposition step, an Ar sputter cleaning is performed to remove the remaining resist. However, this could cause in the removal of the AlOx layer in the exposed area around the junction caused during the lift-off of SiO2. This could lead to short circuits between the ground and wiring layers. The Nb deposition is done in 2 steps with a time in between to prevent overheating. Oil is put under the wafer to increase the heat contact between the wafer and the chuck. This step is shown in figure 3.2(h).

Contact pad and wiring layer patterning

First a resist layer on top of the gold layer is patterned with optical lithography. Then a wet etching process is applied to etch the gold, creating the contact pad pattern. Afterwards, an e-beam lithography step is used to pattern the Nb wiring layer. The alignment during this step is crucial in reducing the error in the microstrip tuning circuit patterning. Then, the same RIE technique used for the junction etching, is used to etch the wiring layer. This step is shown in figure 3.2(i) and (j).

3.3.1 Final layout

Picture 3.3(a) shows the final layout of the 4 different masks used for the groundplane, junction definition, wiring layer definition, and contact pads. The groundplane and contact pad layer masks are optical lithography masks. The junction layer and wiring layer masks are e-beam masks. There are 8 sectors on every batch, each of them having 88 devices 7 of which are test devices. The surroundings of the masks as well as the area between the 8 sectors, is used for making test structures. These structures give information about the material parameters of different layers (resistivity, superconducting gap voltage, ...), as well as the quality of the fabrication processes (undercut, alignment, ...). Figure 3.3(b) shows a scanning electron microscope (SEM) picture of the final devices.

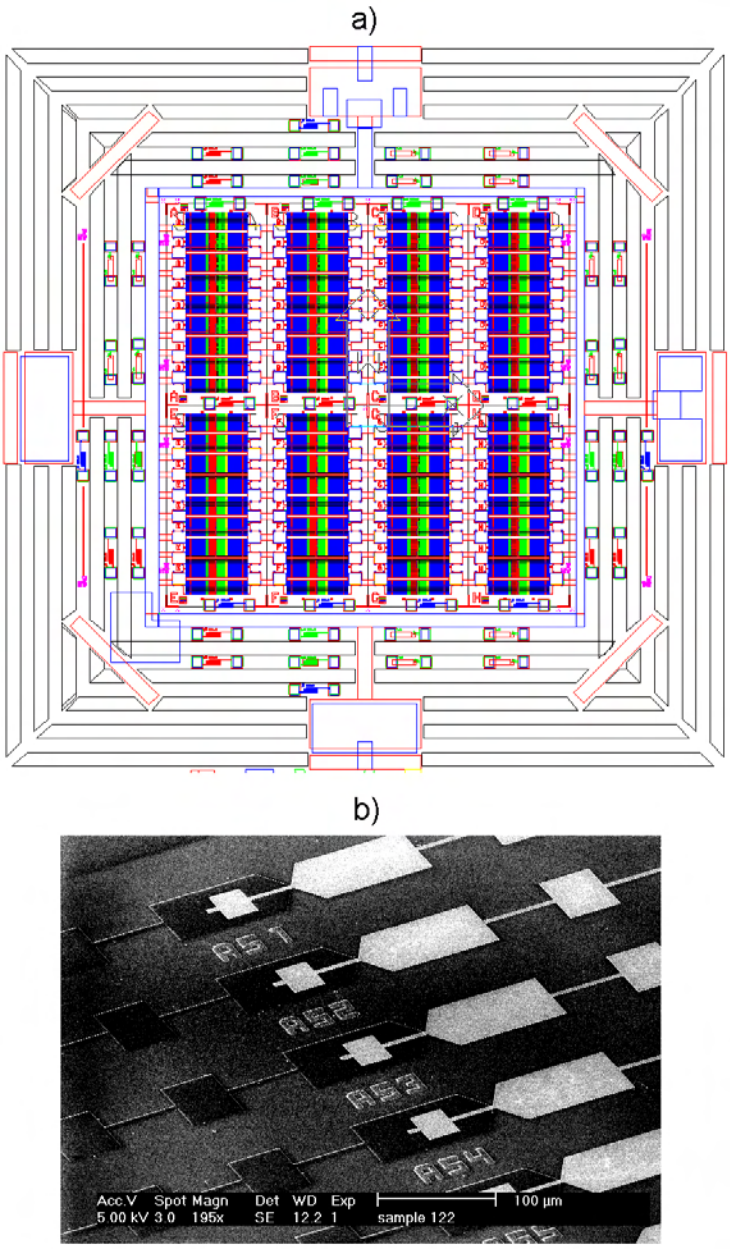

Figure 3.3: (a) Final layout of the 4 optical and e-beam masks. There are 8 sectors on every batch, each having 88 devices. Test structures can be seen around the 8 sectors. (b) SEM picture of the final devices.

Chapter 4
Modeling of SIS Mixers with Integrated Tuning Circuits

As was already mentioned in section 2.5, integrated tuning circuits need to be utilized in order to couple the radiation efficiently to the SIS junction. The integrated tuning circuits are usually made out of microstrip lines (as in this work) and will act as inductors to resonate out the junction capacitance or serve as impedance transformers to match the junction impedance to the driving antenna.
In this work, Nb/AlOx/Nb SIS junctions are integrated with Nb used as the material for the tuning microstrip lines. Below the Nb superconducting gap frequency (~ 680 GHz), the Nb has negligible RF loss as a superconductor. However, above the gap frequency, Nb behaves like a normal metal since the RF photons have enough energy to break the Cooper pairs. A large fraction of the radiation is thus lost in the tuning circuits. Therefore, mixers that are to be operated much above 680 GHz, will not be efficient anymore if Nb is used. A way to overcome this problem is to use other material like Al which has lower loss as a normal metal above the Nb gap frequency, or to use NbTiN which is a superconductor with a higher gap frequency.

However, in this work it was decided to use Nb, since first of all the frequency range (600-720 GHz) is not much higher than the Nb gap frequency, still allowing for some tuning above the gap. Secondly, the technology for integrating Nb/AlOx/Nb junctions with other microstripline materials like Al or NbTiN at that time was much more complicated than the well-known and easy-to-fabricate Nb microstriplines. Switching to another junction type like Nb/AlN/Nb was also a choice, but again technologically too complicated and risky to realize at that time.
Our work on Nb/AlOx/Nb with Nb tuning circuits has obtained very good results, however with a lot of effort. Further ongoing work shows that using Nb/AlN/Nb junctions with Nb tuning circuits is much more promising than originally thought and will be the continuation of this work.

Understanding the characteristics of microstrip lines at high frequencies especially above the gap frequency of Nb is critical for the design of SIS mixers in this work. This chapter will describe the model that is used for characterizing Nb microstrip lines and also the methodology for their design. The fine tuning and optimization of these microstrip lines is the subject of the

next chapter.

4.1 Review of RF tuning circuits

SIS junction RF impedance

The geometrical capacitance of an SIS junction can be represented by a capacitance C_j which is connected in parallel with the quasi-particle tunneling impedance of the junction, $Z_j = R_j + jX_j$. In general Z_j must be calculated from complex expressions for the tunneling current which give both real and imaginary components due to the non-instantaneous behavior at high frequencies [26]. However it can be shown [60] that it is sufficient to approximate Z_j by the junction normal-state resistance R_n. The equivalent circuit for an SIS junction is shown in the dashed box in the circuit of figure 4.1. The nominal value for normal-state resistance R_n in our SIS devices is 25Ω. Small variation of R_n have only a minor effect on the simulations, and are not important. However, since the R_nA product is constant in one fabrication batch, variations in R_n translate into variations of junction capacitance C_j, which dramatically affects the bandwidth and center frequency, and should be taken into account.

There are many ways that we can use to tune out the capacitance of the SIS junction. These can be all put into two categories depending on whether a tuning inductance is placed in series or in parallel with the junction. These will be described now.

Parallel inductance tuning

The ideal tuning circuit for an SIS junction would simply consist of a lumped-element inductor L connected in parallel with the junction so that the admittances of the junction capacitance $j\omega C_j$ and tuning inductance $1/j\omega L$ would cancel at the resonant frequency $\omega_0 = 1/\sqrt{(LC_j)}$, leaving only R_n. The tuning inductance is most often realized as an electrically short section of a superconducting microstrip line. The bandwidth of the circuit is proportional to $1/R_nC_j$. Note that the R_nC_j product is independent of the junction area but which depends on the current density roughly as $1/J_c$. Thus high current density junctions are needed to obtain broad bandwidths.
In practice, shunt inductance tuning circuits must be modified by adding a so called "blocking capacitance" in series with the tuning inductance to allow a DC bias to be applied to the junction. This will add the difficulty that the RF impedance of this element must be kept small, to avoid reducing the bandwidth. This constraint proves to be difficult above 500 GHz [55].

Series inductance tuning

This method of tuning is shown in figure 4.1. A series inductance is used to cancel out the capacitance. This kind of tuning is used in this thesis work, and from now on, when referred to tuning, this kind of tuning is meant. This is the most common tuning circuit for SIS mixers, and does not have the difficulty with biasing as in the shunt tuning case. However, it presents some

difficulties, which will be briefly described here.

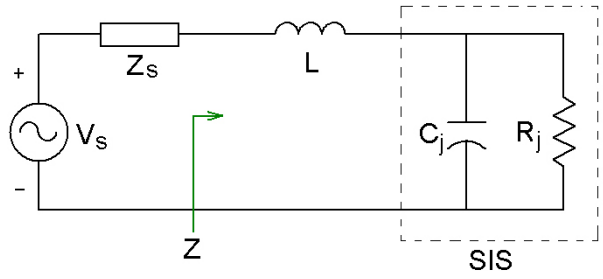

Figure 4.1: Equivalent circuit for an SIS mixer with series inductance tuning.

The difficulty presented by this circuit is that it also acts as an impedance transformer, producing a real impedance of the order $R_n/(R_nC_j\omega)^2$ which is very low compared to the 50 Ω impedance of the source. Therefore, a multisection microstrip quarter-wave transformer is then needed to bring the impedance back up to match the source (antenna). This transformer will reduce the bandwidth and introduce more losses, especially at higher frequencies for which a larger transformation factor will be needed. In addition, rapidly becomes difficult to design at higher frequencies. Because of the very low impedance needed, the last section of the transformer becomes quite wide, allowing higher order modes to propagate. In addition, a large discontinuity in width is developed between this section and the series tuning inductor. This means that the traditional analysis based on transmission-line formulas is inadequate to characterize the circuit, as are approximations which treat the discontinuities in terms of parasitic lumped elements as is common in microwave CAD (Computer Aided Design) programs. A more sophisticated method is needed which can calculate the two-dimensional distribution of current.

Let us calculate some of the parameters associated with the circuit in figure 4.1. The antenna is modeled as a voltage source with source impedance Z_s. The tuning circuit is simplified as a series inductance. As mentioned earlier, the junction resistance is almost equal to the junction's normal state resistance, $R_j = R_n$.
The RF coupling efficiency η is defined as the ratio of the absorbed power at the junction to the maximum available power at the source. For the circuit in figure 4.1,

$$\eta = 1 - \left| \frac{Z - Z_s^*}{Z + Z_s^*} \right|^2, \tag{4.1}$$

in which

$$Z = \frac{R_n}{1 + (R_nC_j\omega)^2} + j\frac{(L - R_n^2C_j)\omega + LR_n^2C_j^2\omega^3}{1 + (R_nC_j\omega)^2}. \tag{4.2}$$

and

$$\Gamma = \frac{Z - Z_s^*}{Z + Z_s^*} \tag{4.3}$$

is the reflection coefficient. Perfect coupling with $\eta = 1$ is achieved when the resonant condition is satisfied, *i.e.* $Z = Z_s^*$. However, in practice this condition is never completely satisfied, and the coupling efficiency will be lower than one. In fact, the Bode-Fano criterion [62, 63] states that there exists a theoretical limit on the minimum reflection coefficient magnitude ($|\Gamma|$) that can be achieved with an arbitrary matching network. This was further extended to typical SIS mixer circuits in [64]. This represents the optimum result that can be ideally achieved, even though such a result is always approximated in practice.

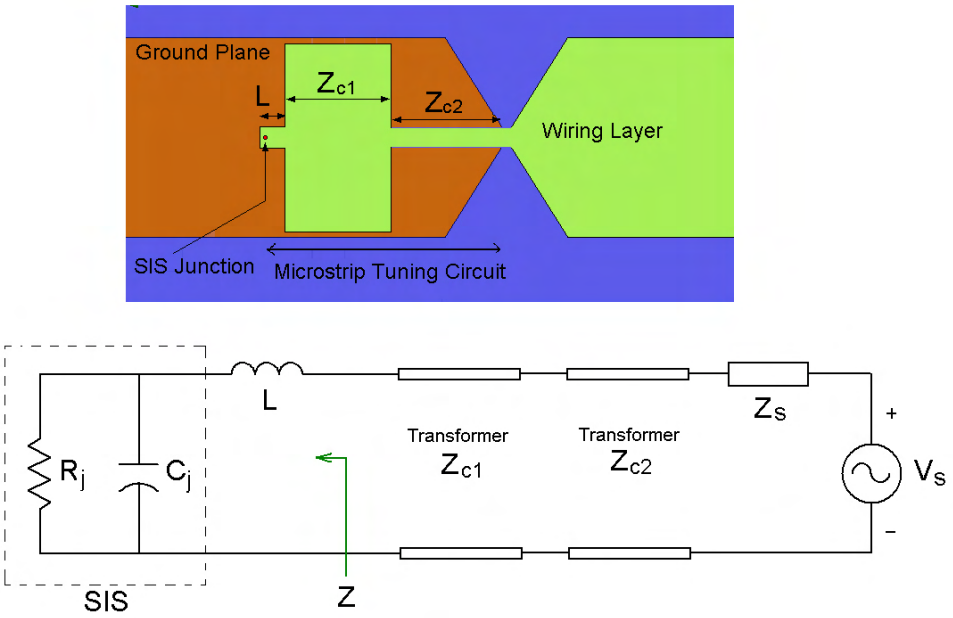

Figure 4.2: An SIS mixer with the associated microstrip tuning circuits. The small tuning inductor L, and the two quarter-wave transformers with characteristic impedances Z_{C1} and Z_{C2} are indicated.

Let's further evaluate the circuit in an ideal case where the source impedance is real. Typical values for our Nb/AlOx/Nb SIS junctions are: $R_n = 25\Omega$, $C_j = 80$fF. The center design frequency for ALMA band 9 (600-720 GHz) is $f_0 = 660$ GHz. In order to resonate out the capacitance at the center frequency, the imaginary part of Z, $Imag\{Z\}$, should be zero at $\omega_0 = 2\pi f_0$. We get

$$\omega_0 = \sqrt{\frac{1}{LC_j} - \frac{1}{(R_n C_j)^2}} \tag{4.4}$$

From this equation, the required value for the inductance that resonates out the capacitance at 660 GHz, is $L = 0.72$ pH . This inductance can be approximated by an electrically short section of a microstrip line which has a high characteristic impedance, therefore having also a small width.
However, the real part of Z in equation 4.2 is $Real\{Z\} = 0.36\Omega$ at this frequency, which is

much smaller than 50Ω . Therefore, extra transformers are needed that can convert this resistance to 50Ω at the source. The impedance conversion factor required is approximately 140. Two quarter-wave ($\lambda/4$) transformers can be used for this purpose, each having a length of $\lambda/4 = c/(4\sqrt{\epsilon}f_0) = 58\mu m$. The ratio of the width of the two transformers is determined from the required impedance conversion factor, which is equal to $(Z_{C2}/Z_{C1})^2$. Here Z_{C1} and Z_{C2} are the characteristic impedances of the two quarter-wave transformers, and Z_{C2} is connected to the source. We find that $Z_{C2}/Z_{C1} = 11.8$ which means that the width of the first transformer should be 11.8 times the width of the second transformer. An actual layout view of the tuning inductor and the two transformers can be seen in figure 4.2.

These initial design values are for an ideal lossless microstrip line and real source impedance. However, in practice these are not completely correct. Therefore, an extensive computer program is written that takes into account the losses and the complex frequency-dependent source impedance. In chapter **??** optimum dimensions are calculated for the microstrip lines using this program. But before that, we need to look at how microstrip lines are modeled.

4.2 General characteristics of transmission lines

A transmission line is a distributed element which can be thought of as an infinite ladder of series impedances and shunt admittances, as shown in figure 4.3, where series resistance R, inductance L, shunt conductance G, and capacitance C are distributed quantities, measured per unit length [65]. Let $Z = R + j\omega L$ and $Y = G + j\omega C$, where ω is the angular frequency. By solving the

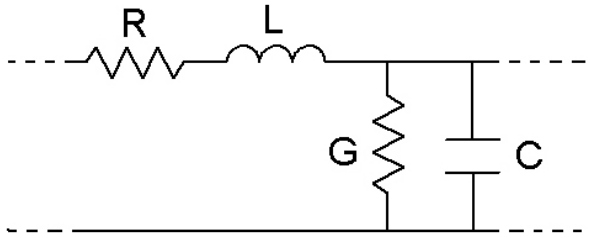

Figure 4.3: Equivalent circuit of a transmission line.

appropriate transmission line equations, the voltage and current on the line are of the shape

$$V(z) = V(0)\exp -\gamma z, \tag{4.5}$$

$$I(z) = I(0)\exp -\gamma z \tag{4.6}$$

which are of wave nature. The propagation constant $\gamma = \alpha + j\beta$ of the voltage and current waves is determined by

$$\gamma = \sqrt{ZY} = \sqrt{(R + j\omega L)(G + j\omega C)}, \tag{4.7}$$

with α the attenuation constant and β the phase constant. The power transmitted on the line is

$$P(z) = Real\{V(z)I^*(z)\} = P(0)\exp(-2\alpha z) \tag{4.8}$$

The power attenuation is hence given by 2α.
The propagation wavelength inside the transmission line is determined by

$$\lambda = \frac{2\pi}{\beta} \tag{4.9}$$

The characteristic impedance of the line, defined by the ratio of the voltage to the current (in the absence of reflections), is

$$Z_0 = \sqrt{Z/Y} = \sqrt{(R + j\omega L)/(G + j\omega C)}. \tag{4.10}$$

The losses contributed by the conductors are represented by R, which is related to the surface impedance of the conductors. The losses in the dielectric are represented by G and are usually less important than R, *i.e.*, we assume $G = 0$. The series inductance L includes contributions from the surface impedance as well as that related to the magnetic flux in the space around the conductors (the geometric inductance).

4.3 Design equations for microstrip lines

The equations describing the superconducting microstrip lines in this work, are mainly a combination of microstrip line models in [66, 65, 67] and models for the frequency dependant complex conductivity of superconductors [72]. We will first consider the standard equations for a microstrip. Then we will introduce the more accurate formulae based on the work of Yassin and Withington [67]. Figure 4.4 shows the geometry of a microstrip line. The series impedance per unit length of the line is determined by

$$Z = j\omega\mu_0 \frac{t_d}{W_{eff}} + \frac{Z_{s1} + Zs_2}{W_{eff}} \tag{4.11}$$

where the first term is the geometrical inductance which accounts for the magnetic flux around the conductors, and the second term is due to the surface impedance of the conductors. Due to the finite thickness of the top strip line, the field penetrates over a larger width (fringing) which is taken into account by an effective width W_{eff} as [66]

$$W_{eff} = W + \frac{1.25t_s}{\pi}\Big(1 + \ln\frac{2t_d}{t_s}\Big) \tag{4.12}$$

The admittance per unit length of the line is

$$Y = j\omega\epsilon_0\epsilon_{eff}(f)\frac{W_{eff}}{t_d} \tag{4.13}$$

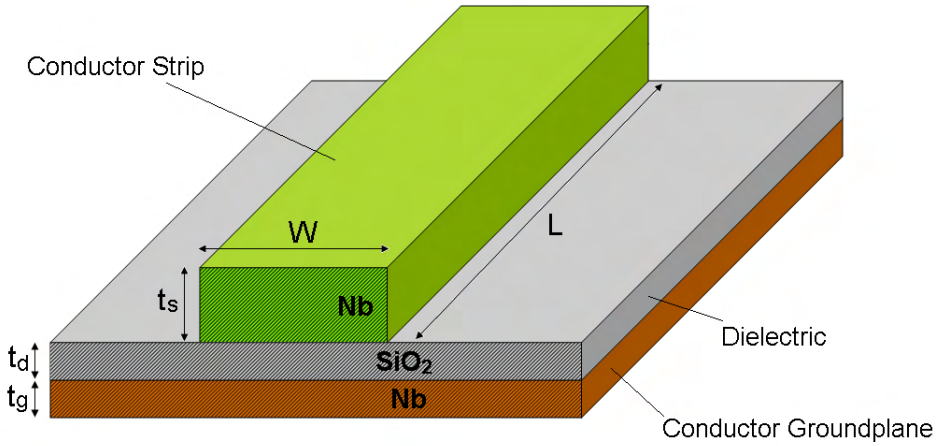

Figure 4.4: Layout of a microstrip line

in which $\epsilon_0 = 8.854 \times 10^{-12}$F/m is the permittivity of space space, and $\epsilon_{eff}(f)$ is the effective frequency-dependent relative permittivity of the dielectric. In this work, dispersion effects at high frequencies are taken into account by using the empirical formula given in [68] which is the most accurate formula applicable to high frequencies. This formula has been verified up to 80 GHz, which is still much below 660 GHz. Nevertheless, despite the lack of such accurate analysis at submillimeter wavelengths, we use it. It is given by

$$\epsilon_{eff}(f) = \epsilon_r - \frac{\epsilon_r - \epsilon_{eff}(0)}{1 + (f/f_{50})^m} \tag{4.14}$$

where

$$f_{50} = \frac{f_{K,TM_0}}{0.75 + \left(0.75 - 0.332\epsilon_r^{1.73}\right)\frac{W}{t_d}} \tag{4.15}$$

$$f_{K,TM_0} = \frac{ctan^{-1}\left\{\epsilon_r\sqrt{\frac{\epsilon_{eff}(0)-1}{\epsilon_r - \epsilon_{eff}(0)}}\right\}}{2\pi t_d\sqrt{\epsilon_r - \epsilon_{eff}(0)}} \tag{4.16}$$

The expression for m is too extensive to be presented but can be found in the original paper [68].
ϵ_r is the relative dielectric constant and for our SiO2 dielectric it is 3.8 .
$\epsilon_{eff}(0)$ is the static effective permittivity, and is given by [66] as

$$\epsilon_{eff}(0) = \frac{\epsilon_r + 1}{2} + \frac{\epsilon_r - 1}{2}\left(1 + 10t_d/W\right)^{-0.555} - \Delta\epsilon_{eff}(t) \tag{4.17}$$

where

$$\Delta\epsilon_{eff}(t_s) = \frac{(\epsilon_r - 1)t_s/t_d}{4.6\sqrt{W/t_d}} \tag{4.18}$$

$\Delta\epsilon_{eff}(t_s)$ is a term that is subtracted because of the effect of the finite thickness of the top strip line in the microstrip, which causes part of the electric field to go through the air reducing the

effective permittivity. It should be noted that different formulae regarding the effective width and effective permittivity have been reported in the literature. A review of these is given in [66]. The chosen effective permittivity formulae here are based on the most accurate ones, taking into account the conditions that have to be met for the formulae to be applicable.

4.3.1 Modified microstrip line model

In this model we use the equations suggested by Yassin and Withington [67] for superconducting microstrip lines. In the previous more simple model, it was assumed that the longitudinal current is uniformly distributed across the whole width of the effective strip. However, it is known [75] the current density rises rapidly towards the edges of the strip. This will modify, for certain geometries, the kinetic inductance of the superconducting lines.
The current denisty has been simulated with the free student-version Ansoft Maxwell software, for the actual dimensions used in this work. Due to the lack of possibility to define complex conductivity or surface impedance in this program, Nb was treated with a real conductivity and an equivalent negative dielectric constant. This equivalent dielectric constant can be easily calculated by using the relevant Maxwell equation as follows:

$$\begin{aligned} \nabla \times \mathbf{H} &= j\omega\epsilon\mathbf{E} + \sigma\mathbf{E} \\ &= j\omega\epsilon\mathbf{E} + (\sigma_1 - j\sigma_2)\mathbf{E} \\ &= j\omega(\epsilon - \sigma_2/\omega)\mathbf{E} + \sigma_1\mathbf{E} \end{aligned} \tag{4.19}$$

where $\epsilon_{equiv} = \epsilon - \sigma_2/\omega$ is the equivalent dielectric constant for the superconductor, which is a negative value. The usage of a negative ϵ in the software is a point of uncertainty, since it is not know whether the software's calculation is reliable in this case. Nevertheless, it was used as it should at least give us a clue of how the current distribution looks like. The simulated current density distribution is shown in figure 4.5(a). We see that indeed the current density is very non-uniform and therefore using Yassin's model is justified.

Yassin's model is based on a rigorous treatment based on conformal transformations for microstrip lines when modal dispersion can be neglected. In the frequency range of ALMA band 9 (600-720 GHz), the propagation wavelength inside the Nb microstrip lines is approximately 220 μm. Since this propagation wavelength is, in the worst case, more than 4 times larger than the cross sectional dimensions of the microstriplines, modal dispersion can be neglected. The model takes into account the thickness of the film and the non-uniform current distribution on the top and ground plane, and is the most accurate analytical scheme available for calculating the characteristics and losses in the microstrip lines.

In this model, the series impedance and shunt admittance per unit length are defined as follows:

$$Z = j\omega\mu_0 g_1 + 2g_2(Z_{s1} + Z_{s2}) \tag{4.20}$$

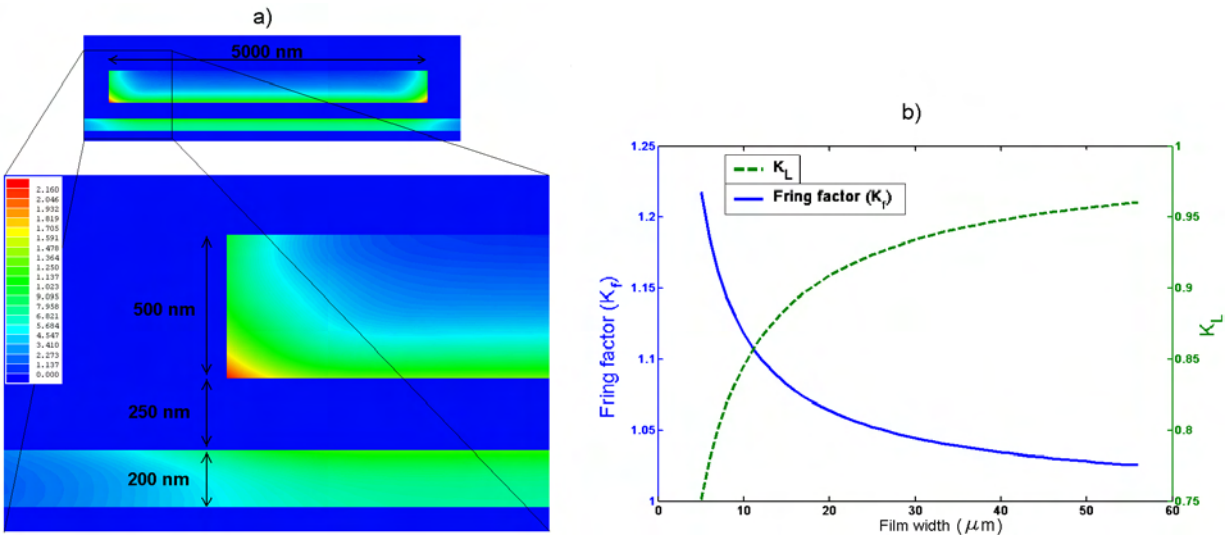

Figure 4.5: (a) Current density **J** simulated by Ansoft Maxwell for a cross section of a Nb superconducting microstrip line at a frequency of 600 GHz and temperature of 4.2 K. The thickness of the top strip line and ground plane are 500 nm and 200 nm respectively. The SiO_2 dielectric layer is 250 nm thick and has a relative permittivity of 3.8 . The legend indicates the value of the current density in arbitrary units. (b) Calculation of the fring factor K_f and K_ℓ in Yassin's model [67] as a function of top strip width for ALMA devices. The top strip and dielectric thicknesses are assumed to be 500nm and 250 nm respectively.

$$Y = j\omega\epsilon\frac{1}{g_1} \tag{4.21}$$

where g_1 and g_2 are geometrical factors which characterize the particular transmission line. g_1 parameterizes the geometry insofar as the external field in concerned and is defined as follows:

$$g_1 = \frac{t_d}{WK_f} \tag{4.22}$$

g_2 parameterizes the geometry insofar as the field penetrating inside the conductor is concerned and is defined as:

$$g_2 = \frac{K_\ell}{W} \tag{4.23}$$

K_f is the fring factor, and defines an equivalent strip width. It is a function of strip width W, strip thickness t_s, and dielectric thickness t_d. Care should be taken not to use equation 4.12, when using Yassin's model. Exact analytical formulae for the calculation of $K_f(W, t_s, t_d)$ and $K_\ell(W, t_s, t_d)$ is two lengthy and will not be presented here as they are available in [67]. However, for the case of our microstrip lines, it has been calculated and is presented in figure 4.5(b). We see that as the top strip width becomes smaller, the effects of the nonuniform current distribution become more apparent. Therefore, these factor will change the characteristics of the high-impedance transformer and the tuning inductor much more than the low-impedance transformer.

By knowing Z and Y all the properties of the microstrip line can be calculated. However, we still need to find the surface impedances Z_{s1} and Z_{s2}.

4.4 Surface Impedance

Non-ideal conductors have a surface impedance Z_s which affects the characteristics of microstrip lines. For a thin conductor film of thickness t, the surface impedance is defined for a sinusoidal electric field $E_x(z,\omega)$ and current density $J_x(z,\omega)$ [69] as

$$Z_s(\omega) = \left.\frac{E_x}{H_y}\right|_{z=0} = \frac{E_x(0,\omega)}{\int_0^t dz J_x(z,\omega)}. \tag{4.24}$$

The real part of Z_s, called the surface resistance, accounts for microstrip losses and the imaginary part, the surface reactance, contributes to the microstrip lie inductance.

4.4.1 Normal Conductors

When the electric field penetration depth is long compared to the electron mean free path, a local equation can be assumed for the relation between **J** and **E**:

$$\mathbf{J} = \sigma \mathbf{E}, \tag{4.25}$$

where σ is the complex conductivity. If the thickness t of a conductor is not very much greater than the field penetration depth, a filed on one side of the conductor penetrates partially through to the other side. In this case, solving the Maxwell equations in the local theory, we obtain the normal skin effect surface impedance [70, 71]:

$$Z_s = \Big(\frac{j\omega\mu_0}{\sigma}\Big) \coth\Big[t\sqrt{j\omega\mu_0\sigma}\Big]. \tag{4.26}$$

To be very accurate, evaluation of the surface impedance also requires boundary conditions regarding the scattering of electrons from the conductor surface to be taken into account.Tthe procedure can be found in [69].
For normal metals the conductivity σ_n is a real value if we ignore the time relaxation effect. However, for superconductors, this is not the case, as we will see next.

4.4.2 Superconductors

For superconductors the surface impedance should be calculated by using the general non-local Mattis-Bardeen theory [72]. However, if the electron mean free path ℓ_e is much smaller than the field penetration depth λ, that is, $\ell_e \ll \lambda$, the local limit theory for metals in equation 4.26 can be used. The calculation can be simplified if the films are thick enough to use a bulk limit approximation for the surface impedance. Actually, it was found [73] that if the thickness is more than three times the superconducting penetration depth, the bulk limit solution is a very

good approximation to the exact solution [1].
In order to calculate the complex conductivity of a superconductor to be used in equation 4.26, we use the Mattis-Bardeen theory in the extreme anomalous limit (or extreme dirty limit) where $\ell_e \ll \xi_0$ [33]. This is justified for our Nb microstrip lines, since $\ell_e \sim 5 - 10$ nm at 4.2 K and $\xi_0 = 40$nm .[2] A complex conductivity $\sigma = \sigma_1 - j\sigma_2$ is conveniently introduced in this approximation. σ is a function of frequency, temperature, and can be calculated if the energy gap Δ and the normal-state conductivity at the superconducting transition temperature σ_n are known:

$$\frac{\sigma_1}{\sigma_n} = \frac{2}{\hbar\omega}\int_{\Delta}^{\infty}[f(E) - f(E+\hbar\omega)]g(E) + \frac{1}{\hbar\omega}\int_{\Delta-\hbar\omega}^{-\Delta}[1 - 2f(E+\hbar\omega)]g(E)dE, \tag{4.27}$$

$$\frac{\sigma_2}{\sigma_n} = \frac{1}{\hbar\omega}\int_{\Delta-\hbar\omega}^{\Delta}\frac{[1 - 2f(E+\hbar\omega)][E^2 + \Delta^2 + \hbar\omega E]}{(\Delta^2 - E^2)^{1/2}[(E+\hbar\omega)^2 - \Delta^2]^{1/2}}dE, \tag{4.28}$$

where f(E) is the Fermi function:

$$f(E) = \frac{1}{1 + e^{E/k_BT}} \tag{4.29}$$

and

$$g(E) = \frac{E^2 + \Delta^2 + \hbar\omega E}{(E^2 - \Delta^2)^{1/2}[(E+\hbar\omega)^2 - \Delta^2]^{1/2}}. \tag{4.30}$$

The first integral in equation 4.27 represents the conduction of thermally excited normal electrons, while the second integral accounts for the contribution of photon-excited quasi-particles and is zero for $\hbar\omega < 2\Delta$. σ_2 describes the effect of superconducting paired electrons (Cooper pairs). The lower limit on the integral for σ_2 becomes $-\Delta$ when $\hbar\omega > 2\Delta$.

The value for σ_n for Nb depends critically on the material quality and conditions that it was made with. DC Measurements of conductivity for films of 200 nm and 500 nm thickness, yields values around 2.4×10^7 S/m. However, we suspect that the Nb film growth does not yield uniform quality across the thickness - at least within the first 50 nm. Therefore since DC measurements will give an average of the conductivity across the film, it is not the correct value to be used for the calculation of the complex conductivity. The effect of this on the simulations will be explained later.

Figure 4.6 shows the calculated complex conductivity $\sigma = \sigma_1 - j\sigma_2$ as a function of frequency for Nb at 4.2 K. We can see that at the Nb superconducting gap frequency ($f_g = \frac{2\Delta}{h} \simeq 680$ GHz), σ_1 rises rapidly due to the addition of the quasi-particles to the normal electrons.
Now having calculated the complex conductivity, we can place it in the normal skin effect formula (equation 4.26) to calculate the surface impedance. In figure 4.7, the real and imaginary parts of Z_s for Nb at 4.2 K are plotted. Note the real part of surface impedance increases sharply at the Nb gap frequency.

[1] In this work, the thickness of the top strip line in the microstrip lines is larger than 3 times the penetration depth. But for the ground plane, this is not the case.

[2] ℓ_e has been measured from resistivity measurements of Nb. Since the $\rho\ell_e$ product is approximately constant in bulk metal [**?**], ℓ_e can be calculated.

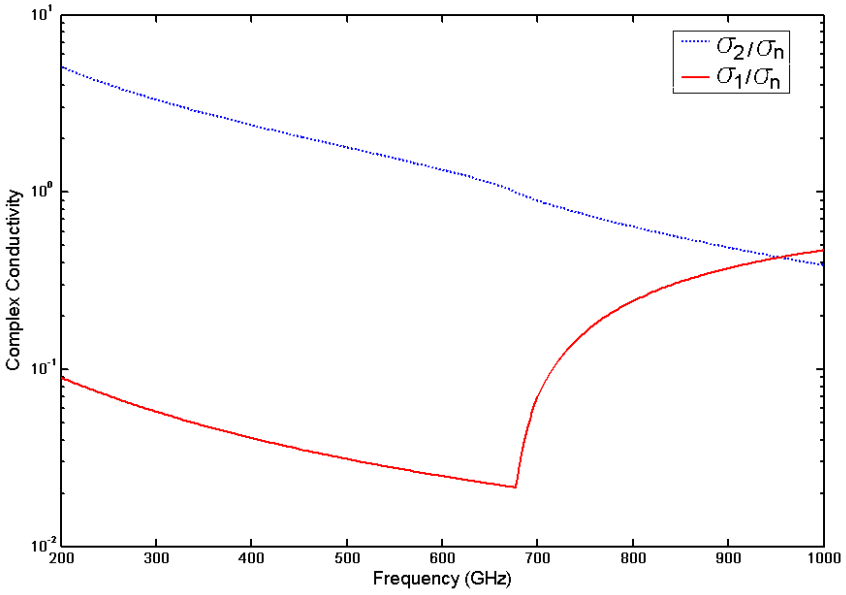

Figure 4.6: Calculated normalized complex conductivity $\sigma/\sigma_n = (\sigma_1 - j\sigma_2)/\sigma_n$ for superconducting Nb at 4.2 K. The energy gap is 2.8 meV. The Nb normal-state conductivity σ_n just above the transition temperature 9.2 K, is measured 2.4E7 S/m (4.2 $\mu\Omega$-cm).

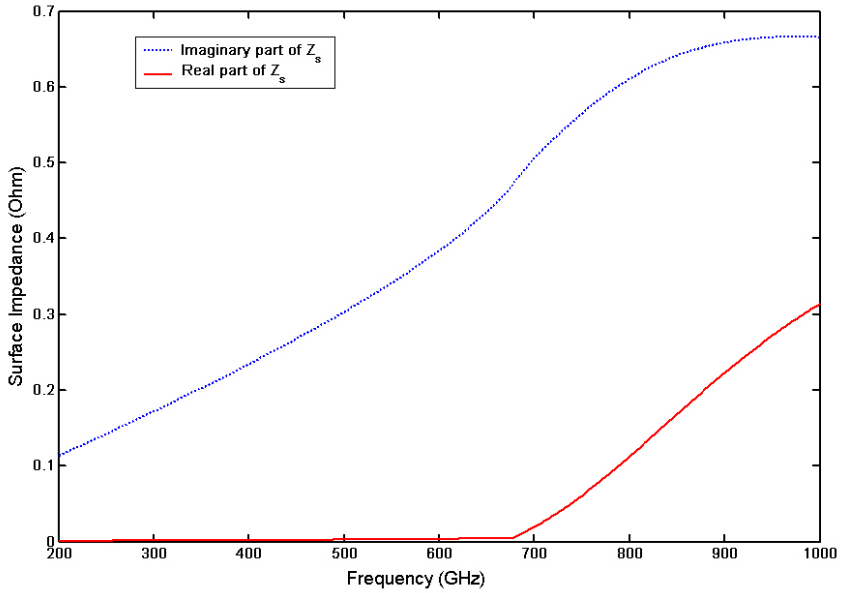

Figure 4.7: Calculated real and imaginary parts of surface impedance Z_s for a 0.5 μm thick Nb layer at 4.2 K. Note the sharp increase in the real part at the superconducting gap frequency (680 GHz).

4.5 Calculation of RF coupling efficiency

The goal in tuning circuit design is to achieve optimum RF coupling efficiency in the frequency band of interest. Often it is necessary to optimize the design using computer-aided programs. There are commercial software like Advanced Design System (Agilent EEsof Inc.) for circuit simulation and optimization. However, these programs do not have the capability to deal with superconducting transmission line parameters. They calculate the conductor losses using the normal skin effect in normal metals , while we need to use as input the complex conductivity in the extreme anomalous limit for Nb. It is possible to convert the superconducting parameters into equivalent normal-metal parameters to utilize these programs, however since it is not possible to use frequency dependant conductivity in these programs, it becomes extremely time consuming. Nevertheless, this has been done with Advanced Design System to some extent, and reasonable results were obtained. These results will be presented later in ??.

However, to avoid this, we have developed our own simulator program, in which superconducting transmission lines are modeled using the models discussed in previous sections. The program was originally written in Mathematica, but was later rewritten in MATLAB. This program is based on two-port network analysis of microwave circuits, which will be described now.

4.5.1 Two-port network analysis of microwave circuits

A microwave circuit can be modeled as a collection of two-port networks that are connected in series, parallel or cascade. In figure 4.8(a) a two-port network with voltage and current at each port is represented. Note the direction of the currents defined. The relationship between

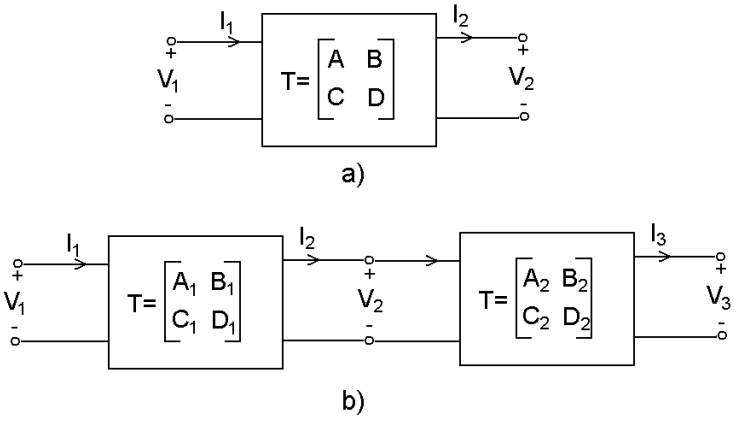

Figure 4.8: (a) A two-port network. (b) A cascade connection of two-port networks.

the currents and voltages can be defined in many ways. But there is one specific way that will always be possible, and that is the ABCD matrix (or T for transmission matrix) representation:

$$\begin{bmatrix} V_1 \\ I_1 \end{bmatrix} = \begin{bmatrix} A & B \\ C & D \end{bmatrix} \begin{bmatrix} V_2 \\ I_2 \end{bmatrix} \tag{4.31}$$

For a specific circuit, the parameters A,B,C,D can always be calculated. For example, for a transmission line with characteristic impedance Z_c, propagation constant γ, and length L, the matrix is:

$$T_{transmission-line} = \begin{bmatrix} \cosh(\gamma L) & Z_c \sinh(\gamma L) \\ 1/Z_c \sinh(\gamma L) & \cosh(\gamma L) \end{bmatrix} \tag{4.32}$$

In a cascade system like in figure 4.8(b), the total transmission matrix is the multiplication of the individual matrices:

$$T = T_1 T_2 \tag{4.33}$$

Now consider a system shown in figure 4.9. This is a schematic representation of the actual RF equivalent circuit for our SIS mixer. The source impedance, which is actually impedance of the antenna, the waveguide, and the probe point shown in figure 2.11, has an impedance with a real and imaginary component, R_a and X_a respectively. The SIS junction has a resistance of R_j which is approximately equal to its normal-state resistance R_n, and a geometrical capacitance C_j. In between, there are tuning circuits which are basically lossy transmission lines, with characteristic impedance Z_c1 to Z_cn, and propagation constants γ_1 to γ_n. The elements inside the network indicated with dashed lines, will have an equivalent T matrix. The RF coupling

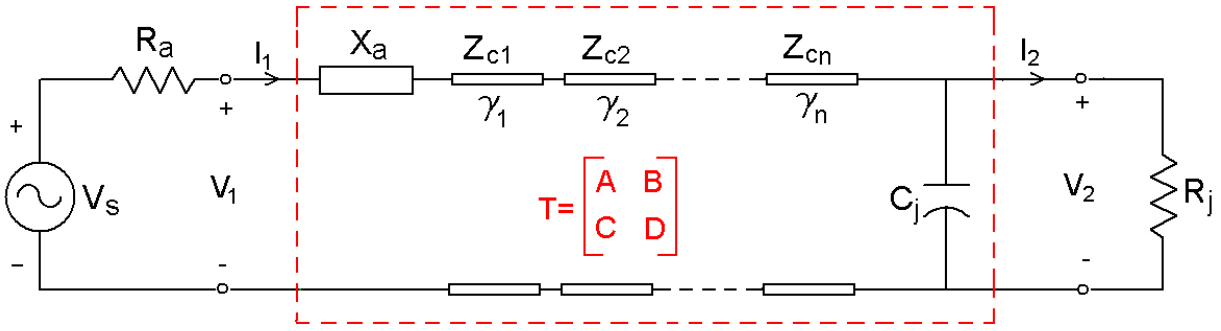

Figure 4.9: Schematic circuit of an SIS mixer, including the tuning circuits.

efficiency between the source and the load (R_j), is defined as the ratio of the power delivered to the load (P_{load}) to the power available from the source (P_{avs}) - the maximum power that can be delivered to the network:

$$\eta_{RF} = \frac{P_{load}}{P_{avs}} \tag{4.34}$$

In order to calculate this, we have to solve equation 4.31, plus the two equations describing the outside of the network. By doing this, we get:

$$P_{load} = 1/2(V_2 I_2^*) = \frac{1/2 R_j V_s^2}{|AR_j + B + CR_a R_j + DR_a|^2} \tag{4.35}$$

The source will deliver maximum power to the network, when the network is conjugately matched with the source. In that case:

$$P_{avs} = 1/2\frac{(V_s/2)^2}{R_a} = \frac{V_s^2}{8R_a} \tag{4.36}$$

Therefore, the RF coupling efficiency of the mixer is:

$$\eta_{RF} = \frac{4R_aR_j}{|AR_j + B + CR_aR_j + DR_a|^2}. \tag{4.37}$$

The frequency dependent source impedance $Z_s = R_a + jX_a$, should be separately calculated and used as an input to the program. The calculation of the source impedance, requires simulation of the horn antenna, waveguide, and probe point with a high-frequency field simulator. We have used Ansoft HFSS and Microwave Studio for this purpose, as will be discussed next.

4.5.2 RF source impedance

The RF source impedance, is the impedance seen when from the probe point and away from the junction (Figure 2.11 and 2.12). This is regarded as $Z_s = R_a + jX_a$ in figure 4.9, and was initially calculated using Microwave Studio. Later, a more accurate simulation using Ansoft HFSS (High Frequency Structure Simulation) was performed. Both these programs use the finite element method in 3 dimensions and solve numerically for the fields inside and outside the conductors. Since the probe point is integrated on the chip and is made out of superconducting Nb, none of these programs can correctly simulate this component. A perfect-metal approximation has been made for the probe point, so that its effect on the fields inside the waveguide can be approximately taken into account in Microwave Studio and HFSS. However, this approximation is only valid

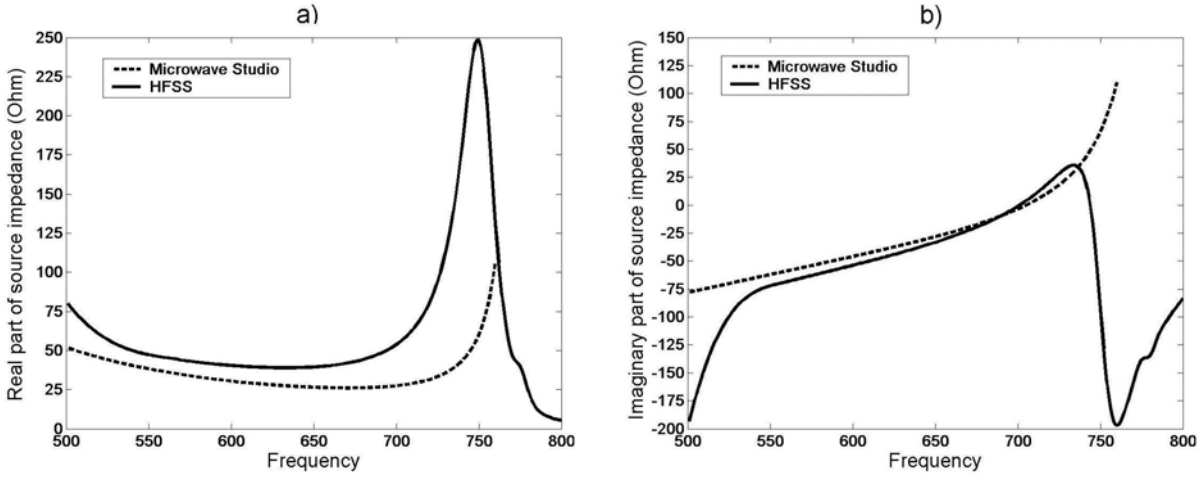

Figure 4.10: RF source impedance calculated with Microwave studio and HFSS. The impedance includes the impedances of the probe point, waveguide, and horn antenna.

for frequencies below the Nb gap frequency where the losses are negligible, and therefore more

accurate simulation of the probe point itself is still a point of concern for the modeling. Several designs for the probe point were made to increase the RF bandwidth and coupling. The design of the horn antenna and waveguide are fixed and have only one design. Figure 4.10 shows the RF source impedance used in our computer program to calculate the RF coupling efficiency. It can be seen that in the frequency range 600-720 GHz, there is quite a difference between the two simulations, especially in the real part which determines the loss. The effect of the two different source impedances on the RF coupling efficiency simulations is large, and is still a point of concern for us. However, due to the easier access to HFSS we will use its results throughout the thesis. It should be noted that such commercial programs are designed for the microwave frequency range, and not for the THz frequency range, and therefore do not have the required accuracy. The simulated RF source impedance is used as input to our program to calculate RF coupling efficiency.

4.6 Initial tuning circuit design for ALMA band 9

The initial design for the microstrip tuning circuits for ALMA band 9 (600-720 GHz), was based on a previous design work that has a long history behind it. We will not introduce this history here; instead we will directly go to presenting the specifications.

ALMA band 9 was based on Nb/AlOx/Nb SIS junctions integrated with Nb microstrip line tuning circuits. The nominal design values for the SIS junction parameters and the tuning circuit material parameters are given in table 4.1. These parameters are based on the material fabrication capabilities and technology at that time. The tuning circuit geometry used in ALMA band 9 is

Table 4.1: Initial Nb/AlOx/Nb SIS junction and Nb tuning circuit design parameters for ALMA band 9.

SIS junction parameters	
R_n	25 Ω
C_s	80 fF/μm^2
A (area)	1.0 μm^2
R_nA	25 $\Omega\mu$m^2
C_j	80 fF
V_g	2.8 mV
J_c at T=4.2 K	8.4 kA/cm^2
Nb Tuning circuit material parameters	
σ_n at 10 K (DC)	1.3×10^7 S/m
V_g at 4.2 K	2.8 mV
ϵ_r (SiO2)	3.8
T_c	9.25 K

shown in figure 4.11. There are eight geometrical parameters, namely L_1 and W_1 for the high impedance transformer, L_2, W_2, L_A, and L_B for the low impedance transformer, and L_3 and W_3 for the tuning inductor. Based on these parameters, two main different sets of geometries were designed: the "tapered design" and the "non-tapered design". In the latter, $L_A = 0$ and $L_B = 0$, reducing the parameter to 6. The values for the two main design geometries are presented in table 4.2. However, as it will become clear later, many different parameter variations, either

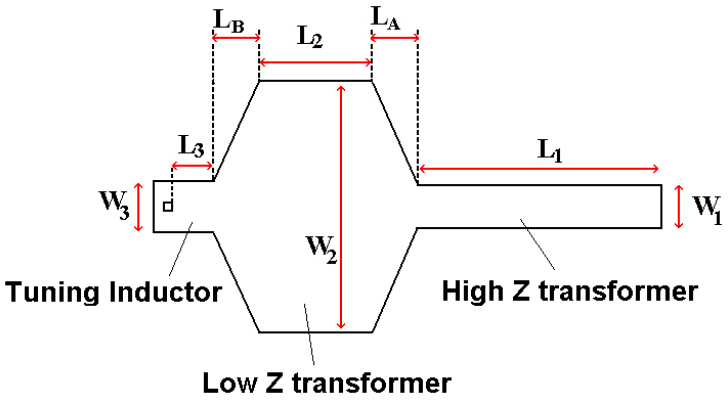

Figure 4.11: The tuning circuit geometry for ALMA band 9. Initially, two different designs depending on whether $L_A = L_B = 0$ (non-tapered) or $L_A = L_B = 6.6\mu$m (tapered) were made.

Table 4.2: Initial tuning circuit geometries for for ALMA band 9.

	Tapered	Tapered high-shifted	Tapered low-shifted	Non-tapered
$L_1 \times W_1$ ($\mu m \times \mu m$)	34×6	34×6	34×6	41×4.8
$L_2 \times W_2$ ($\mu m \times \mu m$)	19.8×56	19.8×56	19.8×56	30×37
$L_3 \times W_3$ ($\mu m \times \mu m$)	5×6.5	5×7.5	5.5×5.5	8.5×6.5
L_A (μm)	6.6	6.6	6.6	0
L_B (μm)	6.6	6.6	6.6	0
t_d (nm) (SiO_2)	250	250	250	250
t_s (nm) (Nb)	500	500	500	500
t_g (nm) (Nb)	200	200	200	200

in material parameters or in geometrical parameters, exist during the fabrication. As a result, the behavior of the coupling efficiency η_{RF}, will change, shifting or reducing the bandwidth. To overcome this problem to some extent, two extra designs, namely the "high-shifted" and the "low-shifted" designs, were added to the initial tapered design. These two extra designs, differ in L_3, W_3 or both, compared to the initial design. It was found that changing the tuning inductor length or width (L_3 or W_3) by a small amount, has a significant influence on the position of the

center frequency of η_{RF}, therefore allowing us to tackle the problem by compensating the parameter variations in this way. But as a trade off, more devices have to be fabricated and measured, to find a suitable candidate.

Simulations of the four designs presented in table 4.2 are shown in figure 4.12. We can see that for the tapered designs, non of the designs really cover the full bandwidth of 600-720 GHz sufficiently. As for the non-tapered design, the bandwidth coverage is better on the lower side, but becomes worse on the higher side compared to the tapered designs. Moreover, the coupling efficiency is also lower in the non-tapered, meaning that more of the signal power is lost, causing an increase in the equivalent input noise power of the receiver. As a result, optimization of the tuning circuit dimensions has to be performed, in order to get the full potential out of the circuit. This will be the subject of chapter 5.

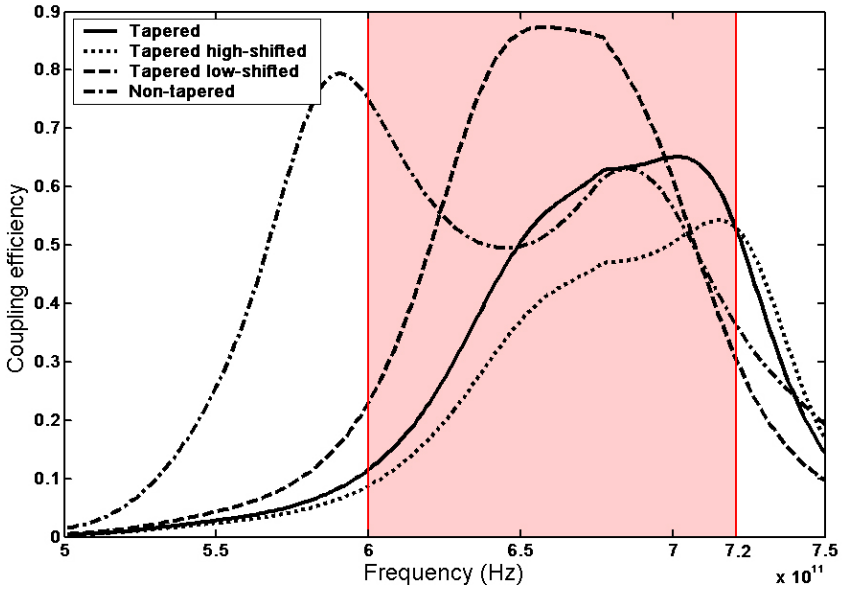

Figure 4.12: Initial simulations for the RF coupling efficiency using parameters from table 4.1 and 4.2 for ALMA band 9 and the design equations described in section 4.3. Four different designs given in table 4.2 are indicated. The desired bandwidth and frequency range is indicated in red.

4.7 Influence of parameter variations in RF coupling efficiency

In this section we will look at some of the important variations that can occur either in material parameters or geometrical parameters, which can affect the RF coupling efficiency bandwidth, absolute value, or both. Most of the times it is a combination of bandwidth and absolute value

that occurs. Because of the very complicated behavior of the RF coupling that originates from the non-linear behavior of the Nb tuning circuits and the source impedance, it is very difficult to predict the effect of these variations, without doing a simulation.

4.7.1 SIS junction properties variations

The SIS junction is subject to some variations which will be described here. These include variations in the junction capacitance C_j, junction normal-state resistance R_n and junction critical current density J_c.

Variations in C_j can occur as a result of variations is the specific capacitance C_s of the junction. The nominal value for C_s in our designs is 80 fF/μm^2. Small changes in the oxidation time of the AlOx barrier growth, performed during the trilayer deposition (section 3.3), have a linear influence on the thickness of the AlOx, which translates into variations of C_s defined in equation 2.12. If the junction area is kept constant, and the thickness reduced, C_j increases, causing a shift in the RF coupling to the left. On the other hand, R_n decreases. Since the R_nC_j product is exponentially dependant on thickness, it will reduce exponentially, causing a reduction in the maximum attainable bandwidth. A change of $\pm$5fF/μm^2 in C_s is very probable. It should be noted that variations in C_s can happen between different fabrication runs, but do not happen between different devices in one batch.

Variations in C_j can also occur as a result of variations in the junction area. This can be caused by inaccuracy in the junction resist patterning (section 3.3) resulting in an area between 0.9×0.9 and $1.1 \times 1.1 \mu$m^2. This translates into capacitance variations of $\pm 20\%$ around 80fF. However, the R_nC_j product will remain constant, not changing the maximum attainable bandwidth. But the observed bandwidth will change. This shown in figure 4.13(left).

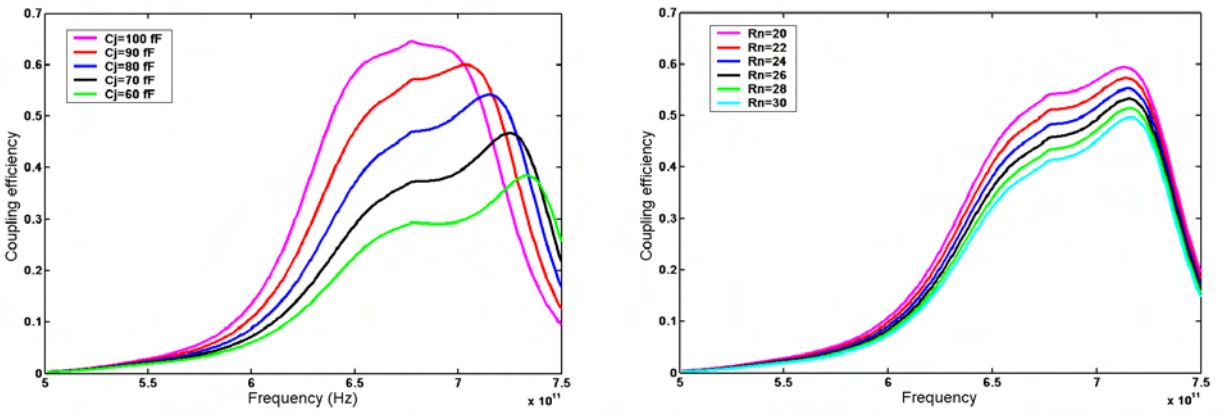

Figure 4.13: Influence on the RF coupling due to: (Left) Change in junction capacitance due to variations in junction area of $\pm 20\%$ around the design value of 1 μm^2 ($C_j = 80$ fF). (Right) Change in junction resistance R_n due to variations in junction area, assuming a constant C_j.

As a result of junction area variations or barrier thickness variations, R_n and C_j both change as was discussed above. However, an evaluation of the effect on RF performance due to variations in R_n alone (assuming that somehow C_j stays constant), shows that this will only cause minor changes in the absolute value of RF efficiency, and much less in the bandwidth. This shown in figure 4.13(right).

4.7.2 Geometrical variations

A number of geometrical parameter variations exist that can occur during the fabrication of the devices, or the installation of the devices.
In picture 4.12 we saw that for small variations in the length or width of the tuning inductor piece (L_3 and W_3 in figure 4.11) as small as 1 μm, the RF coupling efficiency value and bandwidth can change dramatically. However, since electron-beam lithography technology is used for the fabrication of the devices (section 3.3), the intrinsic error in length and width size for the tuning circuit, is governed by the alignment accuracy of the two masks, and not by the e-beam writing itself. In this work, the alignment accuracy is around 100 nm. Therefore, we can safely assume that variations is tuner dimensions are too small to have a major effect on the RF coupling.

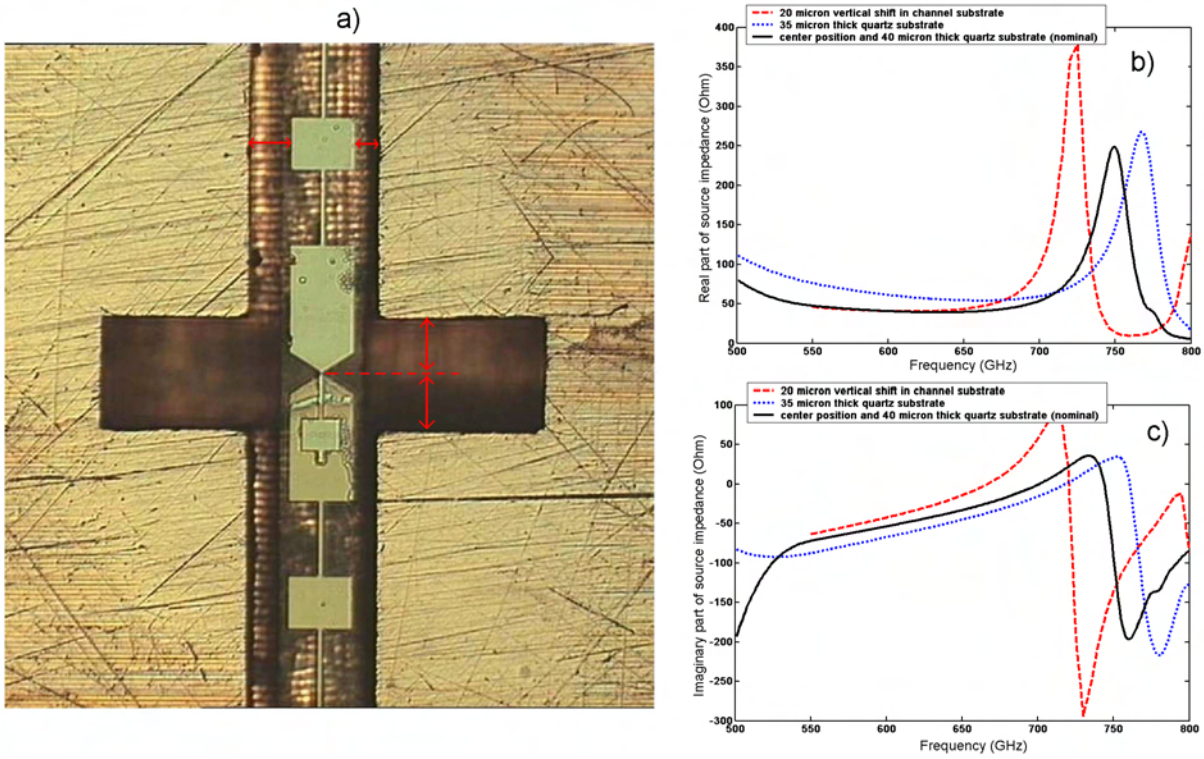

Figure 4.14: (a)The actual substrate channel in the copper mixer block with a device in it. (b) and (c) Change in source impedance as a result of vertical positioning error in the channel (dashed) or thickness error of the quartz substrate (dotted).

A very important geometrical error that is responsible for unwanted variations in the RF coupling efficiency, occurs when the SIS devices are mounted in the substrate channel in the waveguide. The waveguide and substrate channel are shown in picture 2.11(a). The actual substrate channel in the copper mixer block is shown in figure 4.14(a) with the device in the channel.

Two factors play a role in the accuracy of the mounting. The first is the accuracy with which the diced device (mixer chip) is mounted in the channel substrate. The reported accuracy for positioning the device exactly in the middle is $\pm 20\mu$m. The change in source impedance as a result of 20μm vertical shift in the channel is shown in figure 4.14(b) and (c) with dashed lines. The corresponding effect in RF coupling efficiency is shown in figure 4.15 with dashed lines.
The second, is the accuracy with which the quartz substrate of the device is made thinner. The original thickness of quartz during fabrication is 200μm. Before mounting, the thickness is reduced to a nominal design value of 40μm. The reported accuracy of this step is $\pm 10\mu$m. The change in source impedance as a result of 5μm thinner substrate is shown in figure 4.14(b) and (c) with dotted lines. The corresponding effect in RF coupling efficiency is shown in figure 4.15 with dotted lines.

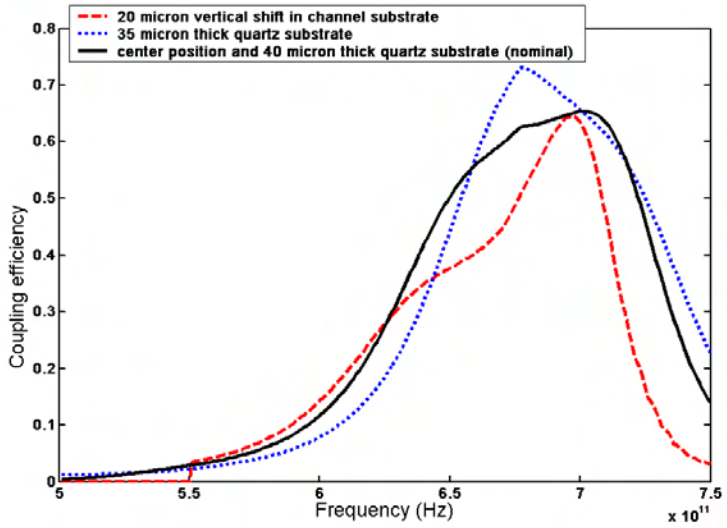

Figure 4.15: The effect on coupling efficiency as a result of vertical positioning error in the channel (dashed) or thickness error of the quartz substrate (dotted).

The error due to device positioning in the channel or substrate thickness reduction, is the most prominent error that we suspect, and is based mostly on human error. The error can be reduced to some extent, but will remain as a fact that has to be considered in the design of tuning circuits. As a result, the design bandwidth has to be larger than the required bandwidth, in order to be less sensitive to this error. However, because of the intrinsic limit in bandwidth due to the RC product of Nb/AlOx/Nb junctions which is reported to be approximately 100 GHz [78], it is difficult to cope with this problem for the case of ALMA band 9 bandwidth which is 120 GHz.

4.7.3 Film properties variations

An important, yet not well studied variation, is the gradual change in the superconducting energy gap (2Δ) in the Nb films. When the ground plane and wiring layers are deposited (section 3.3), depending on the intrinsic mechanism of Nb growth as well as the underlying substrates that they grow on, the quality of the Nb crystallinity gradually increases with growth. In the microstrip lines used in this work, the current density strongly increases when we go towards the dielectric layer (figure **??**(a)). The effect is that the current in the top strip will see mostly the low quality Nb layers, while in the ground plane it will see mostly higher quality layers. Therefore, we suspect that this will have an influence on the modeling, especially regarding the top strip. It is not easy to find out what the exact influence is on the coupling efficiency, however, we can assume that an equivalent superconducting gap Δ_{eqv} can be defined. In figure 4.16(left) the coupling efficiency has been calculated for different equivalent gap voltages of the top strip line. An

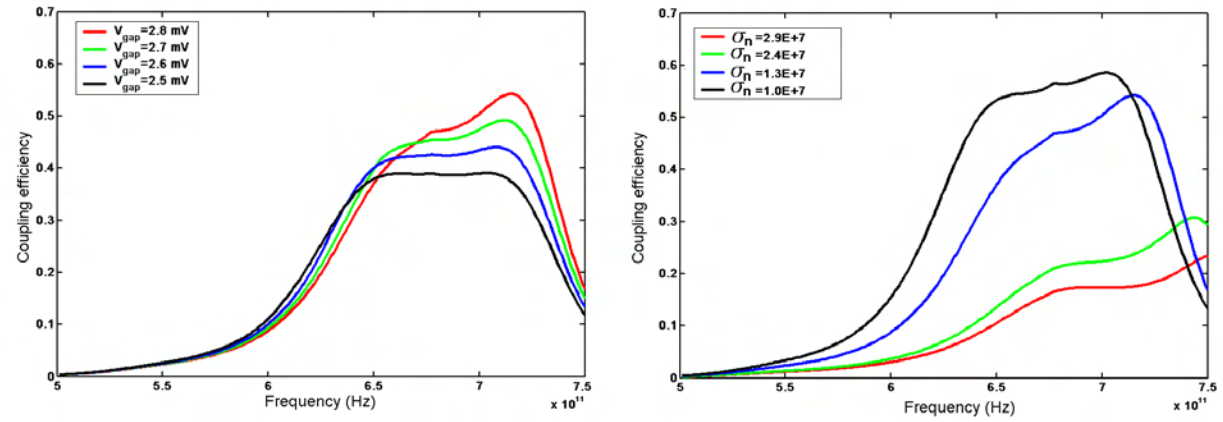

Figure 4.16: Influence on the RF coupling due to: (Left) variations in the superconducting gap energy ($2\Delta = eV_{gap}$) in the top strip of the microstrip lines, assuming for the ground planes a gap of $V_{gap} = 2.8$ mV. (Right) variations in the normal-state conductivity of Nb films.

evaluation of the gradual change in properties of the Nb layers along with transmission electron microscopy (TEM) pictures are given in section 4.7.4.

Another important parameter that has a large influence on the modeling, is the conductivity of Nb films. For the same reasons described above for the variations in the energy gap, the normal-state conductivity σ_n of the film changes gradually. The effect has been shown in figure 4.16(right) for three different normal-state conductivity values. In order to confirm this hypothesis, measurements have been done on Nb layers of different thickness, which will be the next topic.

4.7.4 Nb film quality evaluation

In order to critically evaluate the quality of the Nb films used in the microstrip lines, samples of Nb with different thicknesses were prepared on top of 250 nm of SiO2 which itself was on top

of 200 nm Nb. A Si (111) wafer was used as the substrate. The cross section of the structure is thus exactly the same as the actual microstrip lines used in ALMA band 9 devices. The deposition method used was the same as ALMA devices. Four-point probe Resistance-Temperature curves of these samples were taken to extract values of resistance at 10K and 300K, Tc, and RRR. The data is presented below. The relative error in the presented values of resistivity is less than $\pm 8\%$. In figure 4.17(a) and (b) we clearly see a sharp increase in resistivity and decrease

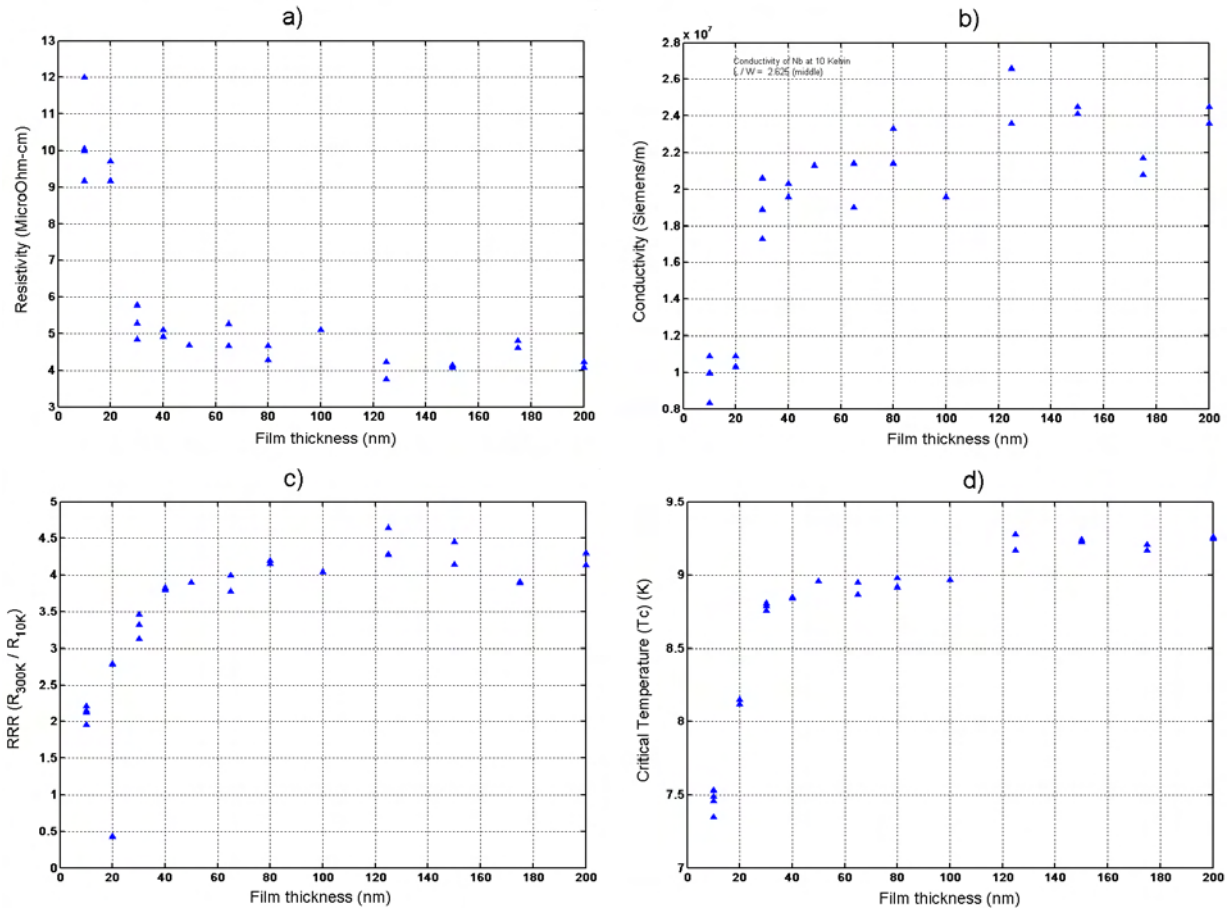

Figure 4.17: Influence on the RF coupling due to: (Left) variations in the superconducting gap energy ($2\Delta = eV_{gap}$) in the top strip of the microstrip lines, assuming for the ground planes a gap of $V_{gap} = 2.8$ mV. (Right) variations in the normal-state conductivity of Nb films.

in conductivity in the films starting at around 30-40 nm. In figure 4.17(c) we see a degradation of the film quality indicated by the residual resistivity ratio (RRR) value. The RRR value is the ratio of the resistivity at 300K to the value at 10K. This a direct indication of the amount of "dirtiness" of the films, since it is inversely proportional to the resistivity caused by processes other than thermal scattering, like impurity scattering. In figure 4.17(d), we see a decrease in T_c which could indicate a decrease in the energy gap Δ, mentioned before. Further evaluation was made by taking transmission electron microscope (TEM) pictures of the sample cross section. This is shown in figure 4.18. In figure 4.18(a), the crystal grains have random orientation caused

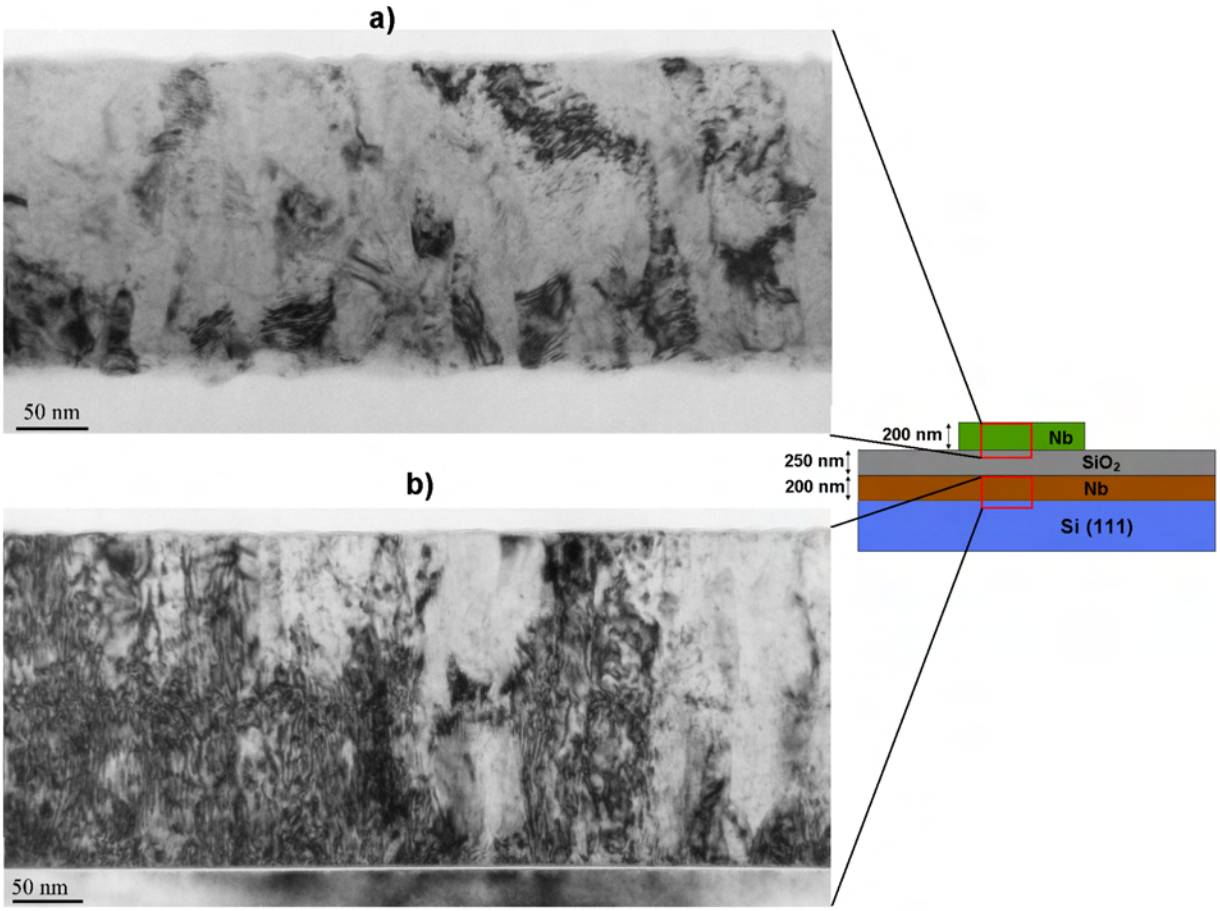

Figure 4.18: Bright-field transmission electron microscope pictures of Nb/SiO2 and Nb/Si cross sections in microstrip lines [77]. (a) A gradual change in Nb crystal structure is observed. The grain size increases as we move to higher positions, indicating better Nb quality. The crystal structure of the grains has random orientation caused by the roughness of the SiO2 layer. (b) There exists columnar crystal structure, probably indicating better Nb quality.

by the roughness of the underlying sputtered SiO2 layer. This was further justified by looking at the diffraction patterns of the crystal (not shown here), indicating random orientation of the grains [77]. Moreover, the grain size increases as we move to higher positions, indicating better crystal structure there. Therefore, we think that the crystal quality as well as the surface roughness of the SiO2 layer, might be a cause for an increase in resistivity when thickness is reduced. Another source that might be responsible for this increase, is the well-known destructive effect of oxygen impurity on Nb superconductivity [76]. We suspect that oxygen can be sucked from the underlying SiO2 layer, since Nb is a very good gettering agent for oxygen. However, this has not been confirmed in our case.

From the resistivity measurements and the TEM pictures, it can be concluded that the DC measured value for conductivity in the Nb film, is an average of the position-dependent conduc-

tivity over the thickness of the film t:

$$\sigma_{DC} = \int_0^t \sigma(t')dt'/t \tag{4.38}$$

Therefore, using this value in the Mattis-Bardeen formula (equations 4.27 and 4.28) will not provide us with the correct complex conductivity, since the assumption there is a constant bulk value for σ. Moreover, an evaluation of an equivalent energy gap (Δ_{eqv}) is also needed, and is as important as the conductivity. A solution to this problem is out of the scope of this work. Therefore, we will assume a gap of 2.8 meV for both conductors, and further use a value for conductivity that fits best to our simulations of the RF coupling, as this is the best we can do for now. This "effective conductivity" will to some extent include the problem of gap variation too. The best value for conductivity that agrees with simulations and measurements of RF coupling, has been found to be $\sigma_n = 1.0 \times 10^7$ S/m.

4.8 Practical modeling considerations

All the effects described in the previous sections, were intrinsic to the devices themselves. However, when we start measuring the RF coupling efficiency, the measurement instruments will interfere with the coupling, and will alter the shape, bandwidth, and absolute value of η_{RF}. In order to be able to compare the simulation results with the measurements, these "outside" effects need to be taken into account. Therefore, we will first briefly look at how the RF coupling measurement is done. Then we will evaluate the effect of the optical elements in the measurement setup, the atmospheric interference, and the variable quantum sensitivity of the SIS junction on the coupling.

4.8.1 RF coupling efficiency measurement technique

Because of the very high working frequency of SIS mixers, the conventional microwave instruments are not able to perform measurements of the frequency response on these devices. Instead, measurement techniques from optics are used. The technique is called Fourier transform spectroscopy (FTS) and is basically a slightly changed Michelson interferometer.
In a Michaelson interferometer, the incoming radiation is split into two beams, and then coherently recombines them to produce the output beam. Interference effects are produced by varying the relative length of optical paths traveled by the separated beams. This path difference is controlled by a moving mirror in one of the beam paths. The output beam intensity is modulated by the path length difference δ. Let's assume the source has a spectrum intensity $S_{in}(\sigma)$ where σ is the wave number (inverse of wavelength λ). Then the output beam spectrum intensity will be equal to

$$S_{out} = S_{in}(\sigma)(1 + cos(2\pi\sigma\delta))\text{const.} \tag{4.39}$$

The total output power will therefore be:

$$I(\delta) = \text{const} \int_0^\infty S_{in}(\sigma)(1 + cos(2\pi\sigma\delta))d\sigma. \tag{4.40}$$

We can find the spectral information of the input beam by taking the inverse Fourier transform of the measured output power:

$$S(\sigma) = \text{const} \int_{-\infty}^{+\infty} [I(\delta) - 1/2I(0)] \exp(-j2\pi\sigma\delta) d\delta. \tag{4.41}$$

where $I(0)$ the maximum output power. The intensity as a function of path difference $I(\delta) - I(0)$ is called an interferogram. The inverse fourier transform of the interferogram is called it's spectrum.
This technique measures the spectrum of the radiation source itself. However, we need the spectral response of our system. In order to use this, we change the source into a constant-intensity source over frequency (perfect black-body), and use our SIS device as the detector. This means that we operate the SIS device in direct detection mode as described in section 2.2.1. In this mode, the change of current is measured in the output. Therefore we can write:

$$\Delta I_{dc}(\omega) = R_i \, \eta_{RF} \, \eta_{opt} \, \eta_{atm} \, P_s. \tag{4.42}$$

where R_i is the junction responsivity, η_{RF} is the RF coupling efficiency, η_{opt} is the optical coupling of all the optics in the system, η_{atm} is the atmospheric coupling (or transmission), and P_s is the source spectrum, which is constant over frequency (delta function in frequency domain). From equation 4.42 it is obvious that by correcting the spectrum for η_{opt}, η_{atm} and R_i, we can obtain the RF coupling efficiency η_{RF}, and thus knowledge about the tuning circuits. These corrections will be made on the simulation results rather than the measurements. The reverse is also possible, but we prefer this way. A typical interferogram using an SIS junction as the detector along with the raw measured spectrum is shown in figure 4.19. Since no absolute calibration is available for the FTS, we cannot extract the absolute value of the RF coupling. But it is very useful for information about the shape and bandwidth of the response.

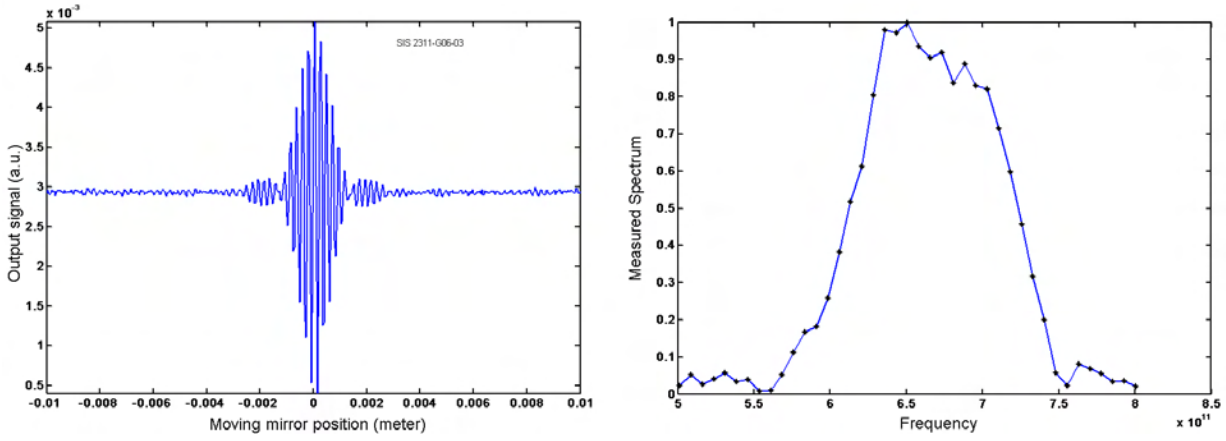

Figure 4.19: (a) A typical interferogram. (b) The frequency response (FTS). The data was obtained for batch SIS2311-G06 of a Nb SIS device.

4.8.2 Correction for optical elements

In order to split the source beam in an FTS measurement system, a beam-splitter is used. The beam-splitter used for our measurements is made of thin 50μm Mylar film that is put in a 45° angle with the incoming source beam. The beam-splitter transmission efficiency is a periodic function of frequency and can be calculated if the index of refraction, the thickness of the film and beam-spitter angle are known. The index of refraction for Mylar has been measured for frequencies between 500-900 GHz [79], and is reported n=1.74. Using this data, the beam-splitter transmission efficiency is calculated and is shown in figure 4.20(left).
The window used in front of the cryostat is a 125 μm Mylar film at 90° angle. There exists also a heat filter made of solid Teflon (PTFE) that has a reported permittivity between 1.95-2.05 [80]. We will use a value of n=2.0. The transmission efficiency of the combination of these three optical elements is shown in figure 4.20(right).

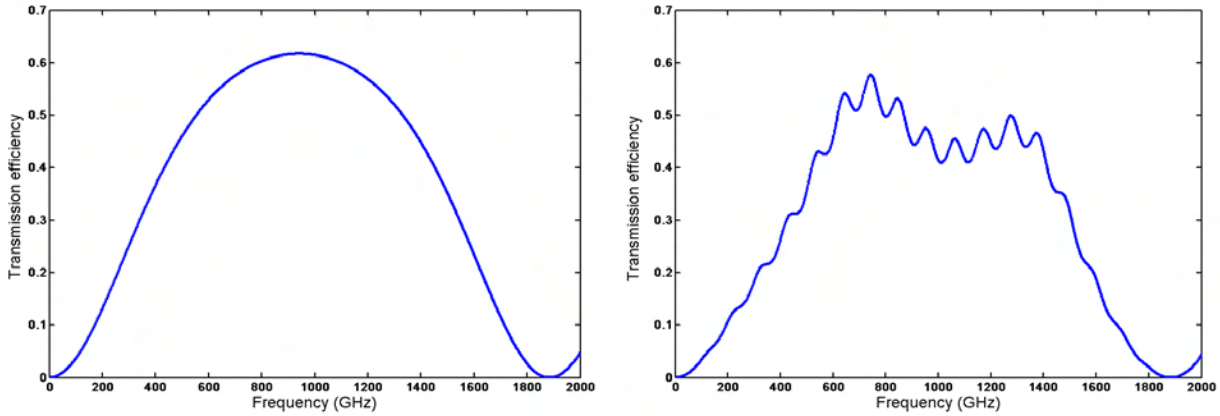

Figure 4.20: (Left) Transmission efficiency for the Mylar beam-splitter used for measurements. (Right) Transmission efficiency for all the important optical elements in the measurement setup (beam-splitter, cryostat window, heat filter).

4.8.3 Atmospheric transmission efficiency

In the FTS measurement setup, the optical beam passes through the laboratory atmosphere. This path length is approximately 1 meter. Previously, in sections 1.1 and 1.1.2, the effect of the earth's atmosphere on submillimeter radiation was discussed. However, those graphs are for the zenith transmission through the 1000 kilometer thick atmosphere. in our measurement, we have only one meter of air path that needs to be taken into account. We made accurate simulations of the atmospheric transmission using the ATM program provided by Dr. Pardo [81]. The transmission efficiency for the typical lab atmosphere (990 mb, 20°C, 40% humidity) is shown in figure 4.21(a).

4.8.4 Frequency dependant responsivity

In section 2.2.1, the responsivity of an ideal SIS junction was shown to have a $1/f$ frequency dependence. For a non-ideal SIS junction, the quantum efficiency $\eta_Q < 1$. The effect is that the responsivity will decrease, but will still have a $1/f$ dependence. The implication is that when measuring an FTS curve for an SIS junction, the spectrum is multiplied by η_Q/f. This can be taken into account in the simulations by multiplying the simulated RF coupling efficiency by $1/f$. Such corrections have been also been reported in [82]. The calculated responsivity for an ideal SIS junction is shown in figure 4.21(b).

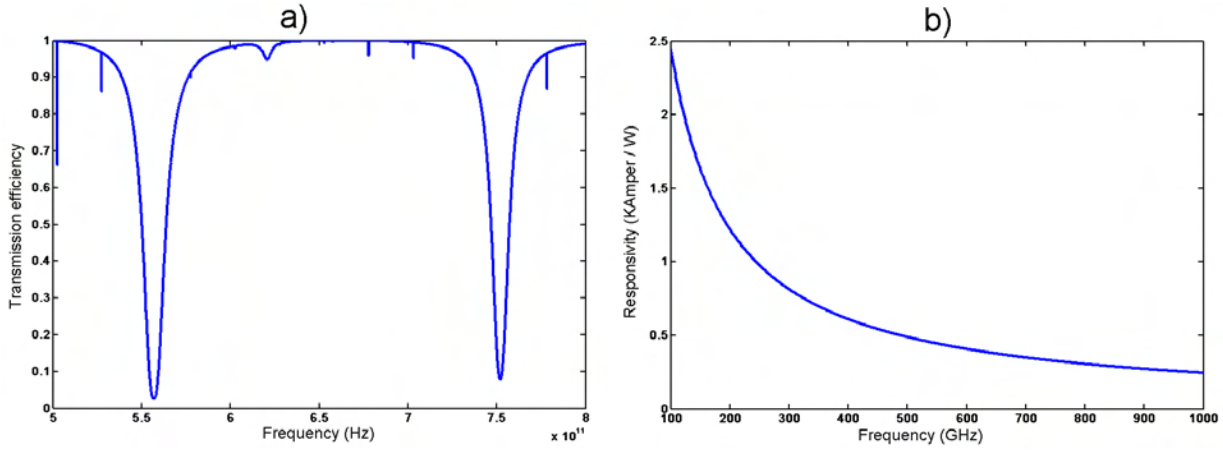

Figure 4.21: (a) Atmospheric transmission for 990 mb, 20°C, and 40% humidity, for 1 meter of optical path length in the lboratory. (b) Calculated responsivity of an ideal SIS junction.

4.9 Final modeling and measurement results for ALMA batch SIS2311 devices

In this section, the simulation results, measured FTS responses, and I-V characteristics for devices from two measured sectors in fabrication batch SIS2311 are presented. The results are summarized in figure 4.22.

The geometries of the tuning circuits used for the devices in figure 4.22 are all of the higher-shifted type. The geometries of 5 sectors are given in table 4.3.

The material properties of the Nb layers as well as the dielectric layer are given in table 4.4.

The value measured by the four-point probe technique for the DC conductivity (σ_n) is for layers of 200nm and 500nm thick. However, as was explained in section 4.7.4, this value is not representative of the correct normal-state conductivity to be used for surface impedance calculations. The $\sigma_{n,eqv}$ value that is used instead, was found by trial and error. Nevertheless, it is close to expected values for lower quality sub-layers of Nb, reducing the equivalent conductivity (section4.7.4).

The properties of the 5 SIS junctions, are listed in table 4.5. From this table, and from figure

Table 4.3: Geometries of the tuning circuits for SIS2311 sectors A,B,C,D, and E.

	Normal	Higher shifted	Lower shifted
$L_1 \times W_1$ (μm^2)	34×6	34×6	34×6
$L_2 \times W_2$ (μm^2)	19.8×56	19.8×56	19.8×56
$L_3 \times W_3$ (μm^2)	5×6.5	5×7.5	5.5×5.5
L_A (μm)	6.6	6.6	6.6
L_B (μm)	6.6	6.6	6.6
t_d (nm) (SiO_2)	250	250	250
t_s (nm) (Nb)	500	500	500
t_g (nm) (Nb)	200	200	200

Table 4.4: Layer material properties for SIS2311 devices.

σ_n (DC) at 10 K	2.4×10^7 S/m
$\sigma_{n,eqv}$ at 10 K	1.0×10^7 S/m
V_g at 4.2 K	2.8 mV
ϵ_r (SiO2)	3.8
T_c	9.25 K

Table 4.5: SIS junction properties for selected SIS2311 devices.

Device	2311A24	2311A28	2311A39	2311B29	2311B38
R_n (Ω)	23.6	23.8	23.8	22.7	22.8
C_s (fF/μm^2)	80	80	80	80	80
R_nA ($\Omega\mu$m^2)	24.5	24.5	24.5	24.5	24.5
A (μm^2)	1.04	1.03	1.03	1.08	1.07
$C_j(fF)$	83.2	82.1	82.8	86.3	86.0
$V_g(mV)$	2.8	2.8	2.8	2.8	2.8

4.22(f), we can conclude that the repeatability in SIS junction properties is high. Results in table 4.4 also show that similarity in tuning circuit material parameters is excellent. However, figure 4.22(e) shows that despite these similarities, the RF coupling (FTS responses) is varying over a range of approximately 30 GHz over the bandwidth. This variation is too high to be attributed to errors caused by fabrication tolerances, as simulations also show that changes in for example C_j (which is the most probable fabrication error), cannot compensate for the shifts seen. Moreover, fabrication errors tend be be uniform across the wafer, while the variations seen in the FTS measurements are scattering randomly. These results indicate that the mounting accuracy of the

devices, and the substrate thickness accuracy, are the most prominent factors that cause the scattering in the measured RF coupling efficiencies.

The implication of the scattering in the measured responses, is that it would be very difficult to fabricate devices which cover the full bandwidth. This has been indicated in figure 4.22(e) by the full-width half-maximum (FWHM) line. We see that the response at lower frequencies is not covering the bandwidth. Only device SIS2311-B29 is close to doing this. The effect of this insufficient coupling becomes apparent in the measured noise temperature. The noise temperature of four devices is shown in figure 4.23. A direct relation between the higher noise and lower RF coupling efficiency at lower frequencies is observed.

Despite all this said, the accuracy of the RF coupling efficiency simulations are higher than expected, which is a justification for the modeling technique and formulae used. Further increase in predictive modeling accuracy requires that all the variations - at least the major ones - be eliminated before further progress can be made. Otherwise, predictive modeling, more than what is presented, would not make much sense. However, there is still an important conclusion that can be made by looking at the acquired bandwidth in figure 4.22(e) with the current design: despite the scattering, optimization of the tuning structure dimensions can be done in order to get the response centered across the desired bandwidth. Higher possible bandwidth and an increase in the absolute value of coupling might also be possible by optimization. This is the subject of the next chapter.

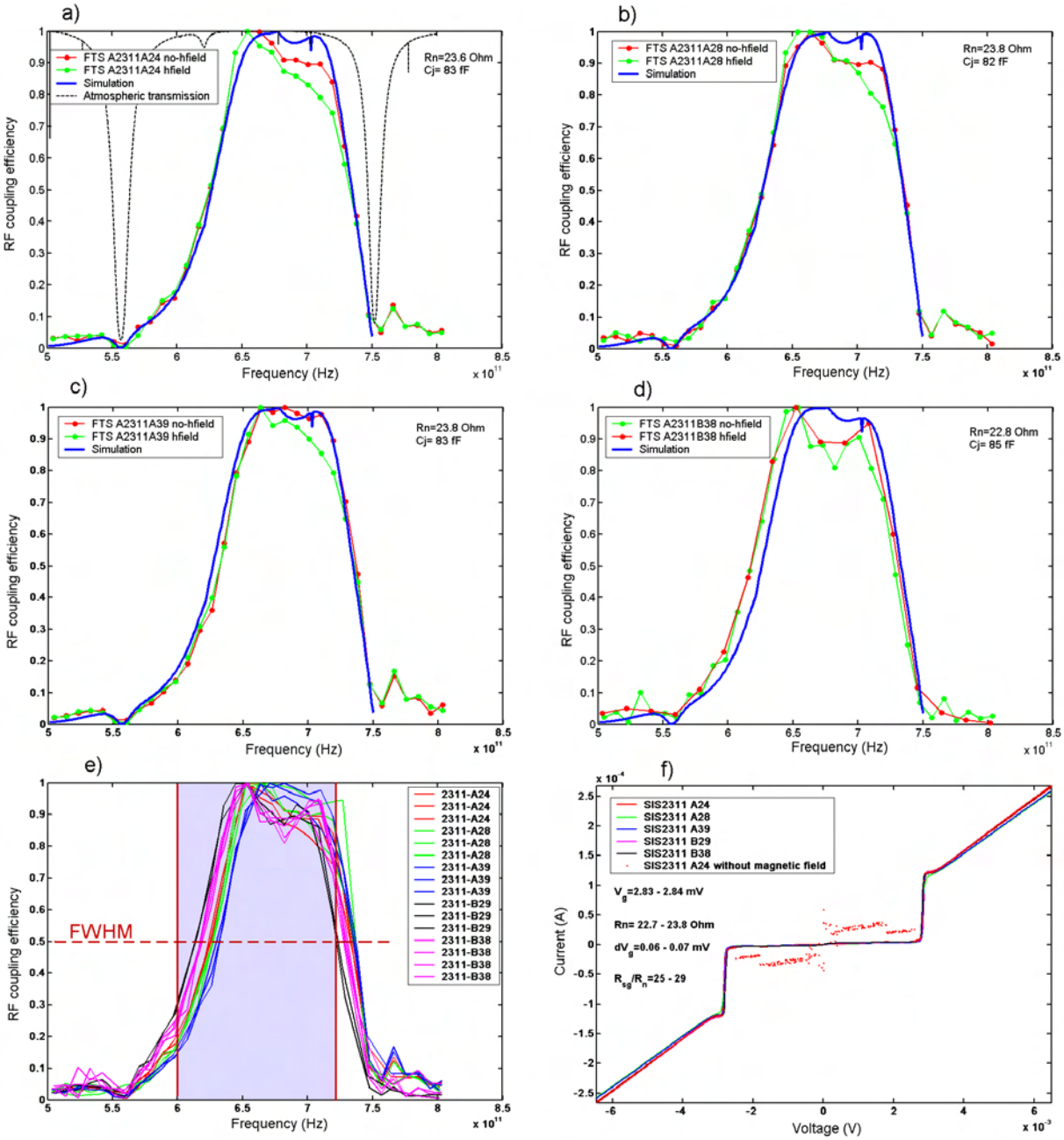

Figure 4.22: (a),(b),(c), and (d) show simulation results for the RF coupling efficiency performed using the modified model (Yassin's model) described in section 4.3.1 and the modification explained in section 4.8. The parameters used are from tables 4.3, 4.4, and 4.5. Figure (a) also includes the atmospheric transmission efficiency in black dotted lines. The measured FTS results are indicated for two cases: in green, when magnetic field is applied to suppress the Josephson curent, and in red when it is not applied. Figure (e) shows all the measured FTS results for five nominally identical devices. The shaded area shows the required bandwidth, and the full width half maximum line is indicated. Figure (f) shows the I-V characteristics for the five devices, with a summary of the important properties. The dotted curve is for when magnetic field is not applied.

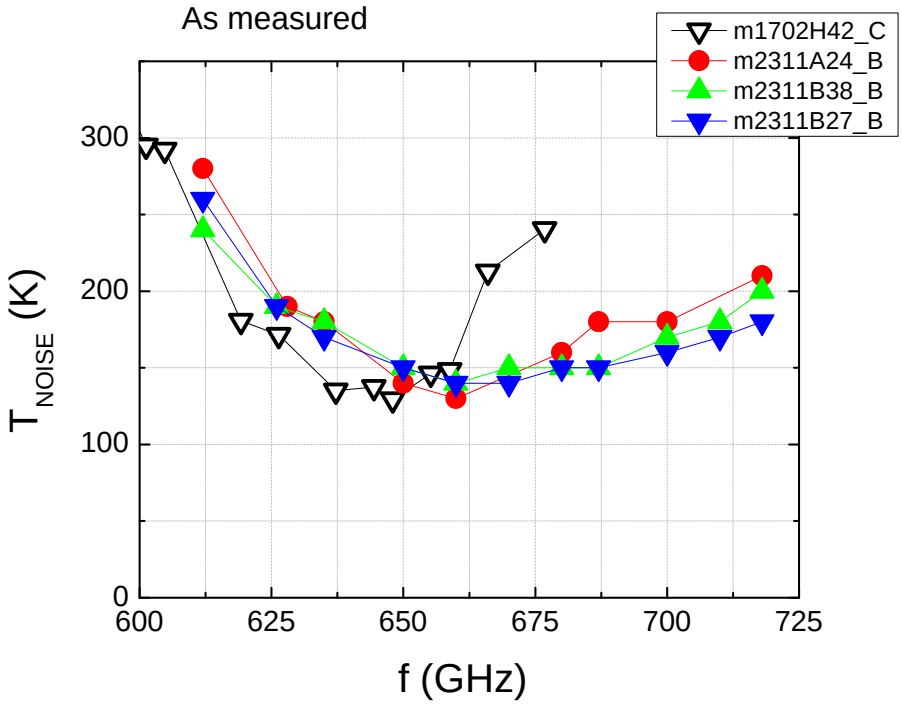

Figure 4.23: Noise measurement results for three devices from batch SIS2311, and one an older design. We see a sharp increase at lower frequencies in noise, which corresponds to lower RF coupling efficiencies. The results are not corrected for added noise due to other elements in the mixer.

Chapter 5
Optimization of SIS mixer RF coupling efficiency and bandwidth

5.1 Optimization requirements

In the design of the SIS mixers discussed in this thesis, the RF tuning circuits were used to couple the radiation efficiently to the SIS junction. In order have efficiency and sensitivity in the mixers, three important factors exist that need to be optimized: the input noise temperature of the receiver, the RF coupling bandwidth of the receiver, and the output IF bandwidth. The optimization of the noise temperature, translates (partly) into finding the maximum value for the RF coupling efficiency in the detection band. The higher the coupling, the lower the losses, the lower the equivalent input noise. The optimization of the RF bandwidth of the receiver, translates (partly) into optimization of the RF bandwidth of the tuning circuits. The optimization of the output IF bandwidth, translates into optimizing the coupling efficiency between the IF amplifier and the output IF impedance of the SIS mixer. The first two optimizations have been done in this work (RF bandwidth and RF coupling efficiency).

In order to perform these optimizations, a two-dimensional function has to be optimized: $\vec{f} = [f_1(x_1, \ldots, x_n)\ , f_2(x_1, \ldots, x_n)]$, where f_1 is the RF bandwidth and f_2 is the RF coupling efficiency. Figure 5.1 shows the two functions f_1 and f_2. They are functions of many material and geometrical parameters like the thicknesses of the Nb and SiO2 layers, and the lateral dimensions of the microstrip lines, and the dimensions of the waveguide and probe point. Most of these parameters were discussed in the previous chapters, and their effect on the behavior of RF coupling efficiency was modeled. However, we will only use the tuning circuit geometry for optimization, as it is the easiest and most accessible way.

In our tuning circuit designs, we have eight dimensions to optimize: L_1, L_2, L_3, W_1, W_2, W_3, L_A, and L_B . These are shown in figure 4.11. We can choose to put $L_A = L_B = 0$, which reduces the dimensions to six. These eight parameters produce a huge eight dimensional search space which can easily get out of control. Measures have to be taken for this, like searching in

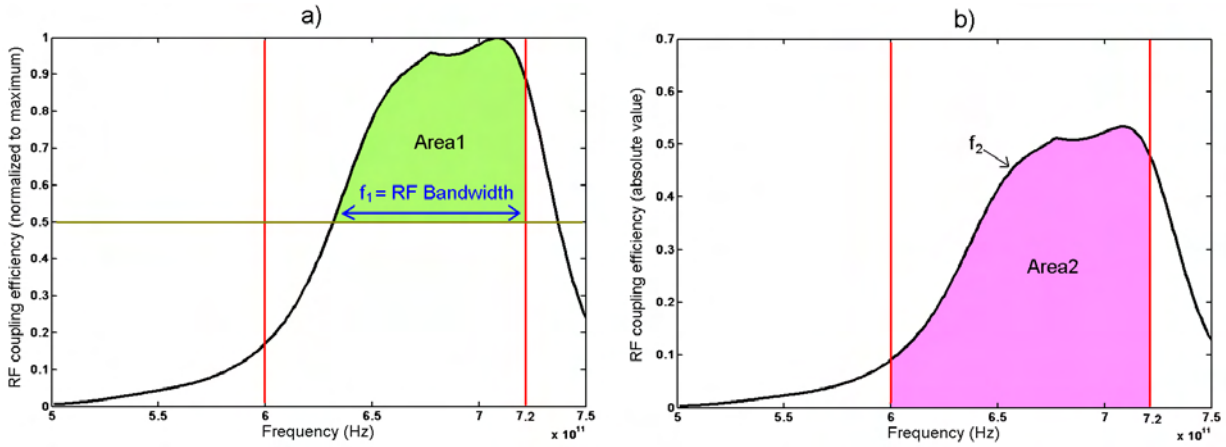

Figure 5.1: The two functions f_1=RF bandwidth, and f_2=RF coupling efficiency, which need to be optimized.

discrete steps. This will be described in section 5.2.1.

5.1.1 Optimization criteria

In order to optimize a function, some criteria have to be defined which can access the optimization results. We will define these criteria as follows.
In figure 5.1(a), the RF coupling efficiency has been normalized to its maximum value. We can define the criteria to optimize the bandwidth, as the area under the curve (area1), and above 50% relative coupling, between 600 to 720 GHz. By changing the parameters to obtain a maximum for area_1, we optimize the bandwidth. In this process, the absolute value of the coupling efficiency is also likely to be optimized to some extent; however, less than the bandwidth.
In figure 5.1(b), the absolute value of coupling has been shown. We can define the criteria to optimize the coupling efficiency, as the area (area2) under the curve, between 600 to 720 GHz. In this process, the bandwidth is also likely to become optimized; however, less than the coupling.

In the ideal case, for optimizing both bandwidth and coupling, we have to maximize both area1 and area2. However, because of the practical difficulty and extensive time required to do so, we have chosen to maximize area2. In this process, we will also have an eye on the value of f_1, meaning that we fine-tune for that manually.

Now that we have a function to maximize (area2), we are faced with the classical problem of finding the absolute maximum of a given function over an allowed range, that is, practical and non-negative dimensions. In the most general case, this problem does not have a straight forward and fast solution other than checking the function over the whole range. This is especially true for complicated, non-analytical functions. This method, named the 'brute search technique', will be used in section 5.2.1.
Another method, is to find the local maxima of the function, and then choose the absolute maxi-

mum out of them. Fortunately, the problem of finding local maxima in a given range is possible by using specific mathematical search algorithms. This method, named the 'smart search technique', will be used in section 5.2.2.

5.2 Optimization techniques

5.2.1 Brute search optimization technique

In this technique, the six or eight dimensional space of the tuning circuit geometrical parameters is searched for finding the maximum area under the coupling efficiency curves. Let's assume that we are limited to a certain search space. We divide the search space for the n^{th} length or width into a_n steps. This will create a space of $\prod_{n=1}^{8} a_n$ elements, in each of which the function has to be evaluated. After all these function evaluations, we can find the maximum value by a normal maximum search in the generated set of values.
As an example, in figure 5.2, a search in a space as big as $9 \times 6 \times 10 \times 10 \times 10 \times 12 = 648000$ elements has been performed, using a computer program written in MATLAB. The gray and green areas are the 648000 RF coupling efficiency curves calculated and plotted. The green area is the maximum value of all the 648000 areas calculated. This maximum value can also be regarded as the maximum average coupling efficiency if we divide the integral by the integration range (120GHz). But we will just regard it as the maximum area. The corresponding coupling efficiency is indicated in blue, which is the optimum curve. The corresponding geometry for the optimum tuning circuit is shown on the left side of the figure, and the search space is shown on the right hand side [1]. This search took approximately 3 days with a 64 bit AMD processor and 512 MB of RAM. The large amount of time and computer sources needed, is a disadvantage of this technique compared to the smart search presented in the next section.

It should be noted that for the purpose of optimization, the destructive effect of laboratory atmospheric absorbtion has not been included in the simulations. This is because the designed mixer is supposed to work at the high altitude of the Atacama desert in Chili, where the atmosphere is very clear. However, for best results, it would have been better to include the atmospheric effects of that specific altitude in the simulations. Unfortunately, the required program for simulating the atmosphere was not available at the time of these optimizations. Nevertheless, we believe these results should be close to those using the atmospheric transmission for simulations.

An important observation that can be made from figure 5.2(a), is the upper limit set on the RF coupling efficiency. This quite sharp decrease in coupling starts from $\sim$ 680 GHz, and corresponds to the gap frequency of Nb. It indicates the start of increase in surface impedance of the microstrip lines which limits the performance. No matter what geometry used, this limit always exists for the current materials used. However, if another material like NiTiN for the microstrip lines, or AlN for the junction barrier is used, this limit will be moved to higher frequencies.

[1] The two lengths L_A and L_B were set to zero to reduce the computational load.

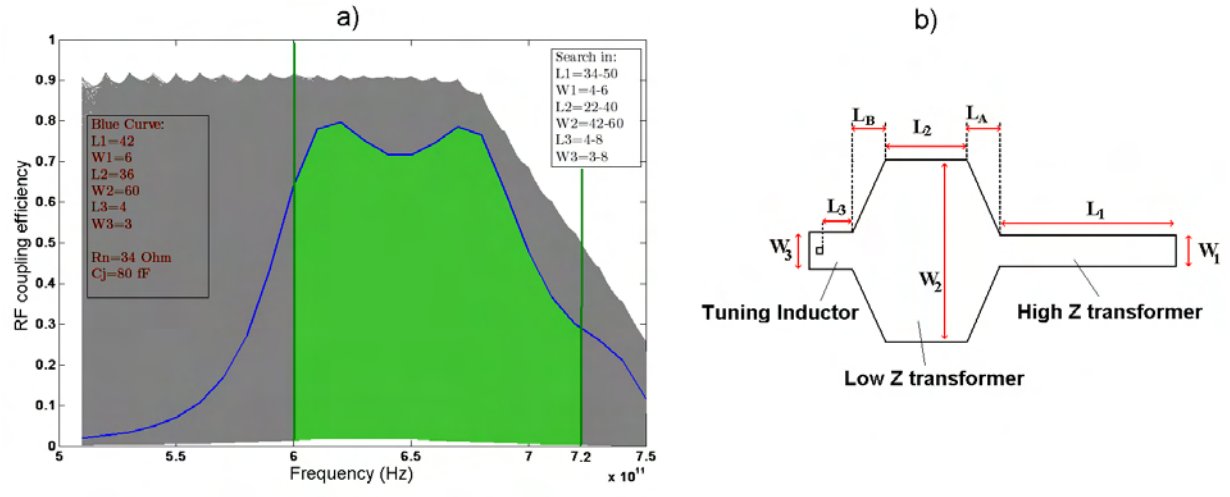

Figure 5.2: (a) The 'brute search technique' for finding the maximum area under the RF coupling efficiency curve between 600 and 720 GHz. The parameter space searched, is indicated on the right side of the curve. The maximum area found is indicated in green. The corresponding RF coupling curve is shown in blue, which is the optimized RF coupling in the sense of maximum average coupling and bandwidth. The corresponding geometry for the tuning circuits is shown on the left of the curve in micrometers. (b) The eight tuning circuit dimensions used for optimizing the coupling efficiency and bandwidth.

NiTiN has a larger gap frequency ($\sim$ 1200 GHz) than Nb, meaning that surface impedance will not increase sharply before that. AlN barriers, as was shown in section 2.3.2, have lower RC constants, causing smaller slope in the higher frequency limit line. This will be shown in section 5.3.

5.2.2 Smart search optimization technique

The smarter way to find the absolute maximum of a function compared to the brute search method, is to find as many local maxima as possible, and choose the maximum out of these values. many different mathematical algorithms exist that can do this. Most of them are designed for specific types of functions which satisfy certain conditions like slow variation over the search range or a limit to the number of variables. However, since we do not know how our eight dimensional function behaves, we chose the most general method called the 'Nelder-Mead simplex algorithm' [83]. This search method has already been integrated in MATLAB, which is the program used for searching. Extra features needed to be added to this MATLAB version of the method, in order to bound the search to positive values. Figure 5.3 shows the result of search with the Nelder-Mead simplex method. The optimization results are for two kinds of design, namely the tapered and the non-tapered (section 4.6). The result curve from the brute search method (section 5.2.1) is also shown for comparison. Two curves for the previously not optimized designs are also presented for comparison. The time required to optimize using the smart

search technique is about 5-10 minutes, which is obviously much better than the brute search technique.

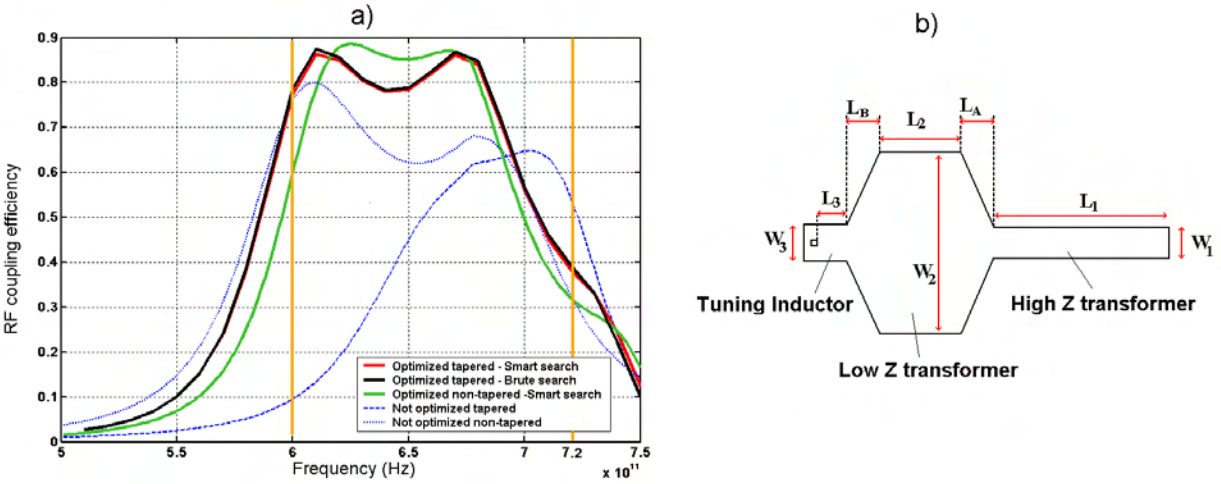

Figure 5.3: (a) Results for the smart search technique for two kinds of geometry - tapered and non-tapered - are shown in red and green respectively. The brute search result for tapered design is drawn in black. Two previous not optimized tapered and non-tapered designs are shown in blue. (b) The eight tuning circuit dimensions used for optimizing the coupling efficiency and bandwidth.

From picture 5.3, several conclusions can be made. First, we see that the result from the brute search and smart search techniques are almost exactly matching. This verifies the techniques used. Secondly, for the optimized tapered design, we observe a (useful) bandwidth of $\sim$ 110 GHz while for the not optimized tapered design it is $\sim$ 80 GHz. This is an increase of about $\sim$ 37% in bandwidth. An increase in coupling as much as 30% is seen as well. For the optimized non-tapered design, a bandwidth of $\sim$ 100 GHz is seen, while in the not optimzed version it was $\sim$ 105 GHz. This is a decrease of $\sim$ 5%. But as a tradeoff, an increase in coupling is seen as much as $\sim$ 40% at its highest. It can be concluded that the tapered design is potentially more capable of providing bandwidth, while keeping the coupling at high values. Therefore, it would be the best choice for tuning circuit designs. Adding more transformers to the tuning circuit proved to be useless in increasing either bandwidth or coupling. This was tested by the same techniques that were presented here.

5.3 Optimization using lower R_nC_j product SIS junctions

Up to here, all designs were made for Nb/AlOx/Nb SIS junctions which have critical current densities around 10 KA/cm^2 (table 4.1). This resulted in an (useful) RF bandwidth of around 100-110 GHz (figure5.3) which seems to be the upper limit for ALMA band 9 using Nb/AlOx/Nb

junctions. It turned out to be quite difficult to cope with this bandwidth, since the required bandwidth for ALMA band 9 is 120 GHz. Moreover, the errors existent in different parameters, most importantly the mounting inaccuracy and junction area inaccuracy, tend to change the optimized tuning circuits behavior which were designed assuming certain parameters. Slight amounts of such inaccuracies result in shifting of the response to out side the required bandwidth, and therefore insufficient coupling bandwidth as was seen in figure 4.22(e).

One of the ways to overcome this bandwidth problem, is to use another material for the SIS junction. For this purpose, Nb/AlN/Nb junctions seem to be the best candidate because of their higher current densities resulting in lower RC products. In parallel with this thesis work, Nb/AlN/Nb junctions were fabricated and tested by the people in our group, and it proved to be possible to use this new technology. Current densities for Nb/AlN/Nb devices were reported around 38 KA/cm^2, which is $\sim$ 4 times larger than our Nb/AlOx/Nb junctions. The result is $\sim$ 4 times lower R_nC_j products, which will lead to higher achievable RF bandwidths which can reach up to 300 GHz [57]. We have tried to find optimum tuning structure dimensions assuming $R_nA = 6.25\Omega\mu m^2$, $C_s = 100fF/\mu m^2$, and $R_n = 25\Omega$ with our programs. The optimization result is shown in figure 5.4. It can readily be seen that the Nb/AlN/Nb junctions are providing

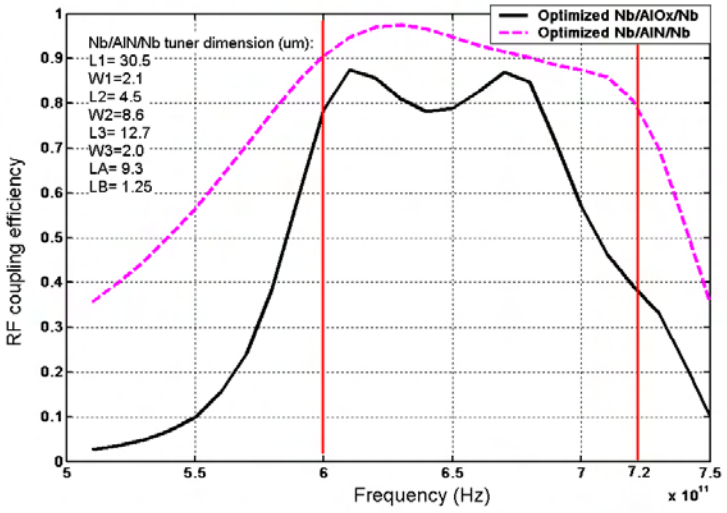

Figure 5.4: Comparison between optimized Nb/AlOx/Nb and Nb/AlN/Nb SIS junctions. The RF coupling efficiency total bandwidth for AlN is $\sim$ 200 GHz of which $\sim$ 150 GHz is useful. For the Nb/AlOx/Nb device the total bandwidth is $\sim$ 150 GHz of which $\sim$ 100 GHz is useful. The required bandwidth for ALMA band 9 is indicated and is 120 GHz.

$\sim$ 50 GHz more bandwidth than their Nb/AlOx/Nb counterparts. This will almost entirely solve the problem of insufficient bandwidth caused by uncontrollable errors, because all the inaccuracy will be absorbed in the large bandwidth, still yielding the required 120 GHz bandwidth in the 600-720 GHz range.

Chapter 6
Summary and conclusions

6.1 Summary

The goal of this thesis research was to extend the low-noise performance of Nb/AlOx/Nb Superconductor - Insulator - Superconductor (SIS) mixers to frequencies above the Nb gap frequency (680 GHz) for use in the ALMA band 9 range (600-720 GHz). First, an insight into the quantum mechanical backgrounds enabling low noise mixing has been presented. Low noise performance of the mixers depends on several factors, some of which have been evaluated in this work. One of them is the materials quality and engineering of the SIS junction. Sharp I-V characteristics with low leakage currents and high gap voltages are required to achieve low intrinsic mixer noise and reasonable mixer conversion losses, or even gains. Mixer performance degradation causes and high frequency limitations of SIS junctions have been studied, and an effective way to suppress the Josephson supercurrent which introduces noise has been established. The material choice for our SIS junctions have been evaluated and its usage justified.

However, the core of this work was to improve and optimize the coupling of radiation into the small SIS junctions, as well as improvement in modeling the RF coupling behavior. Waveguide technology is used to direct and couple the radiation to the device. However, because of the high reliability standards needed for the ALMA telescopes, tunable elements like backshorts are no choice for tuning the coupling. Instead, integrated tuning circuits have been used in order to increase the RF bandwidth and coupling efficiency. These circuits are made of Nb superconducting microstrip lines that operate around and even above the Nb superconducting gap frequency ($\sim$ 680 GHz). Work above this frequency will introduce significant RF losses in the microstrip lines that have to be taken into account. Only then the characteristics of the microstrip lines can be calculated and RF behavior of the tuning circuit predicted. For this purpose, the Mattis-Bardeen theory of anomalous skin effect [72] has been used to calculate the surface impedance of the lines. Further, an mofification in modeling microstrip lines has been introduced (section4.3.1) by taking into account non-uniform current density. In order to simulate the RF coupling, a computer program has been written that utilizes two-port network theory. With this program, aimed for predictive modeling, the effect of materials as well as geometrical variations in the RF response

has been simulated. Measurements of RF coupling efficiency showes scattering in bandwidth for nominally identical devices as large as 30 GHz, which makes the limited 100-110 GHz bandwidth too sensitive to variations. It has been found that fabrication variations are too small to account for this scattering. Accuracy in mounting of the devices into the waveguide and accuracy in device thickness reduction have been found to be the most prominent variations responsible for this scattering. Furthermore, a critical evaluation of the Nb film quality in the microstrip lines has been performed, suggesting that DC resistivity changes over the film thickness, causing uncertainty in the value of σ_n ranging from 0.9 to 2.4×10^7 S/m. The value corresponding to best fit between simulations and measurements (1×10^7) has been taken, although further evaluation is needed. The RF coupling measurement principle was introduced. Various corrections in modeling caused by non-idealities of the measurement instruments and technique have been studied. Using these corrections, measurements of a set of fabricated devices has been compared with the model. It has been shown that despite scattering in measurement results for nominally identical devices, predictive modeling is fairly possible depending on the accuracy of input parameters. Using this model, the tuning circuit geometry has been optimized using various techniques, in order to yield the required bandwidth and highest possible coupling required for ALMA band 9. At the end, RF performance using Nb/AlN/Nb junctions has been briefly evaluated, and it was found that $\sim$ 50 GHz increase in bandwidth compared to the initial Nb/AlOx/Nb junctions is attainable, providing much less sensitivity to uncontrollable variations.

6.2 Remarks

Several important remarks can be made regarding the results obtained.
Low noise Mixer performance using Nb tuning circuits and Nb/AlOx/Nb junctions at frequencies higher than the superconducting gap is limited by both the Nb microstrip line losses and the junction barrier material RC constant. This higher limit was clearly observed in figure 5.2(a). Therefore, in order to have wider bandwidth coupling, we need to change the wiring technology to higher gap superconductors like NbTiN or metals like Al, or change the junction barrier material which has higher current densities resulting in lower RC constants.
Regarding the specific capacitance of Nb/AlOx/Nb junctions, more accurate measurements need to be performed to be able to extract junction capacitances correctly, as this has always been a point of uncertainty. In this work, it was assumed that $C_s = 80 \pm 5fF/\mu m^2$. However, values as high as $85 \pm 5fF/\mu m^2$ have been reported [84, 82].
Concerning the value used for conductivity used for our simulations, ($\sigma_{eqv} = 1 \times 10^7$ S/m), further insight into the Nb layer properties deposited need to be obtained. Although the transmission electron microscopy pictures shown in figure 4.18 were an indication of the gradual change in σ_{DC} over the thickness, we were not able to conclude firmly that 1×10^7 S/m is the actual value. The used value here has been based on an estimate that agrees most with measurements of coupling efficiency.
The mounting and substrate thickness inaccuracy (section 4.7.2), need to be exactly measured for the devices for which modeling is to be performed. This has been shown to be the most

prominent effect in scattering of nominally identical devices. Inaccuracies during fabrication, will not cause scattering in devices made from one batch, and tend produce a systematic error that can be filtered out by inspection and measurements.
Finally, the amount of details that is incorporated in the modeling, and our level of understanding of the effects involved, have exceeded the initial expectation of the complexities involved. During this process, a wealth of information, especially regarding the microwave engineering techniques and different microwave simulation programs have been added to our knowledge which has lead to an increase in our evaluation capabilities.

In conclusion, we have fairly successfully modeled the RF behavior of the tuning circuits to the extent that unpredictable scattering in nominally identical devices allowed us. However, it is has been difficult to correctly simulate the behavior of our devices, because of the many number of uncertainties involved. Nevertheless, optimized tuning circuit dimensions for higher coupling and bandwidth were found and fabricated. Measurement of the optimized devices still needs to be performed in order to give us feed back of the work. This feedback is crucial for better understanding and determination of uncertainties in parameters.

Bibliography

[1] Thomas G. Phillips, and Jocelyn Keene, "Submillimeter Astronomy", Proc. IEEE Vol. 80, p.1662, 1992.

[2] "Sumillimeter Astronomy", Flyer from 'Max Planck Institut fuer Radioastronomie', Bonn, 2005.

[3] Peter H. Siegel, "Terahertz Technology", IEEE Transactions on Microwave Theory and Techniques Vol. 50, pp. 910-928, 2002.

[4] D. Leisawitz et al., "Scientific motivation and technology requirements for the SPIRIT and SPECS far-infrared/submillimeter space interferometers", Proc. SPIE, vol. 4013, Munich, Germany, Mar. 2931, pp. 3646, 2000.

[5] J.R. Pardo, E. Serabyn , and J. Cernicharo, "Submillimeter atmospheric transmission measurements on Mauna Kea during extremely dry El Nino conditions: implications for broadband opacity contributions", Journal of Quantitative Spectroscopy and Radiative Transfer Vol. 68, pp. 419-433, 2001.

[6] W. A. Traub and M. T. Slier, "Theoretical atmospheric transmission in the mid- and far-infrared at four altitudes", Appl. Optics., Vol. 15, pp. 364-377, 1976.

[7] Schilke P, Groesbeck TD, Blake GA, Phillips TG. "A line survey of Orion KL from 325 to 360 GHz", Astrophys J Suppl Ser., Vol. 108, p. 301 ,1997.

[8] Thorwirth S., "Molecules in Space", available online at: http://www.ph1.uni-koeln.de/vorhersagen/molecules/main_molecules.html, 2006.

[9] Submillimeter Array website, available at: http://sma-www.cfa.harvard.edu/sciDoc/m5104.html.

[10] "ALMA Scientific Specifications and Requirements", 2004, available at the ALMA website: http://www.eso.org/projects/alma/science

[11] E. J. Nichols and J. D. Tear, "Joining the infrared and electric wave spectra", Astrophys. J., vol. 61, pp. 1737, 1925.

[12] J. C. Wiltse, “History of millimeter and submillimeter waves”, IEEE Trans. Microwave Theory Tech., vol. MTT-32, pp. 11181127, Sept. 1984.

[13] P. Coleman, “State of the art: Background and recent developments Millimeter and submillimeter waves”, IEEE Trans. Microwave Theory Tech., vol. 11, pp. 271288, Sept. 1963.

[14] P. D. Coleman and R. C. Becker, “Present state of the millimeter wave generation and technique art1958”, IEEE Trans. Microwave Theory Tech., vol. 7, pp. 4261, Jan. 1959.

[15] J. C.Webber and M.W. Pospieszalski, “Microwave instrumentation for radio astronomy”, IEEE Trans. Microwave Theory Tech., vol. 50, pp. 986995, Mar. 2002.

[16] M. C. Gaidis, H. M. Pickett, C. D. Smith, R. P. Smith, S. C. Martin, and P. H. Siegel, “A 2.5 THz receiver front-end for spaceborne applications”, IEEE Trans. Microwave Theory Tech., vol. 48, pp. 733739, Apr. 2000.

[17] E. Kollberg, *Microwave and Millimeter-Wave Mixers*, New York: IEEE Press, 1984.

[18] S. A. Maas, *Microwave Mixers*, Norwood, MA: Artech House, 1993.

[19] T. G. Blaney, “Radiation detection at submillimeter wavelengths”, J. Phys. E, Sci. Instrum., vol. 11, pp. 856881, Sept. 1978.

[20] B. J. Clifton, “Schottky diode receivers for operation in the 1001000 GHz region”, Radio Electron. Eng., vol. 49, no. 7/8, pp. 333346, July/Aug. , 1979.

[21] P. L. Richards, “The Josephson junction as a detector of microwave and far infrared radiation”, Semiconductors and Semimetals, R. K. Willardson and A. C. Beer, Eds. New York: Academic, vol. 12, pp. 395439, 1977.

[22] M. McColl, M. F. Millea, and A. H. Silver, “The superconductorsemiconductor Schottky barrier diode detector”, Appl. Phys. Lett., vol. 23, pp. 263264, Sept. 1973.

[23] T. G. Phillips and K. B. Jefferts, “A low temperature bolometer heterodyne receiver for millimeter wave astronomy”, Rev. Sci. Instrum., vol. 44, pp. 10091014, 1973.

[24] A. H. Dayem and R. J. Martin, “Quantum interaction of microwave radiation with tunneling between superconductors”, Phys. Rev. Lett., vol. 8, pp. 246248, 1962.

[25] P. Tien and J. Gordon “Multiphoton Process observed in the Interaction of Microwave Fields with the Tunneling Between Superconductor Films.”, Phys. Rev. Vol. 129, pp. 647-651, 1963.

[26] J. R. Tucker, “Quantum limited detection in tunnel junction mixers”, IEEE J. Quantum Electron., vol. QE-15, pp. 12341258, Nov. 1979.

[27] R. H. Dicke, “The Measurement of Thermal Radiation at Microwave Frequencies”, Rev. Sci. Instrum., Vol 17, pp. 268-275, 1946.

[28] M.J. wengler, “Submillimeter wave detection with superconducting tunnel diodes”, Proc. IEEE, Vol 80 (11), pp. 1811-1826, 1992.

[29] M.J. wengler and D.P. Woody, “Quantum Noise in heterodyne detectin”, IEEE J. Quantum Electronics, Vol 23, pp. 613-622, 1987.

[30] A. Karpov, D. Miller, F. Rice, J. Zmuidzinas, J. A. Stern, B. Bumble, and H. G. Leduc, “Lownoise 1.2 THz SIS receiver”, in 8th Int. Superconduct. Electron. Conf., Osaka, Japan, June 1922, 2001, pp. 521522.

[31] L.N. Cooper, “Bound Electron Pairs in a Degenerate Fermi Gas”, Phys. Rev., vol. 104, pp. 1189-1190, 1956.

[32] J. Bardeen, L. N. Cooper, and J. R. Schrieffer, “Theory of Superconductivity”, Phys. Rev. 108 (5), p. 1175 (1957).

[33] M. Tinkham, *Introduction to Superconductivity*, 2nd ed., MacGraw-Hill, Inc., New York, 1996.

[34] D.W. Face, D.E. Prober, W.R. McGrath, and P.L. Richards, “High quality tantalum superconducting tunnel junctions for microwave mixing in the quantum limit”, Appl. Phys. Lett., vol 48, pp. 1098-1100, 1986.

[35] H.C. Torry, C.A. Whitmer, *Crystal Rectifiers*, MTT Radiation Lab. Series, Vol 15, McGraw-Hill, NewYork, 1948.

[36] W.R. McGrath, P.L. Richards, A.D. Smith, H. van Kempen, R.A. Batchelor, D.E. Prober, and P. Santhaman, Appl. Phys. Lett. Vol 39, p. 655, 1981.

[37] Terry. P. Orlando, Kevin A. Delin, *Foundations of Applied Superconductivity*, Addison-Wesely Publishing Comp., 1991.

[38] Antonio Barone and Gianfranco Paterno, *Physics and Applications of the Josephson Effect*, John Wiley & Sons, 1982

[39] Dolan, G.J.; Linke, R.A.; Sollner, T.C.L.G.; Woody, D.P.; Phillips, T.G., “Superconducting Tunnel Junctions As Mixers at 115 Ghz”, IEEE Trans. Microwave Theory Tech., vol. 29, pp. 87-91, Apr. 1981.

[40] S. Shapiro, “Josephson Currents in Superconducting Tunneling: The Effect of Microwaves and Other Observations”, Phys. Rev. Lett., Vol 11, pp. 80-82, 1963.

[41] D. D. Coon and M. D. Fiske, “Josephson ac and Step Structure in the Supercurrent Tunneling Characteristic”, Phys. Rev., Vol. 138, A744A746, 1965.

[42] N. N. Iosad, M. Kroug, T. Zijlstra, A. B. Ermakov, B. D. Jackson, M. Zuiddam, F. E. Meijer, and T. M. Klapwijk, "Analysis of the Fabrication Process of Nb/Al-AlNx/Nb Tunnel Junctions With Low RnA Values for SIS Mixers", IEEE Trans. on Applied Superconductivity, Vol. 13 (2), 2003.

[43] Zhen Wang, Hirotaka Terai, Akira Kawakami, and Yoshinori Uzawa, "Characterization of NbN/AlN/NbN Tunnel Junctions", IEEE Trans. on Applied Superconductivity, Vol. 9 (2), 1999.

[44] M. Gurvitch, M. A. Washington, and H. A. Huggins, "High quality refractory Josephson tunnel junctions utilizing thin aluminum layers", Appl. Phys. Lett., Vol 42, pp. 472-474, 1983.

[45] J. H. Smet, C. F. Fonstad, and Q. Hu, "Intrawell and interwell intersubband transitions in multiple quantum wells for far-infrared sources", J. Appl. Phys., vol. 79 (12), pp. 93059320, 1996.

[46] B. Xu, Q. Hu, and M. R. Melloch, "Electrically pumped tunable terahertz emitter based on intersubband transition", Appl. Phys. Lett., vol. 71 (4), pp. 440442, 1997.

[47] "Imaging the dynamics and chemistry of star formation", Flyer from 'Max Planck Institut fuer Radioastronomie', Bonn, 2005.

[48] Paul Grimes, "Design and Analysis of 700 GHz Finline Mixers", PhD thesis, University of Cambridge, 2006.

[49] R Cristiano, M P Lissitskii and C Nappi, "The role of the geometry in superconducting tunnel junction detectors", Supercond. Sci. Technol., Vol. 13, 2000.

[50] R.L. Peterson, "Sidelobe suppression in small losephson junctions", Cryogenics, Vol. 31, 1991.

[51] T. Vaupel, V. Hansen, and F. Schafer, "Radiation efficiency analysis of submillimeter-wave receivers based on a modified spectral domain integration technique", Radio Sci., vol. 38 (4), 2003.

[52] A. Risnen, W. McGrath, P. Richards, and F. L. Lloyd, "Broadband RF match to a millimeter-wave SIS quasiparticle mixer", IEEE Trans. Microwave Theory Tech., vol. 33, pp. 14951500, 1985.

[53] A. Kerr, S. Pan, and M. Feldman, "Integrated tuning elements for SIS mixers", Int. J. IR MM Waves, vol. 9 (2), pp. 203212, 1988.

[54] T. Bttgenbach, H. LeDuc, P. Maker, and T. Phillips, "A fixed tuned broadband matching structure for submillimeter SIS receivers", IEEE Trans. Appl. Superconduct., vol. 2, pp. 165175, Sept. 1992.

[55] J. Zmuidzinas, H. G. LeDuc, J. A. Stern, and S. R. Cypher, "Two junction tuning circuits for submillimeter SIS mixers", IEEE Trans. Microwave Theory Tech., vol. 42, pp. 698706, Apr. 1994.

[56] A. R. Kerr, "Some fundamental and practical limits on broadband matching to capacitive devices, and the implications for SIS mixer design", IEEE Trans. Microwave Theory Tech., vol. 43, pp. 213, 1995.

[57] J. Kawamura, D. Miller, J. Chen, J. Zmuidzinas, B. Bumble, H. G. LeDuc, and J. A. Stern, "Very high current density Nb/AlN/Nb tunnel junctions for low-noise submillimeter mixers", Appl. Phys. Lett., vol. 76 (15), pp. 21192121, 2000.

[58] J. Zmuidzinas, H. G. LeDuc, J. A. Stern, and S. R. Cypher, "Two junction tuning circuits for submillimeter SIS mixers", IEEE Trans. Microwave Theory Tech., vol. 42, pp. 698706, Apr. 1994; and A.M. Baryshev, B.D. Jackson, G. de Lange, S.V. Shitov, N. Iosad, J.R. Gao, and T.M. Klapwijk, "Quasi-optical terahertz SIS mixers", in J. East (Ed.), Proc. 11th Int. Symp. on Space THz Technology, U. of Michigan, Ann Arbor, Michigan, May 1-3, 2000.

[59] M. M. T. M. Dierichs, FL A. Panhuyzen, C. E. Honingh, M. J. de Boer, T. M. Klapwijk, "Submicron niobium junctions for submillimeter-wave mixers using optical lithography", Appl. Phys. Lett., Vol 72 (7), 1993.

[60] Qing Hu, C.A. Mears, P.L. Richards, "Quantum susceptance and its effect on high-frequency response of superconducting tunnel junctions", Phys. rev. B., Vol 42 (16), pp. 10251-10262, 1990.

[61] Jonas Zmuidzinas, Henry G. LeDuc, J.A. Stern, and Scott R. Cypher, "Two-Junction Tuning Circuits for Submillimeter SIS Mixers", IEEE Trans. Microwave Theory Tech., Vol 42 (4), pp. 698-705, 1994.

[62] H.W. Bode, *Network Analysis and Feedback Amplifier Design*, van Nostrand, N.Y., 1945.

[63] R.M. Fano, "Theoretical limitations on the broad-band matching of arbitrary impedances", Journal of the Franklin Institute, Vol 249, pp. 57-83, 1950, and pp. 139-154, 1950.

[64] A. R. Kerr, "Some Fundamental and Practical Limits on Broadband Matching to Capacitive Devices, and the Implications for SIS Mixer Design", IEEE Trans. Microwave Theory Tech., Vol. 43 (1), 1995.

[65] David M. Pozar, *Microwave Engineering*, third edition, John Wiley & Sons, 2004.

[66] Terry Edwards, *Foundations for Microstrip Circuit Design*, second edition, John Wiley & Sons, 1991.

[67] G. Yassin and S. Withington, "Electromagnetic models for superconducting millimetre-wave and su b-m il Iimetre-wave microstrip transmission lines", J. Phys D: Appl. Phys., Vol. 28, pp. 1983-1991, 1995.

[68] Masanori Kobayashi, “A Dispersion Formula Satisfying Recent Requirements in Microstrip CAD”, IEEE Trans. Microwave Theory Tech., Vol. 36 (8), pp. 1246-1250, 1988.

[69] Kautz, R. L., “Miniaturization of normal-state and superconducting striplines”, Journal of Research, National Bureau of Standards, vol. 84, pp. 247-259, May-June 1979.

[70] R.E. Matick, *Transmission Lines for Digital and Communication Networks*, New York, McGraw Hill, 1969.

[71] A.R. Kerr, “Surface Impedance of Superconductors and Normal Conductors in EM Simulators”, MMA Memo No. 245, 1999.

[72] D. C. Mattis and J. Bardeen, “Theory of the Anomalous Skin Effect in Normal and Superconducting Metals”, Phys. Rev., Vol. 111, pp. 412417, 1958.

[73] R. Pöpel, “Electromagnetic Properties of Superconductors”, Superconducting Quantum Electronics, Springer-Verlag, pp. 44-78 in V. Kose, 1989.

[74] N.W. Ashcroft, N.D. Mermin, *Solid State Physics*, Saunders College Publishing, 1976.

[75] E. Gaál, “Current distribution on a strip line”, Acta Tech. (Budapest), Vol. 38, pp. 387-397, 1962.

[76] C.C. Koch, J.O. Scarbrough, and D.M. Kroeger, “Effects of interstitial oxygen on the superconductivity of Nb”, Phys. Rev. B., Vol. 9 (3), pp. 888-897, 1974.

[77] Dr. Ir. F.D. Tichelaar at the National Centre for HREM at Delft University of Technology is acknowledged for the investigations performed by scanning electron microscopy and crytallography.

[78] J. Zmuidzinas and P.L. Richards, “Superconducting Detectors and Mixers for Millimeter and Submillimeter Astrophysics”, Proc. IEEE, VOL. 92 (10), 2004.

[79] L.B. Whitbourn, J.C. Macfarlane, P.A. Stimson, B.W. James and I.S. Falconer, “Infrared Physics” Vol. 28, pp.720, 1988.

[80] J.W. Lamb, “Miscellaneous data on materials for millimeter and submillimeter optics”, International Journal of Infrared and Millimeter Waves, Vol. 17 (12), 1996.

[81] The program was provided by: Dr. Juan R. Pardo-Carrion Departamento de Astrofisica Molecular E Infraroja, Consejo Superior de Investigaciones Cientificas, Madrid, Spain.

[82] Gaidis, M.C.; LeDuc, H.G.; Mei Bin; Miller, D.; Stern, J.A.; Zmuidzinas, J., “Characterization of low-noise quasi-optical SIS mixers for the submillimeter band”, IEEE Trans. Microwave Theory Tech., Vol. 44 (7), pp. 1130-1139, 1996.

[83] Lagarias, J.C., J. A. Reeds, M. H. Wright, and P. E. Wright, “Convergence Properties of the Nelder-Mead Simplex Method in Low Dimensions”, SIAM Journal of Optimization, Vol. 9 (1), pp. 112-147, 1998.

[84] Jonathan Kawamura, David Miller, Jian Chen, Jonas Zmuidzinas, Bruce Bumble, Henry G. LeDuc, and Jeff A. Stern, “Very high-current-density Nb/AlN/Nb tunnel junctions for low-noise submillimeter mixers”, Appl. Phys. Lett., Vol 76 (15), 2000.